DIFFRACTIVE W AND Z BOSON PRODUCTION IN $p\overline{p}$ COLLISIONS AT $\sqrt{s} = 1800$ GeV

A Dissertation

Submitted to the Graduate School

of the University of Notre Dame

in Partial Fulfillment of the Requirements

for the Degree of

Doctor of Philosophy

by

Linda R. Coney , B.S., M.S.

Mitchell Wayne, Director

Department of Physics

Notre Dame, Indiana

April 2000

© Copyright by

LINDA R. CONEY

2000

All rights reserved

DIFFRACTIVE W AND Z BOSON PRODUCTION IN $p\overline{p}$ COLLISIONS AT $\sqrt{s} = 1800$ GeV

Abstract

by

Linda R. Coney

Diffractive W and Z boson production is described for $p\overline{p}$ interactions at a center-of-mass energy of 1800 GeV for events with a forward rapidity gap and concurrent W or Z-boson production. Diffractively produced W and Z bosons are critical for an understanding of diffraction, since their production probes the quark structure of the diffractive exchange. In a sample of $W \to e\nu$ events collected by the DØ experiment at Fermilab, an excess of events with a rapidity gap is observed. This excess is consistent with diffractive W-boson production at the 1% level compared to an inclusive W-boson data sample. A similar excess at the 1% level is reported for a sample of $Z \to e^+e^-$ events, providing the first measurement of diffractive Z-boson production. The (diffractive W/inclusive W) fraction is measured to be $R_W = 1.08 \ \pm^{0.21}_{0.19}$ % for central electrons ($|\eta| < 1.1$) and $R_W = 0.64 \ \pm^{0.19}_{0.16}$ % for forward electrons ($1.5 < |\eta| < 2.5$). A distinct dependence on η of the W gap fraction is observed. The (diffractive Z/inclusive Z) fraction is measured to be $R_Z = 1.38 \ \pm^{0.62}_{0.48}$ %. Furthermore, diffractive W and Z production is modeled using pomeron exchange with a hard quark, hard gluon, and soft gluon pomeron structure. The pomeron model predictions are then compared to the data with attention to both normalization and behaviour as a function of η.

To my parents, Thom A. Coney and Barbara B. Coney, for their constant support and confidence in my abilities.

Whatever trouble life holds for you, that part of your lives which you spend finding out about things, things that you can tell others about, and that you can learn from them, that part will be essentially a gay, a sunny, a happy life, not untouched by rivalry, maybe not even untouched by an occasional regret that somebody else thought of something that you should have thought of first, but on the whole, one of those nobler parts of the human experience. This makes it true that the life of the scientist is, along with the life of the poet, soldier, prophet, and artist, deeply relevant to man's understanding of his situation and his view of his destiny.

J. Robert Oppenheimer

Uncommon Sense

Boston, Birkhauser, 1984.

For God hath not given us the spirit of fear; but of power, and of love, and of a sound mind.

- 2 Timothy 1:7

CONTENTS

TABLES vi

FIGURES x

ACKNOWLEDGEMENTS xxi

CHAPTER 1: INTRODUCTION 1
1.1 History 2
1.2 Thesis Overview 9

CHAPTER 2: THEORY 10
2.1 Standard Model 10
2.2 W and Z Boson Production 16
2.3 W and Z Boson Decay 17
2.4 Soft Diffraction 18
2.5 Hard Diffraction 22
2.6 Soft Color Model 30

CHAPTER 3: THE DØ DETECTOR 31
3.1 Coordinate System 33
3.2 Central Tracking System 36
3.3 Calorimeter 41
3.4 Muon System 50
3.5 Triggering and Data Acquisition 51
3.5.1 Level 0 51
3.5.2 Level 1 and Level 1.5 52
3.5.3 Level 2 54

CHAPTER 4: DIFFRACTIVE W and Z BOSON ANALYSIS 55
4.1 Data Selection 56
4.1.1 Trigger Discussion 56
4.1.2 Offline Cuts 57
4.1.3 Multiple Interaction Cuts 59
4.1.4 Electron Quality Cuts 62
4.2 Signal Measurement 65

4.2.1 Calorimeter Threshold Selection 66
4.2.2 Diffractive Event Identification 68
4.2.3 Corrections and Uncertainties 69
4.3 Fitting 81
4.3.1 Quantitative Signal Extraction Procedure 81
4.3.2 Range Fit Method 83
4.3.3 Event Characteristics 102

CHAPTER 5: MONTE CARLO 112
5.1 Method 113
5.2 Gap Efficiency 117
5.3 Monte Carlo Gap Fraction 129
5.4 ξ Distribution 135

CHAPTER 6: CONCLUSION 141

APPENDIX A: MULTIPLICITY FITS 148
A.1 Dependence of Signal on $n_{L\emptyset}$ and n_{CAL} Ranges 151

BIBLIOGRAPHY 158

TABLES

1.1 The building blocks of matter: 3 generations of leptons and quarks. Each particle also has an associated anti-particle. For example, the positron (e^+) and anti-neutrino ($\overline{\nu_e}$) are the anti-particles of the electron (e) and the electron neutrino (ν_e), respectively. 4

1.2 The four fundamental forces in nature and their associated mediating particles. While the photon and both weak force bosons have been detected, the graviton remains a purely theoretical construct and has not yet been seen. 5

3.1 Conversion from η_d to IETA. 49

4.1 Central and Forward W electron event selection criteria. The event selection process removes events from the event sample based on all of the quality characteristics for each electron rather than making cuts on each quality individually. The bold face numbers indicate how the sample size decreases with each cut. The non-bold numbers simply show how many events have electrons with the corresponding electron characteristic. 60

4.2 Central and Forward Z electron event selection criteria. All selection cuts were applied to each electron for events with CC-CC, CC-EC, and EC-EC electrons. The event selection process removes events from the event sample based on all of the quality characteristics for each electron rather than making cuts on each quality individually. The bold face numbers indicate how the sample size decreases with each cut. The non-bold numbers simply show how many events have electrons with the corresponding electron characteristic. Events containing EC-EC events were removed from the sample as a final cut. 61

4.3 Residual contamination correction for several electron samples. The error was found by varying luminosity by 5.3% and recalculating the residual contamination. 77

4.4 Residual contamination correction for several combined central and forward electron samples. The error was found by varying luminosity by 5.3% and recalculating the residual contamination. 78

4.5 Measured gap fractions for the far gap region for central electron Ws at 1800 GeV center-of-mass energy. The gap fractions were obtained using the range fit method where BOTH SIGNAL and BACKGROUND shapes were taken from the SAME SAMPLE. The raw gap fraction obtained directly from the fit is given for each sample. This raw fraction is then corrected for residual multiple interaction event contamination for each sample using the contamination values listed in Table 4.3. 91

4.6 Measured gap fractions for the far gap region for forward electron Ws at 1800 GeV center-of-mass energy. The gap fractions were obtained using the range fit method where BOTH SIGNAL and BACKGROUND shapes were taken from the SAME SAMPLE. The raw gap fraction obtained directly from the fit is given for each sample. This raw fraction is then corrected for residual multiple interaction event contamination for each sample using the contamination values listed in Table 4.3. 92

4.7 Measured gap fractions for the far gap region for the combined central and forward electron W's at 1800 GeV center-of-mass energy. The gap fractions were obtained using the range fit method where BOTH SIGNAL and BACKGROUND shapes were taken from the SAME SAMPLE. The raw gap fraction obtained directly from the fit is given for each sample. This raw fraction is then corrected for residual multiple interaction event contamination for each sample using the contamination values listed in Table 4.4. 93

4.8 Measured far gap fractions for several electron η bins at 1800 GeV center-of-mass energy. The gap fractions were obtained using the range fit method where BOTH SIGNAL AND BACKGROUND shapes were taken from the SAME SAMPLE. 94

4.9 Number of events with at least one jet from the central + fwd electron W sample for several jet E_T thresholds. 94

4.10 Measured gap fractions for the far gap region for all W+jet events at 1800 GeV center-of-mass energy. Signal extracted using SAME SAMPLE to find SIGNAL and BACKGROUND. NO CORRECTION for residual contamination was performed. 95

4.11 Mean of the minimum side calorimeter multiplicity for several electron W samples. 97

4.12 Mean of the minimum side calorimeter multiplicity for several forward electron W samples. 98

4.13 Mean of the minimum side calorimeter multiplicity for several Z samples. 98

4.14 Measured gap fractions for the far gap region for central electron W's at 1800 GeV center-of-mass energy using HIGH STATISTICS SAMPLES to determine the BACKGROUND SHAPE. 107

4.15 Measured gap fractions for the far gap region for forward electron W's at 1800 GeV center-of-mass energy using HIGH STATISTICS SAMPLES to determine the BACKGROUND SHAPE. 107

4.16 Measured gap fractions for the far gap region for all Z's at 1800 GeV center-of-mass energy. The COMBINED CENTRAL and FORWARD electron W sample was used to find the BACKGROUND SHAPE for the Z sample fit. 108

4.17 Measured gap fractions for the far gap region for all central + forward electron $W + jet$ events at 1800 GeV center-of-mass energy. The COMBINED CENTRAL and FORWARD electron W sample was used to find the BACKGROUND SHAPE for the $W + jet$ samples. 109

5.1 Gap efficiencies for several structure function models of diffractive W and Z boson production using events generated with the POMPYT Monte Carlo package. The maximum possible ξ value was limited to: $\xi_{max} = 0.1$ at generation. 120

5.2 The number of events in each Monte Carlo sample are shown for quark pomeron events, hard gluon pomeron events, and soft gluon events. 124

5.3 Gap efficiencies for several structure function models of diffractive W and Z boson production using events generated with the POMPYT Monte Carlo package. The maximum possible ξ value was limited to: $\xi_{max} = 0.2$ at generation. 127

5.4 Gap efficiencies for diffractive W and Z boson production through pion exchange. Both π^0 and π^+ exchange are modeled using POMPYT. 129

5.5 Predicted fractions, (POMPYT/PYTHIA), of diffractively produced W and Z events are shown after full detector simulation for quark, hard gluon, and soft gluon pomeron models. The maximum possible ξ value was limited to: $\xi_{max} = 0.1$ at generation. The gap efficiency has NOT been taken into account. 131

5.6 Predicted fractions, (POMPYT/PYTHIA), of diffractively produced W and Z are shown after full detector simulation for π^0 and π^+ exchange. The gap efficiency has NOT been taken into account. . . . 131

5.7 Predicted fractions, (POMPYT/PYTHIA), of diffractively produced W and Z events are shown after full detector simulation for quark, hard gluon, and soft gluon pomeron models. The maximum possible ξ value was limited to: $\xi_{max} = 0.2$ at generation. The gap efficiency has NOT been taken into account. 132

5.8 The fraction of diffractive to all W bosons produced in data is shown for both central electron Ws and forward electron Ws. The analogous fraction is also reported for diffractively produced Z bosons. 132

5.9 Final predicted gap fractions, (POMPYT/PYTHIA), of diffractively produced W and Z events are shown after full detector simulation for quark, hard gluon, and soft gluon pomeron models. The maximum possible ξ value was limited to: $\xi_{max} = 0.1$ at generation. The gap efficiency HAS been taken into account. 133

6.1 Measured gap fractions for Ws and Zs at 1800 GeV center-of-mass energy. 142

6.2 Rapidity (η) dependence of the measured gap fractions for W's at 1800 GeV center-of-mass energy. 142

6.3 A comparison of diffractive W and Z data gap fractions to those predicted by POMPYT for a hard quark and hard gluon pomeron. . 144

6.4 A comparison of diffractive W and Z data gap fractions to diffractive dijet data gap fractions. 145

6.5 The diffractive W, Z, and dijet gap fractions [48] measured in data are listed with the associated gap efficiencies for a quark pomeron and hard gluon pomeron. 146

6.6 The diffractive W, Z, and dijet data gap fractions are corrected back to the diffractive fraction using the gap efficiency for a quark pomeron and a hard gluon pomeron. 147

FIGURES

1.1 The soft processes of elastic and diffractive scattering. In elastic scattering, both the proton and antiproton survive leaving a large part of the detector with no particles. This region is referred to as a rapidity gap. For single diffraction, either the proton or antiproton is excited producing particles on one side of the detector and a rapidity gap on the other. 6

1.2 The processes of hard single diffraction (producing jets in the final state) and hard double pomeron exchange. In hard double pomeron exchange, both the incoming proton and antiproton "emit" a pomeron which then participate in the hard scatter. This leaves a dijet system in the central part of the detector with a rapidity gap on both sides. 7

1.3 Hard diffractive production of the W boson leading to an electron and neutrino (identified by an imbalance in event energy) in the final state. 7

2.1 The strong coupling constant, α_s, as a function of the momentum transfer Q. At high momentum transfer, the coupling approaches zero and allows QCD to be calculable using perturbation theory. However, the coupling becomes very strong at low momentum transfer in the non-perturbative region [10]. 13

2.2 Leading order W and Z boson production mechanisms are shown. . 17

2.3 Leading order leptonic W and Z boson decay mechanisms are shown, specifically decays involving the electron and its neutrino ($W \to e\nu$ and $Z \to ee$). These are the most easily detected decay paths for the W and Z bosons at DO; however, there are other decays available for both the W and Z. 18

2.4 Proton-proton elastic cross section vs four-momentum transfer squared at several incident proton momenta. A classical diffraction pattern emerges as the energy increases [12]. 20

2.5 Proton-proton cross sections as a function of laboratory momentum are shown. The total cross section is shown as well as those for only inelastic and elastic processes [12]. 21

2.6 Diffraction occurs through the exchange of a color singlet. As a color singlet, the pomeron has the quantum numbers of the vacuum. It must be a colorless object in order for the proton and/or antiproton to survive the interaction. a)Single diffraction where the $\overline{p}$ breaks apart. b) If the pomeron had color, the outgoing proton would also have color. There would be color strings between the outgoing proton and the pomeron. This would lead to $q\overline{q}$ pair production along the string and the hadronization of the proton. 23

2.7 Factorization allows pomeron exchange to be described as two distinct interactions. a) First, the proton(antiproton) 'emits' the pomeron, b) then a parton from the pomeron participates in a hard scatter with a parton from the antiproton(proton). 26

2.8 Diffractive W production based on a hard quark pomeron structure. 28

2.9 Diffractive W production based on a hard gluon pomeron structure. 28

2.10 Rapidity gap events created through non-perturbative Soft Color Interactions (b,c) through a modification of (a) [25]. 30

3.1 Isometric view of the DØ detector showing the three main systems: the central tracking and vertexing detector, the calorimeter, and the muon system. 32

3.2 Coordinate systems for the DØ detector. The coordinates chosen to describe events are z(beamline direction), η (pseudorapidity), and ϕ (azimuthal angle). 34

3.3 The four systems that make up the central tracking detector. 37

3.4 dE/dx for one and two tracks seen in the full CDC chamber [26]. . . 39

3.5 R-ϕ view of one quadrant of the VTX chambers. 39

3.6 Cross section of the TRD. 40

3.7 Distribution of total energy observed on the three TRD layers for both electron and pion traversals [26]. 41

3.8 R-ϕ view of one quadrant of the CDC chambers. 42

3.9 Expanded view of one set of FDC modules showing chamber orientation. 42

3.10 An isometric view of the DØ calorimeter which is separated into the central cryostat (CC) and two end cryostats (EC). The central tracking system is shown in the center of the calorimeter, surrounded by the EM and hadronic calorimeter. 44

3.11 Side view of one quarter of the DØ calorimeter showing the tower structure in terms of pseudorapidity. 47

3.12 A typical calorimeter cell is shown with uranium absorber and liquid argon for the ionizing medium. 47

3.13 Calorimeter segmentation is shown for detector eta (η_d) and IETA. . 49

3.14 The LevelØ detector is made up of scintillating tiles (shaded squares). The two detectors are mounted around the beam pipe on the front of each end calorimeter cryostat. The LevelØ system is most often used to identify inelastic $p\overline{p}$ collisions, but for diffractive analyses it provides a mechanism to identify rapidity gaps. Here, a hard single diffractive candidate event is shown with activity only on one side of the detector and a gap on the other side. 53

4.1 H-matrix χ^2 distribution for test beam pions (shaded), test beam electrons (unshaded), and electrons from an early $W \rightarrow e\nu$ sample (data points) [45]. Only true electrons have low χ^2 values, which enables us to efficiently remove the pion background events. 64

4.2 The particle multiplicity distributions expected for a) color singlet exchange, and b) color exchange. 66

4.3 Event displays are shown for a typical QCD event and a diffractive W boson candidate event. If the calorimeter is sliced and then unrolled, we get pictures of the detector like those shown here. Each event display shows the amount of energy deposited in the calorimeter, and where these energy deposits were located in ϕ and η. In the QCD event, two jets (localized bunches of energy) can be seen with particles scattered throughout the detector. The diffractive W candidate event has an electron and $\not{E}_T$, with a beam remnant on one side of the detector, but nothing on the other side. This empty region at high η is the rapidity gap which identifies this as a diffractive W event. . . 67

4.4 POMPYT [49] Monte Carlo electron η distribution (mean e η = -0.4335), for $n_{L\emptyset}$ = n_{CAL} =0 on the south side ($\eta > 0$) of the detector. The electron is more frequently found opposite the rapidity gap which is at positive η for this figure, but it is possible for the gap and electron to be on the same side of the detector. 70

4.5 The multiplicity of LØ and calorimeter towers above threshold in the minimum multiplicity far gap region for the central electron W sample is shown. The right-hand plot is a close-up of the region near (0,0). The LØ axis runs from 0 to 20 for the plot on the left, and it runs from 0 to 10 on the close-up plot. The calorimeter tower axis runs from a multiplicity of 0 to 500 and 0 to 20 for the entire plot and the close-up, respectively. 70

4.6 The multiplicity of LØ and calorimeter towers above threshold in the minimum multiplicity far gap region for the forward electron W sample. The right-hand plot is a close-up of the region near (0,0). The LØ axis runs from 0 to 20 for the plot on the left, and it runs from 0 to 10 on the close-up plot. The calorimeter tower axis runs from a multiplicity of 0 to 500 and 0 to 20 for the entire plot and the close-up, respectively. 71

4.7 The multiplicity of LØ and calorimeter towers above threshold in the minimum multiplicity far gap region for the Z sample. The right-hand plot is a close-up of the region near (0,0). The LØ axis runs from 0 to 20 for the plot on the left, and it runs from 0 to 10 on the close-up plot. The calorimeter tower axis runs from a multiplicity of 0 to 500 and 0 to 20 for the entire plot and the close-up, respectively. 71

4.8 Residual contamination calculation for the central electron W sample. The top plot shows the NoCut sample luminosity distribution as a solid line with the standard data sample shown by the dashed line (nearly obscured by the solid points). (The y-axis is the number of events in each luminosity bin, where luminosity is given by the x-axis.) The solid circles represent the predicted number of single interactions for each luminosity bin. The bottom plot again shows the standard sample distribution (solid line) overlaid with the predicted number of single interactions (solid circles) as a function of luminosity. 73

4.9 Residual contamination calculation for the forward electron W sample. The top plot shows the NoCut sample luminosity distribution as a solid line with the standard data sample shown by the dashed line (nearly obscured by the solid points). (The y-axis is the number of events in each luminosity bin, where luminosity is given by the x-axis.) The solid points represent the predictednumber of single interactions for each luminosity bin. The bottom plot again shows the standard sample distribution (solid line) overlaid with the calculated number of single interactions (solid circles) as a function of luminosity. 74

4.10 Residual contamination calculation for the Z sample. The top plot shows the NoCut sample luminosity distribution as a solid line with the standard data sample shown by the dashed line (nearly obscured by the solid points). (The y-axis is the number of events in each luminosity bin, where luminosity is given by the x-axis.) The solid points represent the predictednumber of single interactions for each luminosity bin. The bottom plot again shows the standard sample distribution (solid line) overlaid with the calculated number of single interactions (solid circles) as a function of luminosity. 75

4.11 Central electron W events: Negative energy (x-axis) for signal dominated events compared to that for color exchange dominated events. The top plot shows the amount of negative energy in the EM calorimeter when the far gap on the minimum multiplicity side of the detector had a multiplicity of 0-2. The bottom plot shows the amount of negative energy in the EM calorimeter when the far gap has a multiplicity of 3-5. An event can only be in one or the other of these distributions, but not both. Therefore, these are mutually exclusive bins. 79

4.12 Forward electron W sample: Negative energy (x-axis) for signal dominated events compared to that for color exchange dominated events. The top plot shows the amount of negative energy in the EM calorimeter when the far gap on the minimum multiplicity side of the detector had a multiplicity of 0-2. The bottom plot shows the amount of negative energy in the EM calorimeter when the far gap has a multiplicity of 3-5. An event can only be in one or the other of these distributions, but not both. Therefore, these are mutually exclusive bins. 80

4.13 The multiplicity of LØ and calorimeter towers above threshold in the minimum multiplicity far gap region for the central electron W sample is shown (top left). The top-right plot is a close-up of the region near (0,0). The bottom left plot shows the LevelØ multiplicity distribution and the bottom right shows the calorimeter multiplicity distribution. 84

4.14 Two dimensional multiplicities (LØ vs calorimeter towers) from fitting routine are shown for a single fit for the central electron sample. The top left plot is the 2D $n_{L\emptyset}$ vs. n_{CAL} data distribution. The top right plot shows the 2D $n_{L\emptyset}$ vs. n_{CAL} distribution found using the fit where the signal fit result is added to the background background from the fit. The middle left plot shows the 2D background multiplicity distribution from the fit, and the middle right plot shows the signal multiplicity distribution from the fit. (Note: these two middle plots combine to produce the top right distribution.) The bottom left shows the data - fit distribution, and the bottom right shows the residuals for this single fit. No additional samples were used as background for this case. 85

4.15 Two dimensional multiplicities (LØ vs calorimeter towers) from fitting routine are shown for a single fit for the central electron sample. The top left plot is the 2D $n_{L\emptyset}$ vs. n_{CAL} data distribution. The top right plot shows the 2D $n_{L\emptyset}$ vs. n_{CAL} distribution found using the fit where the signal fit result is added to the background background from the fit. The middle left plot shows the 2D background multiplicity distribution from the fit, and the middle right plot shows the signal multiplicity distribution from the fit. (Note: these two middle plots combine to produce the top right distribution.) The bottom left shows the data - fit distribution, and the bottom right shows the residuals for this single fit. No additional samples were used as background for this case. 86

4.16 The fit results for the 1800 GeV central electron W data sample. Shown is the variation of the signal for fits using an upper limit range of 5-7 in LØ bins and 6-12 in n_{CAL} bins (top). Trial number 1 corresponds to a fit using (LØ ,n_{cal}) upper limits of (5,6). Trial number 2 corresponds to a fit with upper limits of (5,7) and so on until trial number 8 with limits (6,6). Trial number 15 begins the series of fits with LØ upper limit = 7, ending with limits (7,12) for trial 21. The bands represent the parabolic errors from MINUIT and the error bars show the MINOS errors. 88

4.17 The fit results for the 1800 GeV forward electron W data sample. Shown is the variation of the signal for fits using an upper limit range of 5-6 in LØ bins and 6-15 in n_{CAL} bins (top). The upper limits in LevelØ and n_{cal} are stepped through as in the central electron range fit. The bands represent the parabolic errors from MINUIT and the error bars show the MINOS errors. 89

4.18 The 2-D multiplicity of LØ tiles and calorimeter towers above threshold in the minimum multiplicity far gap region for the combined central and forward electron W samples. 96

4.19 One dimensional calorimeter multiplicity distributions (the number of calorimeter towers hit on the x-axis and the number of events on the y-axis). The solid line is the Central W electron sample, and the dashed line is the combined Central + Forward W samples, which is scaled to the central sample. 99

4.20 One dimensional calorimeter multiplicities distributions (the number of calorimeter towers hit on the x-axis and the number of events on the y-axis). The solid line is the standard Central W electron sample, and the dashed line is the Central loose electron quality cut sample, which is scaled to the standard central sample. 100

4.21 One dimensional calorimeter multiplicities (the number of calorimeter towers hit on the x-axis and the number of events on the y-axis). The solid line is the standard Central W electron sample, and the dashed line is the Central electron sample where only an miflag multiple interaction cut was imposed. Note that the normalization between the two distributions is correct. The miflag sample multiplicity distribution is pushed out to much higher n_{cal} than the standard sample. This is an indication that the miflag sample background shape does not match that of the standard sample; therefore, it is not used for the Alternate Background Sample Fitting Method. 100

4.22 One dimensional calorimeter multiplicities: the solid line is the standard Forward W electron sample, and the dashed line is the combined Central + Forward W sample which has been scaled to the forward electron W sample size. 101

4.23 One dimensional calorimeter multiplicities: the solid line is the standard Z sample, and the dashed line is the combined Central+Forward W sample which has been scaled to the Z sample size. 101

4.24 Two dimensional multiplicities (LØ vs calorimeter towers) from a single 2D fit extraction of the quantitative signal for the central electron W sample. The background shape was taken from the combined central+forward electron W samples, scaled to the statistics in the central only W sample, and fixed for the fitting procedure. The top two plots show i) only the data $n_{L\emptyset}$ vs. n_{CAL} multiplicity plot, and ii) the signal and background $n_{L\emptyset}$ vs. n_{CAL} multiplicity distribution from the fit. The middle plots show the individual multiplicities for iii) the background,and iv) the signal from the fit. (Note: these two middle plots combine to produce the top right distribution.) Finally, the bottom plots show v) data - fit, and vi) residuals for this individual fit. 103

4.25 Two dimensional multiplicities (LØ vs calorimeter towers) from a single 2D fit extraction of the quantitative signal for the forward electron W sample. The background shape was taken from the combined central+forward electron W samples, scaled to the statistics in the forward only W sample, and fixed for the fitting procedure. The top two plots show i) only the data $n_{L\emptyset}$ vs. n_{CAL} multiplicity plot, and ii) the signal and background $n_{L\emptyset}$ vs. n_{CAL} multiplicity distribution from the fit. The middle plots show the individual multiplicities for iii) the background,and iv) the signal from the fit. (Note: these two middle plots combine to produce the top right distribution.) Finally, the bottom plots show v) data - fit, and vi) residuals for this individual fit. 104

4.26 Two dimensional multiplicities (LØvs calorimeter towers) from a single 2D fit extraction of the quantitative signal for the Z sample. The background shape was taken from the combined central+forward electron W samples, scaled to the statistics in the Z sample, and fixed for the fitting procedure. The top two plots show i) only the data $n_{L\emptyset}$ vs. n_{CAL} multiplicity plot, and ii) the signal and background $n_{L\emptyset}$ vs. n_{CAL} multiplicity distribution from the fit. The middle plots show the individual multiplicities for iii) the background,and iv) the signal from the fit. (Note: these two middle plots combine to produce the top right distribution.) Finally, the bottom plots show v) data - fit, and vi) residuals for this individual fit. 105

4.27 The fit results for the 1800 GeV central electron W data sample are presented. Shown is the variation of the signal for fits using an upper limit range of 5-7 in LØ bins and 6-12 in n_{CAL} bins (top). The bands represent the parabolic errors from MINUIT and the error bars show the MINOS errors. The combined central and forward electron W sample was used to find the background shape for this fit. 106

4.28 The fit results for the 1800 GeV forward electron W data sample are presented. Shown is the variation of the signal for fits using an upper limit range of 5-7 in LØ bins and 6-12 in n_{CAL} bins (top). The bands represent the parabolic errors from MINUIT and the error bars show the MINOS errors. The combined central and forward electron W sample was used to find the background shape for this fit. 106

4.29 The fit results for the 1800 GeV Z data sample are presented. Shown is the variation of the signal for fits using an upper limit $n_{L\emptyset}$ and n_{CAL} range of (5-6:6-12). The bands represent the parabolic errors from MINUIT and the error bars show the MINOS errors. The combined central and forward electron W sample was used to find the background shape for this fit. 108

4.30 Event characteristics for standard central electron W boson events (left column, $n_{CAL} > 1$) compared to diffractive W boson candidate events (right column, $n_{L0} = n_{CAL}$ =0). The top plots compare electron E_T (on the x-axis), the middle show $\not\!\!E_T$ (on the x-axis) in the events, and the bottom plots compare the transverse mass (x-axis) for the two cases. Note: Events either fall into the standard W event sample or the diffractive candidate event sample; therefore, for each set of comparisons mutually exclusive data sets are examined. 110

4.31 Event characteristics for standard forward electron W boson events (left column, $n_{CAL} > 1$) compared to diffractive W boson candidate events (right column, $n_{L0} = n_{CAL}$ =0). The top plots compare electron E_T (on the x-axis), the middle show $\not\!\!E_T$ (on the x-axis) in the forward electron events, and the bottom plots compare the transverse mass (x-axis) for the two cases. Note: Events either fall into the standard W event sample or the diffractive candidate event sample; therefore, for each set of comparisons mutually exclusive data sets are examined. 111

5.1 Comparison of PYTHIA (solid line) W event characteristics to high multiplicity non-diffractive W data (dashed line). The PYTHIA events have been run through a full simulation of the DØ detector using GEANT. The top left plot shows a comparison of the electron η_d. Note that the distributions both dip around $\eta_d = \pm 1.2$. This is a detector effect. The top right plot shows a comparison of the electron E_T for PYTHIA and the non-diffractive data. The bottom left plot shows a comparison of $\Delta\phi$ for the electron and neutrino. This shows that they are equally back-to-back in data and PYTHIA. Finally, the bottom right plot shows the transverse mass for both PYTHIA and non-diffractive data. 114

5.2 POMPYT (top plot) and PYTHIA (bottom plot) minimum side particle multiplicity distributions using a far gap for forward electron W's. The POMPYT multiplicity is peaked at low multiplicities, while the PYTHIA multiplicity is a broad distribution with a much higher mean. 115

5.3 The electron η distributions for W boson events generated in POMPYT using a quark pomeron structure (solid line), a hard gluon structure (dashed line), and a soft gluon structure (dotted line). The rapidity gap for all events in these samples is located at $+\eta$. Although it is less common, it *is* possible for the electron to be located on the same side as the gap. 116

5.4 The quark pomeron POMPYT (top plot) and PYTHIA (bottom plot) n_{LO} vs n_{CAL} minimum side multiplicity distributions in the far gap region for central electron W's. 118

5.5 The gap efficiency was extracted by simultaneously fitting a non-diffractive background and the diffractive signal. The Monte Carlo Level Ø vs. calorimeter tower multiplicity (top left histogram) and the background multiplicity histogram from a fit to data (top right) were added together (bottom left). This combined sample was then fit several times to find the number of Monte Carlo events detected. Each fit used a slightly different background shape (example at bottom right). 119

5.6 Multiplicity distributions for central electron W events are shown for a quark pomeron structure (top left), hard gluon (top right) structure, and soft gluon (bottom left) structure. The distributions for quark and hard gluon structures look very similar and both have a pronounced peak in the (0,0) bin. For each distribution, the LevelØ multiplicity runs from 0 to 10 and the calorimeter tower multiplicity from 0 to 20. 121

5.7 Multiplicity distributions for forward electron W events are shown for a quark pomeron structure (top left), hard gluon (top right) structure, and soft gluon (bottom left) structure. As in the central electron case, the distributions for quark and hard gluon structures look very similar and both have a pronounced peak in the (0,0) bin. For each distribution, the LevelØ multiplicity runs from 0 to 10 and the calorimeter tower multiplicity from 0 to 20. 122

5.8 Multiplicity distributions for Z events are shown for a quark pomeron structure (top left), hard gluon (top right) structure, and soft gluon (bottom left) structure. Again, the distributions for quark and hard gluon structures look very similar and both have a pronounced peak in the (0,0) bin. For each distribution, the LevelØ multiplicity runs from 0 to 10 and the calorimeter tower multiplicity from 0 to 20. . . 123

5.9 Calorimeter multiplicity (x-axis) distributions are shown for central electron W events: quark structure pomeron (top plot) mean number of calorimeter towers above threshold =8.9, and soft gluon structure (bottom) mean = 16.8 towers. 125

5.10 Multiplicity distributions for central electron W events in bins of ξ (the fraction of the initial proton momentum carried by the pomeron). As ξ increases (top left $\rightarrow$ top right $\rightarrow$ bottom left $\rightarrow$ bottom right), a lower percentage of events are at low multiplicities, and the gap efficiency decreases. For each distribution, the LevelØ multiplicity runs from 0 to 10 and the calorimeter tower multiplicity from 0 to 30. 127

5.11 Multiplicity distributions for forward electron W events in bins of ξ (the fraction of the initial proton momentum carried by the pomeron). As ξ increases (top left $\rightarrow$ top right $\rightarrow$ bottom left $\rightarrow$ bottom right), a lower percentage of events are at low multiplicities, and the gap efficiency decreases. 128

5.12 The ξ distribution is shown for quark pomeron W events with electron $E_T > 25$ GeV (solid line). The dashed line is the ξ distribution for central electron events, and the dotted line represents forward electron events. The central electron events probe a higher ξ region than the forward events. 136

5.13 The ξ distribution is shown for quark pomeron Z events with electron $E_T > 25$ GeV (solid line). The dashed line is the ξ distribution for CC-CC electron events, and the dotted line represents CC-EC electron events. The CC-CC electron events probe a higher ξ region as did the central electron W events. 137

5.14 The ξ distribution for quark pomeron W events is shown for central electron events with no rapidity gap required (solid line) and for events with a far gap (dashed line). Many of the high mass states have been excluded by demanding a rapidity gap. The mean of the distribution drops from ($\xi_{MEAN} = 0.06$) to ($\xi_{MEAN} = 0.04$) when a far gap is required. 138

5.15 The ξ distribution for quark pomeron W events is shown for forward electron events with no rapidity gap required (solid line) and for events with a far gap (dashed line). Again, the higher mass states have been excluded by demanding a rapidity gap. The mean of the distribution drops from ($\xi_{MEAN} = 0.03$) to ($\xi_{MEAN} = 0.02$) when a far gap is required. 139

5.16 The ξ distribution for quark pomeron Z events is shown for CC-CC (top plot) electron events with no rapidity gap required (solid line) and for events with a far gap (dashed line). The distribution is shown for CC-EC events (bottom plot) without (solid) and with a gap (dashed line). Again, many of the higher mass states have been excluded by demanding a rapidity gap. 140

A.1 The multiplicity of LØ and calorimeter towers above threshold in the minimum multiplicity far gap region for the central electron W sample is shown (top left). The top-right plot is a close-up of the region near (0,0). The bottom left plot shows the LevelØ multiplicity distribution and the bottom right shows the calorimeter multiplicity distribution. 149

A.2 Two dimensional multiplicities (LØ vs calorimeter towers) from fitting routine are shown for a single fit for the central electron sample. This fit was done using upper limits in ($n_{L\emptyset}$,n_{CAL}) =(7,11). The top left plot is the 2D $n_{L\emptyset}$ vs. n_{CAL} data distribution. The top right plot shows the 2D $n_{L\emptyset}$ vs. n_{CAL} distribution found using the fit where the signal fit result is added to the background background from the fit. The middle left plot shows the 2D background multiplicity distribution from the fit, and the middle right plot shows the signal multiplicity distribution from the fit. (Note: these two middle plots combine to produce the top right distribution.) The bottom left shows the data - fit distribution, and the bottom right shows the residuals for this single fit. 154

A.3 Top: Variation of hard single diffraction with jets signal where 42 different fits have been done (x-axis) by varying the background region used in the fit. The bottom left plot shows the signal distribution with one entry per fit. This is used to find the mean signal fraction, and the rms error on the distribution. The bottom center and bottom left plots show the distributions of the upper and lower MINOS errors, respectively, for each fit. 155

A.4 Top: Variation of central electron diffractive W signal where 21 different fits have been done (x-axis) by varying the background region used in the fit. The bottom left plot shows the weighted signal distribution with one entry per fit. This is used to find the weighted mean signal fraction, and the rms error on this distribution. The bottom center and bottom left plots show the distributions of the weighted upper and lower MINOS errors, respectively, for each fit. In each case, fits with smaller MINOS errors are given higher weight in the average. 156

A.5 The fit results for the 1800 GeV central electron W data sample are presented. Shown is the variation of the signal for fits using an upper limit range of 5-7 in LØ bins and 6-12 in n_{CAL} bins (top). The bands represent the parabolic errors from MINUIT and the error bars show the MINOS errors. The combined central and forward electron W sample was used to find the background shape for this fit. 157

ACKNOWLEDGEMENTS

The analysis presented in this thesis was made possible only through the efforts of many people that preceded me. I would like to thank all those who put forth the astounding amount of effort needed to design, build, test, and successfully run the DØ detector. I still remember the first time I saw the detector in the assembly building after RunI finished. This phenomenal piece of machinery was positioned where before I had only seen concrete blocks. DØ was already up and running 24-7 when I arrived on the scene, so I had to wait quite a while to get a glimpse. As we approach RunII, I am developing a greater appreciation for the body of work needed to accomplish this . I also acknowledge those who possessed the creativity and drive necessary to build the Tevatron and put Fermilab at the forefront of high energy physics.

My time in graduate school has been spent at two great institutions: the University of Notre Dame and the Fermilab DØ experiment. I have learned a great deal, and I feel fortunate to have had this experience. I want to thank those who made me feel welcome at Notre Dame from my first visit. In particular, I acknowledge my classmates: Don Peterson, Paul Tischhauser, Yi Jiang, Shirlan Johnson, Subrahmanyam Mallampalli, Frank Peiris, and Yee-Kin Tsui. They are a terrific group of people, and I feel fortunate to know them. Their friendship and collaboration made time at Notre Dame truly enjoyable.

I especially want to thank my advisor, Mitch Wayne, for providing me with opportunities and for giving me the freedom to choose my own path. He allowed me

to find an analysis that appealed to me, while still exploring other interests in accelerator physics and politics. I greatly appreciate his support and, most recently, his efforts over the past semester. On the same note, I want to acknowledge the efforts of the members of my dissertation committee: Mitch, Neal Cason, Bill Shephard, and Jonathan Sapirstein.

I also value my experience at DØ, in great part due to the people I have met and/or with whom I have worked. Bob Kehoe was both a wealth of knowledge and a good friend to me when I first came to Fermilab. I would like to thank him for getting me started on the energy scale, for answering all of my questions, and for always providing me with good advice. I would like to thank Harry Weerts for taking an interest in graduate students and giving credit where it is due. I also want to thank the QCD group (and within, the rapidity gap group) for creating an environment of interest and education.

I am particularly grateful to my rapidity gap group colleagues. They laid the groundwork for my analysis, and taught me more than I ever imagined I would learn. I want to thank Andrew Brandt for bringing me into the group, getting me involved in this analysis, and providing a steady stream of good ideas, and insight into diffractive physics. I also want to thank Bob Hirosky for his amazing ability to answer questions and solve particularly nasty fitting problems. Jill Perkins was one of the first people I remember meeting when I came to DØ. I acknowledge her for making me feel welcome, providing housing for me when it was needed, and for planting that rap gap group seed in my mind. I am deeply grateful to Kristal Mauritz for her work in this group, for her unflagging support, for the after-meeting discusions, and for her help dealing with the everyday catastrophes of graduate school.

Of course, I would not have been able to succeed without the love and support of my family. I honor my parents, Barb and Thom Coney, for their constant support,

patience, intelligence, humor, and unconditional love. They have always encouraged me in everything I do. I thank them for nurturing my curiosity, for introducing me to science, for telling me how it is, for teaching me before anyone else could (lettuce costs 79 cents today), for whispering "physics" to me in the crib, and for genetics.

I also deeply appreciate the support of my friends. In particular, I thank Denton Morris for his incredible patience, his humor, and his Renaissance personality. He has listened to me worry, has calmed me down before I became hysterical, has helped me to survive this process, and will help me celebrate its completion. I would like to thank Kristal Mauritz, Drew Green, and Kevin Davis for keeping me sane and human at work, and helping me to get out of the office occasionally for trips to DC or France. I would like to thank Crissy Barnas for keeping me grounded and reminding me of life after school, and for many hours of discussion, sage advice, and several dozen grilled cheese sandwiches. I greatly appreciate my friendship over the years with Fil Rysanek and Jen (my setter), Colin, and now Logan Bown. Finally, I thank Anne Findura and Lena Putkonen Winkler who knew me way back when, for sticking with me this far, and believing in me.

CHAPTER 1

INTRODUCTION

Diffractive W and Z boson production is described for $p\overline{p}$ interactions at a center-of-mass energy of 1800 GeV. This class of events produces a forward rapidity gap and concurrent W and Z production. This unique topology, used to identify these events, is due to the fact that one of the incoming particles (p or $\overline{p}$) survives the interaction intact. W and Z bosons produced in this manner are critical for a more complete understanding of diffraction, since their production probes the quark structure of the exchange.

In samples of $W \to e\nu$ and $Z \to e^+e^-$ events collected by the DØ experiment at the Fermilab Tevatron, an excess of events with a rapidity gap is observed. The (diffractive W/inclusive W) fraction is measured to be $R_W = 1.08\ \pm^{0.21}_{0.19}\,\%$ for central electrons ($|\eta| < 1.1$) and $R_W = 0.64\ \pm^{0.19}_{0.16}\,\%$ for forward electrons ($1.5 < |\eta| < 2.5$). A distinct dependence on η of the W gap fraction is observed. Additionally, the first measurement of diffractively produced Z bosons is reported where $R_Z = 1.38\ \pm^{0.62}_{0.48}\%$. Furthermore, diffractive W and Z production is modeled using pomeron exchange with a hard quark, hard gluon, or soft gluon pomeron structure functions, respectively. The pomeron model predictions are then compared to the data with attention to both normalization and behaviour as a function of η.

Although our goal is a very specific understanding of diffractive W and Z boson events produced in $p\overline{p}$ interactions, we begin at a much more general level. In order to interpret the results of this analysis, we need to determine where this information

belongs in the greater context of particle physics. We must also recognize the phenomenal advances made in our understanding of the natural world which enable us to even consider such an endeavor. As Isaac Newton said, "If I have seen further... it is by standing upon the shoulders of giants."

1.1 History

The quest to understand the intricacies of nature has been underway for centuries. An insatiable curiosity and the desire to fully grasp the workings of the natural world characterize scientists regardless of their chosen field of study. This inherent curiosity has produced incredible advances in a wide range of disciplines: diseases have been erradicated, trips into space for satellite repair have become almost routine, the birth of the universe has been described, human DNA has been partially mapped, and computers have become a household appliance on par with the toaster oven. Within this great diversity one finds physics, the most fundamental physical science upon which astronomy, chemistry, and geology are based.

Describing the behavior of matter has always been a significant goal in physics. This endeavor began, rather sensibly, at the macroscopic level. For example, in 1543 Copernicus proposed the heliocentric notion that perhaps the earth revolved around the sun. Around the same time, Galileo studied the motion of objects in free fall and on inclined planes. These basic studies in mechanics paved the way for Newton's development of the laws of motion which were published in his Mathematical Principles of Natural Philosophy in 1687. In addition to the study of mechanics, the electric and magnetic behavior of matter was also being explored. It was determined that these phenomena are related, and in 1873 Maxwell formulated the laws of electromagnetism.

About a century ago, it was thought that physics had been figured out. Classical (macroscopic) mechanics, Maxwell's electromagnetism, thermodynamics, and

kinetic theory very successfully explained a wide variety of observed phenomena. At this point, matter was thought to consist of atoms, then considered to be the fundamental particle. However, this model would soon become obsolete with the debut of particle physics in 1897 when J.J. Thomson discovered the electron. Then in the original colliding experiment, Rutherford bombarded gold foil with a beam of α-particles to probe the structure of the atom. Dramatic scattering at unexpectedly high angles of some of the α particles pointed to the existence of a massive atomic nucleus. Suddenly, the atom was no longer the basic building block of material. During the same period of time, the seeds of quantum mechanics were planted and Einstein formulated his special theory of relativity. These revolutionary concepts dramatically changed the face of physics and opened doors to new discoveries in atomic, nuclear, and particle physics.

Over the next century, particle physics probed inward from the atomic level to find the fundamental constructs of matter and the forces which govern their interactions. It was eventually learned that the atom is made up of electrons and a nucleus of protons and neutrons. These protons and neutrons in turn are composed of fundamental particles called quarks. However, this was hardly the full picture. Over a relatively short period of time, many experiments discovered hundreds of other particles along with new forces of nature. With this proliferation of information, a new theory was required to classify the abundance of elementary particles and explain the interactions between them.

The Standard Model provided this much needed description of the most elementary level of physics. In this theory, all matter reduces to three types of particles: leptons, quarks, and mediators. (Note: There is an ongoing attempt to see whether quarks are truly fundamental or if they also have an inner structure [1].) Table 1.1 shows the 6 leptons and 6 quarks. The quark type (u,d,c,s,t,b) is also referred to as

the quark "flavor".

Leptons are divided into three families (or generations) based on their properties. Each lepton has an associated anti-particle bringing the total number up to 12. There are also three generations of quarks (q) and anti-quarks ($\overline{q}$), which can come in one of three colors for a total of 36. Finally, every interaction between these particles has a mediator. (Interestingly, all matter is made up of d-quarks, u-quarks, and electrons. The other particles are very short-lived and require complex accelerators to study them.)

Table 1.1. The building blocks of matter: 3 generations of leptons and quarks. Each particle also has an associated anti-particle. For example, the positron (e^+) and anti-neutrino ($\overline{\nu_e}$) are the anti-particles of the electron (e) and the electron neutrino (ν_e), respectively.

Leptons		**Spin**	**Quarks**		**Spin**
e	ν_e	$\frac{1}{2}$	u (up)	d (down)	$\frac{1}{2}$
μ	ν_μ	$\frac{1}{2}$	c (charm)	s (strange)	$\frac{1}{2}$
τ	ν_τ	$\frac{1}{2}$	t (top)	b (bottom)	$\frac{1}{2}$

The four basic forces that underlie all observed phenomena are gravity, electromagnetism, the weak force, and the strong force. Gravity operates at very long distances, but is comparatively weak. Electromagnetism is also a long range force, while the weak and strong forces operate at very short distances. The strong force holds the atomic nucleus together, and weak interactions are essential to the generation of energy in the sun. These four forces govern the interaction of matter through the exchange of the mediating particles shown in Table 1.2. The photon mediates electromagnetic interactions, and the W and Z bosons are the carriers for the weak nuclear force. While gravity is still explained with classical mechan-

Table 1.2. The four fundamental forces in nature and their associated mediating particles. While the photon and both weak force bosons have been detected, the graviton remains a purely theoretical construct and has not yet been seen.

Force	Mediating particle	Mass (GeV/c^2)	Spin
Strong	Gluon (g)	0	1
Electromagnetism	Photon (γ)	0	1
Weak	W and Z Bosons	~ 80 and ~ 90	1
Gravity	graviton (G)	0	2

ics and general relativity only, electromagnetic, weak and strong interactions are now described using quantum field theories. Quantum electrodynamics (QED) and quantum chromodynamics (QCD) are the theories of the electromagnetic and strong forces respectively. Furthermore, weak and electromagnetic interactions have been unified into one force(electroweak). There are ongoing efforts to combine the electroweak and strong forces into one coherent (grand unified) theory, although they have not yet been successful.

As in every scientific endeavor, these theories must be tested experimentally. In the tradition of Rutherford, experiments are done today which collide particles in order to probe the nature of the subatomic world. Very sophisticated tools are needed to study phenomena at such a minute scale, which can be as small as 10^{-18} m. Several accelerators have been developed which collide particles such as electrons or protons at nearly the speed of light. Since protons are made up of quarks and gluons, proton-antiproton ($p\overline{p}$) accelerators can actually produce $q\overline{q}$, qg, and gg collisions. These accelerators act as microscopes providing a glimpse into the world of particle physics. Complex detectors monitor the collisions, collect the

products of the interactions, and record volumes of information about the events. This information is analyzed with respect to proposed theories, and is used to search for new and unexpected phenomena. The Standard Model has been explored using studies of b quark mesons and CP violation and the search for and discovery (in 1995) of the top quark [3]. Precision measurements of the production cross sections for W bosons, Z bosons, and jets (clusters of particles, see [2]) also provide tests of standard model validity. As the tip of the proverbial iceberg, this list of analyses gives one an idea of the great scope of experimentation in particle physics.

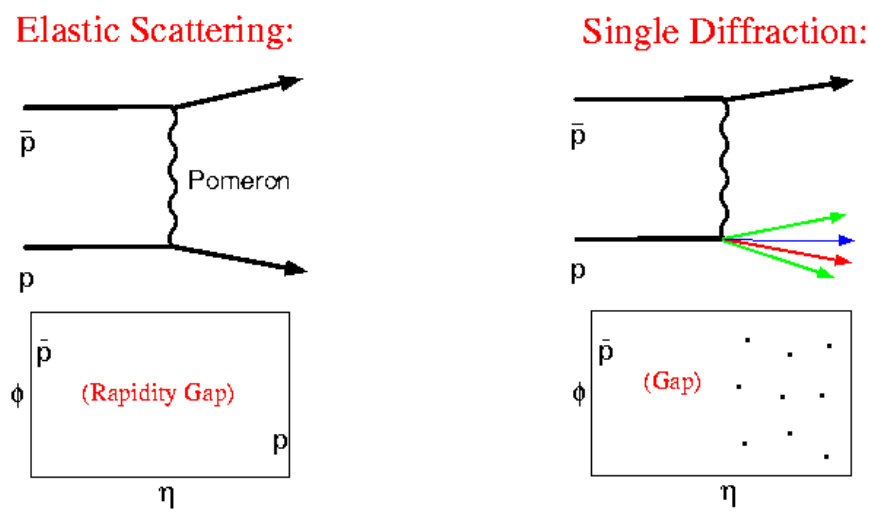

Figure 1.1. The soft processes of elastic and diffractive scattering. In elastic scattering, both the proton and antiproton survive leaving a large part of the detector with no particles. This region is referred to as a rapidity gap. For single diffraction, either the proton or antiproton is excited producing particles on one side of the detector and a rapidity gap on the other.

At the Fermilab Tevatron, the world's most powerful accelerator, protons (p) and antiprotons ($\overline{p}$) are collided at extremely high energies, $\sim$ 2 TeV. Many of the resultant interactions are diffractive processes, including elastic and diffractive

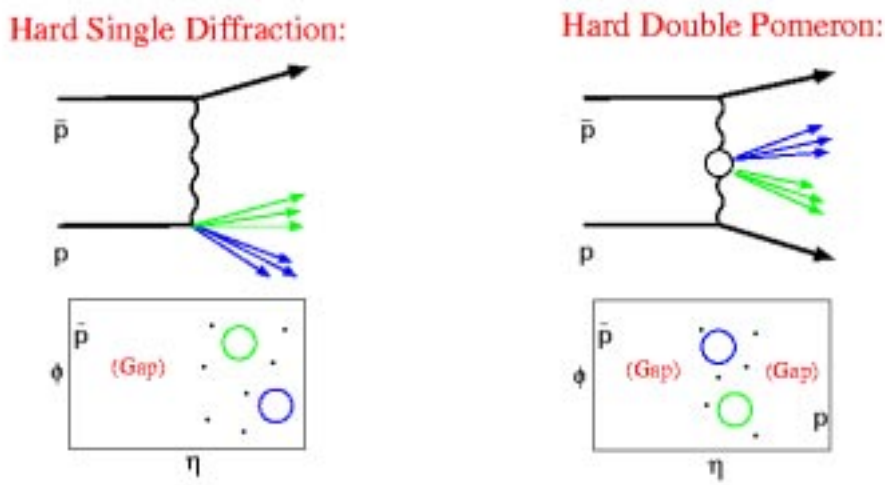

Figure 1.2. The processes of hard single diffraction (producing jets in the final state) and hard double pomeron exchange. In hard double pomeron exchange, both the incoming proton and antiproton "emit" a pomeron which then participate in the hard scatter. This leaves a dijet system in the central part of the detector with a rapidity gap on both sides.

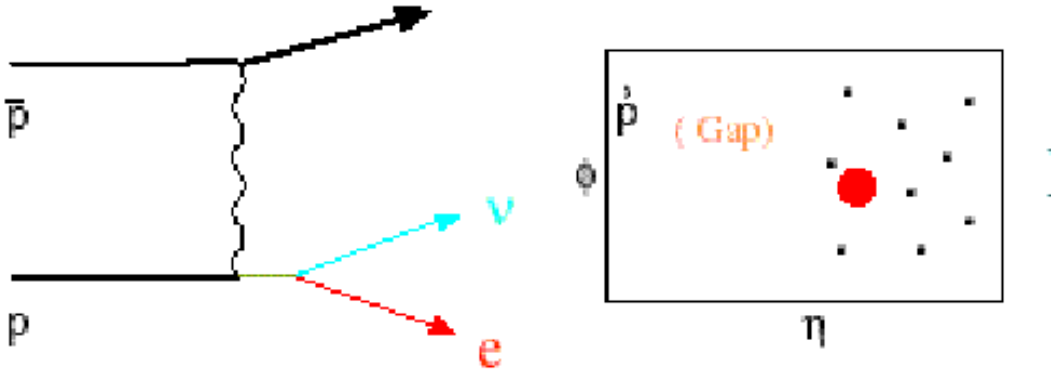

Figure 1.3. Hard diffractive production of the W boson leading to an electron and neutrino (identified by an imbalance in event energy) in the final state.

scattering, where one or both of the incident hadrons survive the encounter intact. For elastic scattering,

$$\mathrm{p} + \overline{p} \rightarrow \mathrm{p} + \overline{p} \ ,$$

some momentum is transferred from one beam particle to the other and both incoming particles survive the encounter. Since the p and $\overline{p}$ continue down the beam pipe, the detector is left devoid of particles. This empty region is referred to as a rapidity gap, where rapidity or pseudorapidity (η) is part of the coordinate system used to define a location within the detector volume. (ϕ and z complete the coordinate system.) For single diffraction,

$$\mathrm{p} + \overline{p} \rightarrow \mathrm{p} + \mathrm{X}$$

either the p or $\overline{p}$ is excited producing particles (X) on one side of the detector, and a rapidity gap on the other (see Fig. 1.1). These soft processes are well described by pomeron exchange (named after Russian physicist Isaak Jakoblevich Pomeranchuk) in Regge theory [4]; however, the nature of this exchanged object is not well understood.

Hard diffractive events are the subset of diffractive dissociation in which a high transverse momentum scattering occurs (see Figs. 1.2 and 1.3). Jets, W and Z bosons, J/Ψ particles, and b quarks can all be produced diffractively. These events provide an arena in which to probe the pomeron structure and test the hypothesis that it is a particle-like object. Interest in this subject began when Ingelman and Schlein [5] suggested that jets from diffractive interactions would give clues to the partonic structure of the pomeron. This is again the classic case of studying an object that is not well understood (the pomeron) by colliding it with something that is understood (the proton). While the gluon component of the pomeron is primarily explored by diffractive jet (j) production,

$$\mathrm{p} + \overline{p} \rightarrow \mathrm{p} + \mathrm{jj}$$

the quark component can be probed by diffractively produced W and Z-bosons

$$\mathrm{p} + \overline{p} \rightarrow \mathrm{p} + W$$

$$\mathrm{p} + \overline{p} \rightarrow \mathrm{p} + Z.$$

1.2 Thesis Overview

This analysis measures the rate of diffractive W and Z boson production in $p\bar{p}$ collisions at the Fermilab Tevatron; furthermore, an attempt is made to probe the quark component of the pomeron and provide insight into the validity of the pomeron-as-particle hypothesis. The results will provide a valuable complement to other hard diffraction studies by measuring the quark component of the pomeron structure.

This thesis describes in detail the many aspects of this analysis. A brief overview of the Standard Model is given in Chapter 2 with particular emphasis placed on quantum chromodynamics and W and Z boson production and decay. Additionally, the underlying theory of diffractive physics is summarized with special attention placed on diffractive W and Z production. Chapter 3 contains a description of the DØ detector, and Chapter 4 explains in detail the analysis of the $W \rightarrow e\nu$ and $Z \rightarrow ee$ data. This explanation includes descriptions of the event selection criteria, the method used to identify diffractive events within the data samples, and the method used to extract the quantitative diffractive W and Z boson production signals. Chapter 5 presents the Monte Carlo predictions for these processes, and a comparison to the data results. Finally, the results and the associated implications are discussed in Chapter 6.

CHAPTER 2

THEORY

2.1 Standard Model

In the Standard Model, electromagnetic phenomena are described using quantum electrodynamics (QED), and strong force interactions are described by quantum chromodynamics (QCD) [6] [7] [8]. Furthermore, the electromagnetic and weak force interactions are joined into one coherent force described by the electroweak theory. Each of these are quantum field theories, specifically, gauge theories. In electromagnetic interactions, charge is conserved and the photon mediates the interaction. Any charged particle, including electrons (e^-), muons (μ^-), and quarks (q), can interact electromagnetically.

As indicated by the name 'chromodynamics', QCD governs interactions between color-carrying quarks. Each quark carries one of three "colors" (or anti-colors) labeled "red", "green", and "blue" (rgb or $\overline{rgb}$). Although these are not the same colors we see, the name is used because of certain parallels in the behavior of QCD interactions and everyday color. In particular, particles such as protons or neutrons are composed of three quarks, each of which carries a different color. However, these protons and neutrons are color neutral (i.e. they have no net color). The color charges of the constituent quarks cancel out, much like white light produced from the combination of the three primary colors. In fact, all naturally occurring particles are colorless, being made of either three quarks or anti-quarks (baryons and anti-baryons), one quark and one anti-quark (mesons like the $\pi^{\pm}$), or no quarks

(leptons like the electron or muon). The color force is mediated by the exchange of gluons which carry one positive and one negative unit of color. In QCD interactions, quark color (although not flavor) may change. A quark can go from red to green, but must remain an up or down quark for example. The force carriers for QED and QCD interact differently. In QED, the photon only interacts with charged particles, and therefore does not interact with other photons. On the other hand, gluons carry color; therefore, they are able to couple directly to other gluons.

There are several significant consequences of the QCD theory, especially with regard to $p\overline{p}$ interactions. First is the evolution of the proton structure function. The proton composition is not as simple as first stated. In addition to the three valence quarks (uud), there are gluons and sea quarks. The latter are $q\overline{q}$ pairs that can fluctuate into existence for a short period of time. During a quantum fluctuation, gluons can also be virtually emitted and absorbed. In a naive parton model, the proton structure functions, F(x), depend only on the momentum fraction of the parton and not on the momentum transfer (Q^2) of the interaction. (Q^2 is also known as the energy scale of an event.) However, in QCD the spatial region or time interval probed decreases as the Q^2 of a given probe increases. Whereas a moderate probe might observe a quark, one at high Q^2 might see a quark and a gluon. In other words, high momentum probes have a smaller probability of finding a quark or gluon carrying a large part of the proton momentum. In this case, it would be much more likely to find a small-x quark or gluon.

Another important consequence of QCD is the running of the coupling constant, α_s. This "constant" (which in fact is not so) provides a measure of the strength of the strong interaction, and depends on the distance between the interacting particles. In QED, vacuum polarization (production of e^+e^- pairs) screens the bare charge of an interacting particle. In other words, the full charge of the particle is not felt

until the probe is at a short distance (high Q^2) where the screening disappears. As a result, the strength of the electromagnetic force increases at short distances (from $\alpha_{em} = 1/137$ to $1/128$) [9]. However, the picture changes when dealing with QCD, which provides mechanisms for both screening and anti-screening of the color charge. In a manner analogous to QED, $q\overline{q}$ pair production screens color charge, but in QCD gluons can also couple to each other. This results in a mechanism which anti-screens the color charge. Due to the fact that there are 3 colors and 6 flavors of quarks, anti-screening dominates and α_s decreases with increasing momentum transfer. At high momentum transfer (as at the Tevatron) the strong coupling strength between particles decreases and even approaches zero (see Figure 2.1). This behavior of α_s is the basis for asymptotic freedom, which (at high Q^2) allows partons to be treated as free particles. As a result, perturbation theory can be used at high momentum to describe strong interactions with QCD. However, in the low momentum transfer regime, the strong coupling strength increases and QCD cannot calculate the interaction.

Another breakthrough in particle physics came with the development of a theory to describe weak interactions. All leptons and quarks carry "weak charge" which is to the weak force as color is to strong interactions. Whereas leptons do not participate in strong interactions (since they do not carry color) and neutrinos do not experience electromagnetic forces (since they are not charged), they all participate in weak interactions. There are two types of weak interactions: charged (mediated by $W^{\pm}$) and neutral (mediated by the Z). The weak fine structure constant, $\alpha_w = 1/29$, is larger than its electromagnetic counterpart (α_{em}) by nearly a factor of five. However, the weak force is normally rather feeble because the mediating particles are very massive. In order to study the W and Z bosons in depth, accelerators must be able to run at energies above the W and Z masses. In this regime, weak

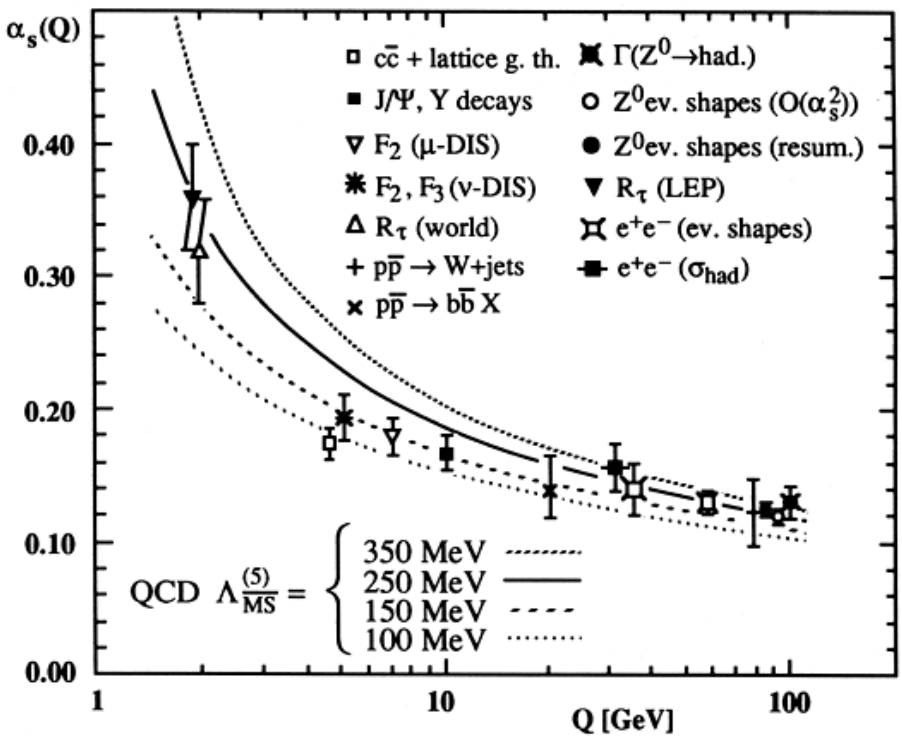

Figure 2.1. The strong coupling constant, α_s, as a function of the momentum transfer Q. At high momentum transfer, the coupling approaches zero and allows QCD to be calculable using perturbation theory. However, the coupling becomes very strong at low momentum transfer in the non-perturbative region [10].

interactions become stronger than electromagnetic interactions.

In the Standard Model, the electromagnetic and weak forces are treated as different manifestations of a single force and are described by the electroweak gauge theory. This combined interaction is produced by a local gauge invariance under the group $SU(2)_L$ of weak isospin $\times$ $U(1)$ of weak hypercharge. Inclusion of the $U(1)$ group was essential in order to incorporate the electric charge (Q) and unify the two interactions [7]. The connection between electric charge, weak isospin(I), and hypercharge(Y) is given by:

$$Q = I_3 + Y.$$

The subscript L for the $SU(2)$ group indicates that these gauge transformations only operate on left handed particles. The relevant lepton doublets and singlets are:

$$\begin{pmatrix} \nu_e \\ e \end{pmatrix}_L, \begin{pmatrix} \nu_\mu \\ \mu \end{pmatrix}_L, \begin{pmatrix} \nu_\tau \\ \tau \end{pmatrix}_L, e_R, \mu_R, \tau_R$$

where the subscripts R and L refer to the right and left handed particles respectively. Similarly, the doublets and singlets for quarks in the electroweak interaction are:

$$\begin{pmatrix} u \\ d' \end{pmatrix}_L, \begin{pmatrix} c \\ s' \end{pmatrix}_L, \begin{pmatrix} t \\ b' \end{pmatrix}_L, u_R, d'_R, c_R, s'_R, t_R, b'_R.$$

This 'unbroken' model for the electroweak interaction has an inherent deficiency in that the $W^\pm$ and Z bosons (as well as the photon) are massless. This problem is remedied with the spontaneous symmetry breaking of the 'Higgs mechanism'. This phenomenon enables the $W^\pm$ and Z to acquire mass while keeping the photon massless. Such a spontaneous symmetry breaking can be illustrated by considering a circle. The circle, drawn on a rubber sheet, is symmetrical when rotated about its center [11]. However, if the sheet is stretched such that the circle becomes an oval, rotation about the center does not match the same shape as the original

position. This is an analogy for the electroweak spontaneous symmetry breaking where the Higgs boson performs the stretching. To date the Higgs boson has not been experimentally detected, although efforts to do so make up a significant part of collider physics programs.

An interesting aspect of electroweak interactions is that flavor is *not* conserved. For example, a down quark converts into an up quark with the emission of a W^-. Additionally, although leptonic weak interactions operate strictly within each generation (for example: $W^- \rightarrow \overline{\nu_e} + e^-$), quark generations can be crossed. In other words, a strange quark can convert into an up quark (as in the decay of the Λ particle: $\Lambda(uds) \rightarrow p(udu) + \pi^-(\overline{u}d)$). The quark generations are skewed for weak interactions. Rather than the standard families,

$$\begin{pmatrix} u \\ d \end{pmatrix} \begin{pmatrix} c \\ s \end{pmatrix} \begin{pmatrix} t \\ b \end{pmatrix}$$

the weak force couples to

$$\begin{pmatrix} u \\ d' \end{pmatrix} \begin{pmatrix} c \\ s' \end{pmatrix} \begin{pmatrix} t \\ b' \end{pmatrix}$$

where d',s', and b' are linear combinations of the physical quarks d, s, and b. The specific combinations are given by the 3×3 Kobayashi-Maskawa matrix as follows:

$$\begin{pmatrix} d' \\ s' \\ b' \end{pmatrix} = \begin{pmatrix} V_{ud} & V_{us} & V_{ub} \\ V_{cd} & V_{cs} & V_{cb} \\ V_{td} & V_{ts} & V_{tb} \end{pmatrix} \begin{pmatrix} d \\ s \\ b \end{pmatrix}$$

where V_{ud} and V_{us} measure the coupling of u to d and u to s, respectively. If this were the unit matrix, then $d' = d$ and so forth; however, it is approximately:

$$\begin{pmatrix} \sim 1 & \epsilon & \epsilon^3 \\ \epsilon & \sim 1 & \epsilon^2 \\ \epsilon^3 & \epsilon^2 & \sim 1 \end{pmatrix}$$

where $\epsilon \cong 0.22$. Note that V_{us} is nonzero which makes cross-generational processes such as the Λ decay possible.

2.2 W and Z Boson Production

At hadron colliders like the Fermilab Tevatron, W and Z bosons are produced primarily through $q\overline{q}$ annihilation. Since the (anti)proton contains two (anti)up quarks and a (anti)down quark, these are the partons involved. Examples of W^- and Z production are ($\overline{u}$ + d $\rightarrow W^-$) and ($\overline{d}$ + d $\rightarrow Z$), respectively. The lowest order diagrams for similar production processes are shown in Figure 2.2. The cross section for $p\overline{p}$ to produce $u\overline{d} \rightarrow W^+$ is given by [8]:

$$\sigma = \int dx_1 dx_2 F_{u/p}(x_1) F_{\overline{d}/\overline{p}}(x_2) \hat{\sigma}(u\bar{d} \rightarrow W^+), \tag{2.1}$$

where $F_{u/p}(x_1)$ is the parton distribution function (PDF) which gives the probability of finding a u quark with momentum fraction (x_1) within the proton. Additionally, $\hat{\sigma}$ is the cross section for W production from the interactions of the specified partons. The total cross section is calculated by integrating over all allowed parton momentum fractions (x_1 and x_2). Similarly, the cross section for $p\overline{p}$ to produce $u\overline{u} \rightarrow Z$ is given by:

$$\sigma = \int dx_1 dx_2 F_{u/p}(x_1) F_{\overline{u}/\overline{p}}(x_2) \hat{\sigma}(u\bar{u} \rightarrow Z). \tag{2.2}$$

W and Z bosons can also be produced in conjunction with a strongly interacting particle (a gluon or quark) in the final state. The former occurs when one of the two incoming quarks radiates a gluon before it is annihilated. In order to have a quark in the final state, a quark and gluon are the initial partons. The gluon then pair produces into a $q'\bar{q''}$, and a standard $q'\bar{q}$ interaction produces the W (or Z). The quark ($\bar{q''}$) not involved in this process then hadronizes and is identified as a jet.

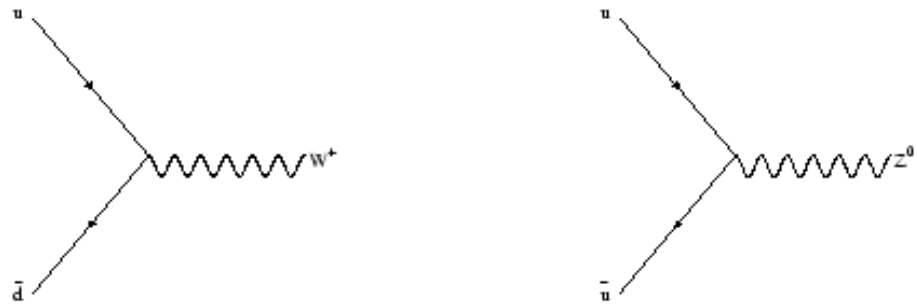

Figure 2.2. Leading order W and Z boson production mechanisms are shown.

2.3 W and Z Boson Decay

Both the W and Z bosons decay a very short time after they are produced. Therefore, the presence of these particles must be inferred by detecting their decay products. The W boson decays into quark-antiquark and lepton-neutrino pairs. The possible decay products from a W^+ are:

$$e^+\nu_e, u\bar{d}, \mu^+\nu_\mu, c\bar{s}, \tau^+\nu_\tau,$$

where the decay to $t\bar{b}$ is forbidden due to conservation of mass. The $q\bar{q}$ decays have the largest cross section (branching ratio of $\sim 67\%$ compared to $\sim 33\%$ for leptonic decays). However, the presence of two jets in the detector is the signature for this type of event. Unfortunately, this channel suffers from a very large background from dijets produced directly through QCD interactions, making it difficult to identify the W decays. As a result, focus is turned to the leptonic decays. The tau channel suffers from the same problem as the hadronic decay channels. The τ decays most often into hadrons, again making it difficult to separate the signal from the large QCD background. The muon channel is not used for the diffractive

W search for two reasons. First, the DØ detector does not have good momentum resolution for high p_T muons. Second, the muon event triggers explicitly required activity throughout the detector, effectively removing any rapidity gap events from the sample. Z boson decay processes parallel those of the W as far as analysis utility is concerned. Therefore, the electron decay channel is used to identify diffractively (and non-diffractively) produced W and Z bosons. The leading order diagrams for these decays are shown in Figure 2.3. For the ee processes, both electrons are detected directly; however, in $e\nu$ processes only the electron can be detected directly. The presence of the neutrino must be inferred from an imbalance in event momentum.

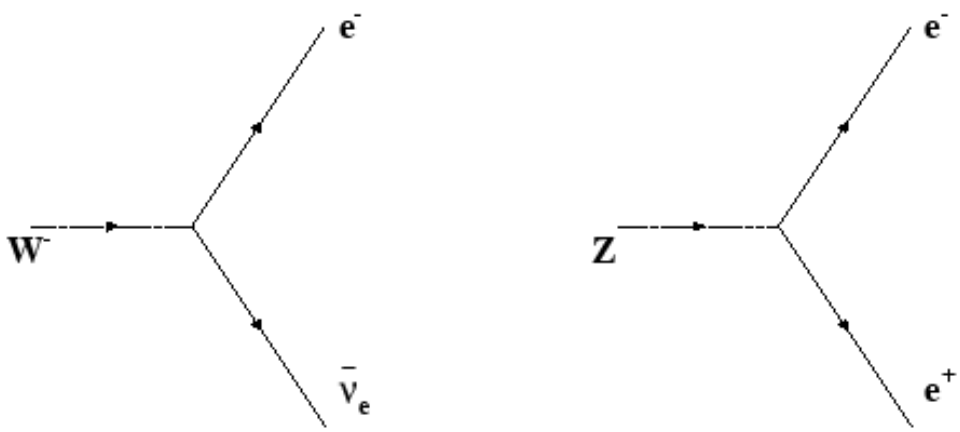

Figure 2.3. Leading order leptonic W and Z boson decay mechanisms are shown, specifically decays involving the electron and its neutrino ($W \to e\nu$ and $Z \to ee$). These are the most easily detected decay paths for the W and Z bosons at DO; however, there are other decays available for both the W and Z.

2.4 Soft Diffraction

Although QCD describes high energy interactions well by using perturbation theory, it is not able to do so for low momentum transfer interactions. This gap in

knowledge needs to be eliminated because these processes are an integral part of particle physics. At accelerators, a large portion of hadron-hadron collisions are soft interactions such as elastic scattering. Furthermore, every interaction (hard or soft) involves hadronization which is also a soft process.

The differential cross section for proton-proton elastic scattering (dσ/dt) is shown in Figure 2.4. The exponential behavior of this cross section at small momentum transfer can be related to the scattering of light by a small absorbing disk. The intensity of light (as a function of angle) scattered from such a disk is given by

$$\frac{I}{I_o} = \frac{[2J_1(x)]^2}{x} \cong 1 - r^2(k\theta)^2 \tag{2.3}$$

where k is the wave number of the photons, r is the radius of the disk, and ($x = krsin\theta \cong kr\theta$). The cross section for elastic scattering can be described in a similar manner by

$$\frac{d\sigma/dt}{(d\sigma/dt)_{t=0}} = e^{bt} \cong 1 - b(p\theta)^2 \tag{2.4}$$

where p is the momentum of the incident proton, and $t = -(p_f - p_i)^2$ is the four-momentum transfer squared. A comparison between these two equations relates the radius of interaction to the slope of the cross section (b = $r^2/4$). For $r = 1/m_\pi$, which is the typical radius of strong interactions, b = 12.5 $(GeV/c)^{-2}$. This slope is well within the range measured for pp elastic scattering at high energies [12]. As in the diffraction of light, the slope reflects the size of the scattering object. This parallel between the two processes led to the 'diffractive' nomenclature for events in which one or both of the incident hadrons survive the interaction intact.

Diffractive processes make up a large portion of the total cross section for hadron-hadron collisions. In fact, in high energy $p\overline{p}$ collisions, approximately 40 percent of the total cross section is due to elastic or diffractive scattering [12] (see Figure 2.5).

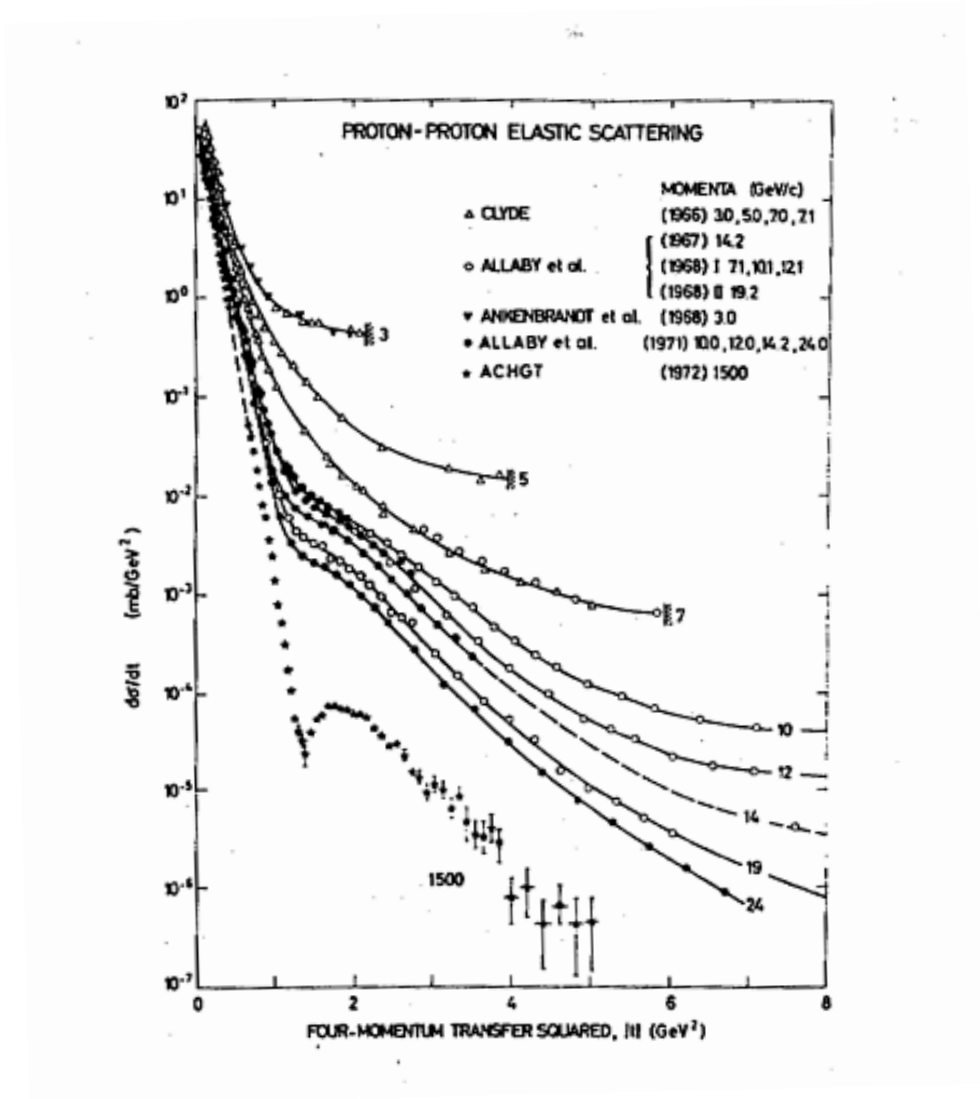

Figure 2.4. Proton-proton elastic cross section vs four-momentum transfer squared at several incident proton momenta. A classical diffraction pattern emerges as the energy increases [12].

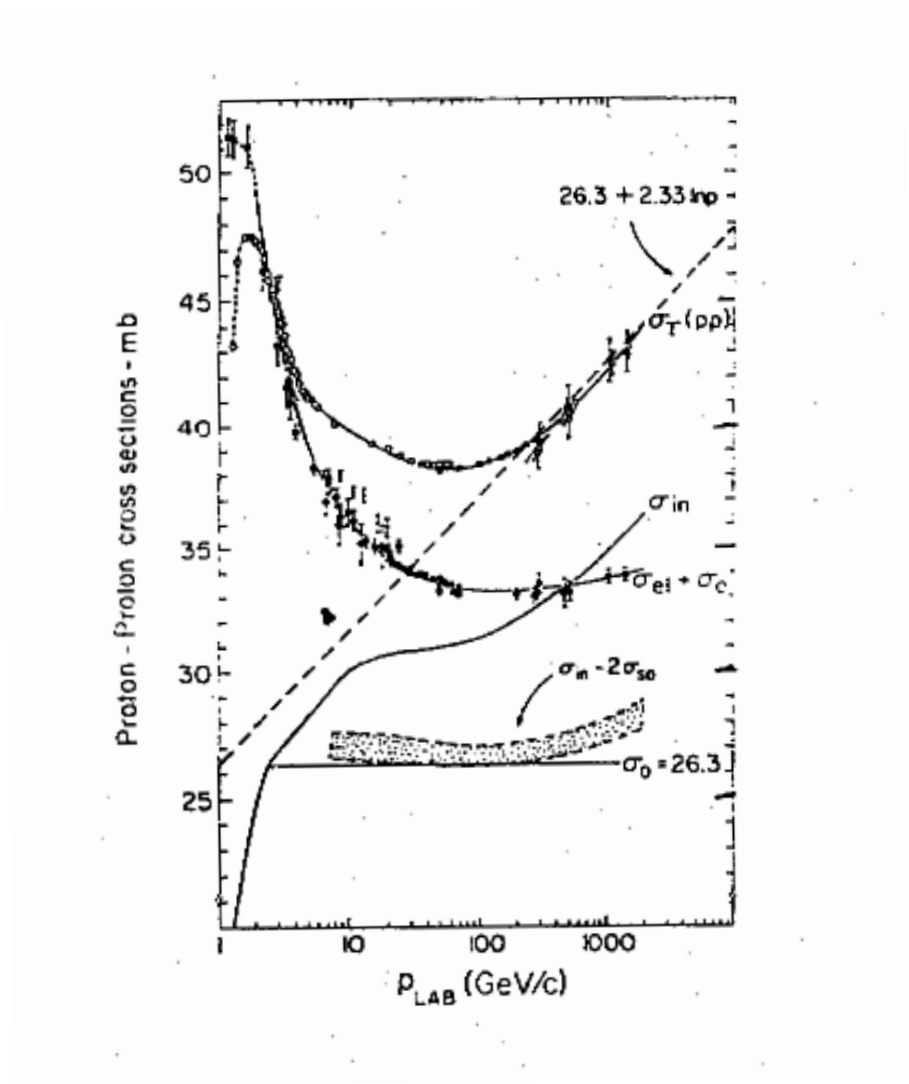

Figure 2.5. Proton-proton cross sections as a function of laboratory momentum are shown. The total cross section is shown as well as those for only inelastic and elastic processes [12].

Many features of hadronic diffraction can be described with Regge theory, which considers strong interactions as the exchange of particle trajectories. This theory, which predates QCD, also provided a mechanism for organizing particles into sequences. This grouping was based on the concept that particles with increasing mass (m_i) and spin (σ_i) represent resonances along a Regge trajectory $l = \alpha(t)$ where t is the square of the center of mass energy such that $\alpha(m_i^2) = \sigma_i$. The most common Regge trajectories are as follows:

$$\text{Pomeron: } \alpha_P(t) \cong 1 + \alpha'_P(t)t$$

$$\text{Reggeon: } \alpha_R(t) \cong 0.5 + t$$

$$\text{Pion: } \alpha_\pi(t) \cong 0.0 + 0.9t.$$

Experimental results support the hypothesis that diffractive processes are dominated by pomeron exchange.

At the Tevatron, diffraction occurs when the proton and antiproton interact via the exchange of the pomeron which is a color singlet. As such, the pomeron has the quantum numbers of the vacuum with no charge, isospin, baryon number, or color. In fact, the pomeron must be colorless or the p and $\overline{p}$ would not survive even the elastic scattering process, since the outgoing particles would then also have color (see Figure 2.6). In reality, there is no color line between the pomeron and the outgoing p ($\bar{p}$), which leads to suppression of particle production. This characteristic event topology can be used to identify diffractive events.

2.5 Hard Diffraction

In hadron collisions, soft diffractive processes such as elastic scattering are well described by pomeron exchange in Regge theory [4], yet the nature of this exchanged object is not well understood. In an attempt to better understand the pomeron,

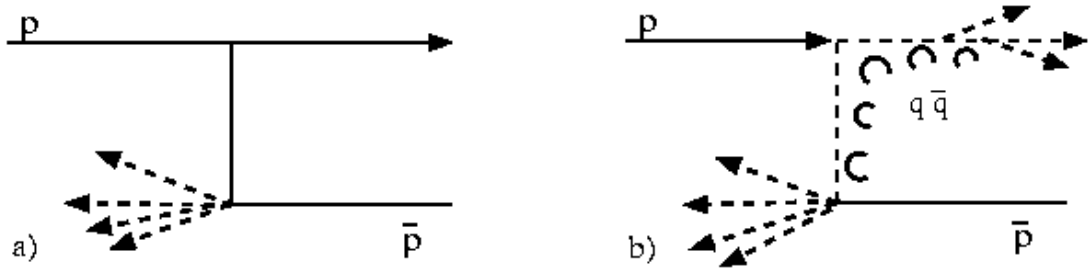

Figure 2.6. Diffraction occurs through the exchange of a color singlet. As a color singlet, the pomeron has the quantum numbers of the vacuum. It must be a colorless object in order for the proton and/or antiproton to survive the interaction. a)Single diffraction where the $\overline{p}$ breaks apart. b) If the pomeron had color, the outgoing proton would also have color. There would be color strings between the outgoing proton and the pomeron. This would lead to $q\overline{q}$ pair production along the string and the hadronization of the proton.

attention has been directed at hard diffractive events, the subset of diffractive dissociation in which a high transverse momentum scattering occurs. This new focus began when Ingelman and Schlein suggested that such hard scattering processes could provide a mechanism with which to resolve the pomeron structure [5]. Interactions between, for example, a gluon in the pomeron and a gluon in the proton leading to high p_T jets in the final state could give clues to the nature of the pomeron and test the hypothesis that it is a particle-like object.

Building on earlier suggestions that the pomeron is composed primarily of gluons [13], this initial model for diffractive hard scattering assumed that the pomeron behaves as a hadron and introduced the concept of a pomeron structure function. This provided a quantitative description of the pomeron as a combination of gluon density distributions. Ingelman and Schlein postulated two extreme pomeron structure functions: a hard gluonic structure with two gluons sharing the pomeron momentum $6\beta(1-\beta)$, and a soft gluonic structure $6(1-\beta)^5$ modeled after the gluon

structure of the proton. In each case, β is the momentum fraction of the parton (quark or gluon) with respect to the pomeron. These distributions are normalized such that the entire pomeron momentum is carried by the gluons:

$$\int_0^1 \beta f(\beta) = 1$$

Although this is a natural concept when thinking of the pomeron as a particle, it is not necessarily true. Since the pomeron is a virtual exchanged particle, the momentum sum rule might not hold.

Several experiments subsequently attempted to determine the pomeron structure. The UA8 collaboration at CERN successfully observed jets in diffractive events [14] and later inferred a hard pomeron structure [15]. Zeus [16] and H1 [17] also found that a substantial fraction of the pomeron is hard, meaning that the parton involved in the hard scattering carries a considerable fraction of the total momentum. Additionally, deep inelastic scattering measurements showed that there is a hard quark component to the pomeron structure [18]. As the experimental results were examined, it became evident that more information was needed in order to effectively describe the quark/gluon composition of the pomeron. Working toward this goal, Bruni and Ingelman proposed the study of diffractively produced W and Z bosons [19]. These electroweak hard scattering processes provide a probe of the quark component of the pomeron, whereas the gluon component is measured through strong hard scattering processes like diffractive dijet production.

This analysis measures the rate of diffractive W and Z boson production in $p\bar{p}$ collisions at the Fermilab Tevatron; furthermore, an attempt is made to probe the quark component of the pomeron and to provide insight into the validity of the Ingleman and Schlein model.

Diffractive W and Z production can be described as occurring in two stages (see Figure 2.7): first, the incident proton(antiproton) 'emits' a color-singlet pomeron

with a small squared momentum transfer

$$t = -(p_f - p_i)^2.$$

The pomeron carries only a small fraction of the initial proton momentum,

$$\xi = 1 - x_p$$

where ($x_p = p_f/p_i$) and the proton remains intact throughout the interaction. In the second part of the interaction, a parton from the pomeron interacts with a quark or gluon in the antiproton(proton) in a large momentum transfer hard scatter producing a W or Z boson. For these high p_T interactions, individual coupling of a gluon constituent in the pomeron to a parton in the proton is assumed; whereas for low momentum transfer processes like elastic scattering, the pomeron is thought to interact as one unit. Describing hard diffraction as two distinct steps is referred to as factorisation. It is thought to be a good approximation of the interaction because pomeron phenomenology provides a good description of elastic scattering and diffractive dissociation.

Factorisation allows the cross section for diffractive W and Z production to be expressed as

$$\frac{d\sigma(\bar{p}p \to p + W/Z + X)}{dx_{\mathrm{P}}dtdx_1dx_2} = f_{\mathrm{P/p}}(x_{\mathrm{P}}, t)\frac{d\sigma(\bar{p}\mathrm{P} \to \mathrm{W/Z + X})}{dx_1dx_2}. \tag{2.5}$$

The first term is the pomeron 'flux factor' and it gives the probability that the proton (antiproton) will emit a pomeron. This flux factor can be taken as the ratio of the single diffractive cross-section and the pomeron-proton total cross section [5]

$$f_{\mathrm{P/p}}(x_{\mathrm{P}}, t) = \frac{d\sigma/dx_{\mathrm{P}}dt}{\sigma_{\mathrm{Pp}\to\mathrm{X}}}. \tag{2.6}$$

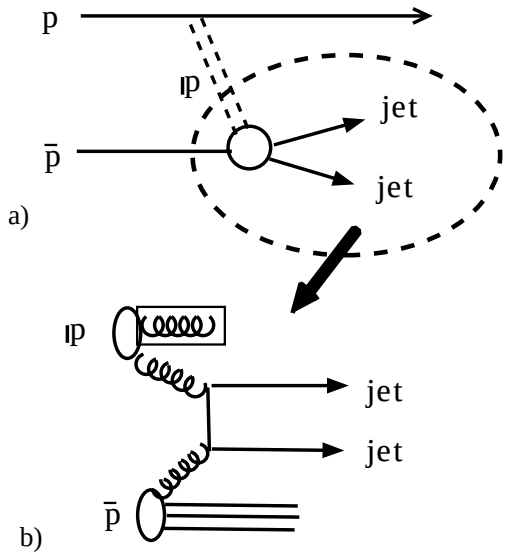

Figure 2.7. Factorization allows pomeron exchange to be described as two distinct interactions. a) First, the proton(antiproton) 'emits' the pomeron, b) then a parton from the pomeron participates in a hard scatter with a parton from the antiproton(proton).

It is estimated using elastic and single diffractive scattering data and Regge theory. The second term is the hard pomeron-particle scattering cross section. It can be written as

$$\frac{d\sigma(\bar{p}\mathrm{P} \rightarrow \mathrm{W/Z+X})}{dx_1 dx_2} = f_{\mathrm{q/P}}(x_1) f_{\mathrm{q/p}}(x_2) \hat{\sigma}(\bar{q}q \rightarrow W/Z) \tag{2.7}$$

when a quark from the pomeron interacts with a quark from the proton, or

$$\frac{d\sigma(\bar{p}\mathrm{P} \rightarrow \mathrm{W/Z+X})}{dx_1 dx_2} = f_{g/\mathrm{P}}(x_1) f_{\mathrm{q/p}}(x_2) \hat{\sigma}(gq \rightarrow q + W/Z) \tag{2.8}$$

when a gluon from the pomeron interacts with a quark from the proton. This scattering cross section is assumed to be independent of the initial small momentum transfer t. It involves the proton and pomeron structure functions, both of which are given as densities of quarks and/or gluons, and the appropriate parton level cross section($\hat{\sigma}$). The diffractive W boson is produced at leading order by the process $q\overline{q} \rightarrow W$, where one quark comes from the pomeron (see Figure 2.8). The process $gq \rightarrow Wq$ is suppressed by order α_s and results in a final state jet accompanying the W(see Figure 2.9).

In calculating the diffractive W and Z boson production cross sections, Bruni and Ingelman proposed three different possible pomeron structure functions:

$$\beta f_{g/\mathrm{P}}(\beta) = 6\beta(1-\beta) \quad where \quad (<\beta>= 1/2)$$
$$\beta f_{g/\mathrm{P}}(\beta) = 6(1-\beta)^5 \quad where \quad (<\beta>= 1/7)$$

the same hard and soft gluonic structure functions given by Ingelman and Schlein, and an additional hard quark structure

$$\beta f_{q/\mathrm{P}}(\beta) = \tfrac{6}{4}\beta(1-\beta) \quad where \quad (<\beta>= 1/2)$$

As in the hard gluon case, the quarks in the last structure function share the pomeron momentum equally. Again, the momentum sum rule is assumed.

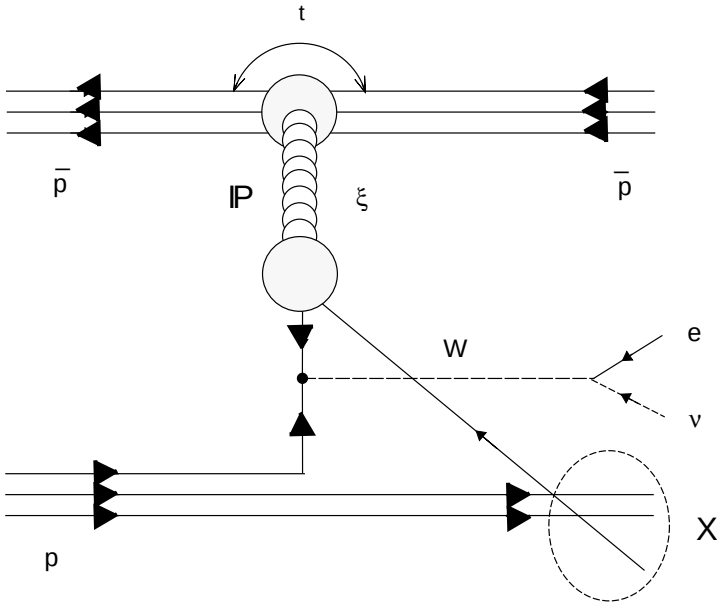

Figure 2.8. Diffractive W production based on a hard quark pomeron structure.

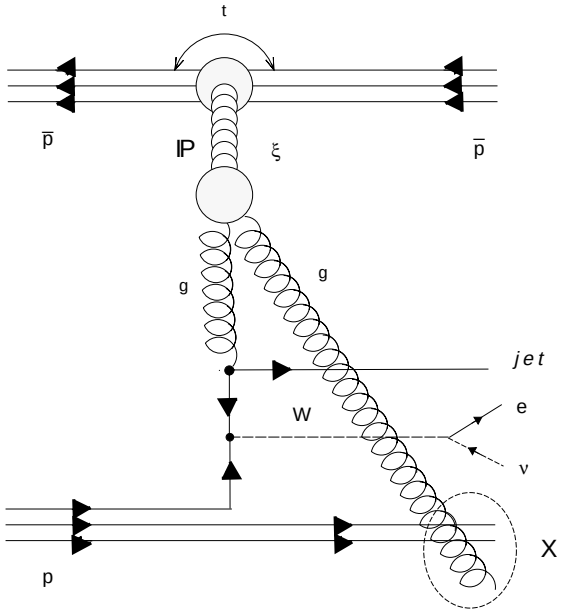

Figure 2.9. Diffractive W production based on a hard gluon pomeron structure.

The observable diffractive W boson fraction:

$$\frac{W_{diffractive} \rightarrow e\nu}{W_{all} \rightarrow e\nu} \tag{2.9}$$

produced at the Tevatron was predicted to be $\sim 17\%$ for a hard quark pomeron and $\sim 1\%$ for a hard gluon pomeron [19]. Similarly, the observable diffractive Z boson fraction:

$$\frac{Z_{diffractive} \rightarrow e^+e^-}{Z_{all} \rightarrow e^+e^-} \tag{2.10}$$

was predicted to be $\sim 15\%$ and $\sim 0.6\%$ for a hard quark and hard gluon pomeron, respectively [19]. Diffractive events can be identified in two distinct ways based on their characteristic topology. Either the quasi-elastically scattered proton (or antiproton) can be detected directly with forward proton detectors (for example Roman pots), or events with a rapidity gap can be tagged. (Currently, DØ does not have the capability to tag the outgoing proton or antiproton, although it will be possible in RunII following the installation of Roman Pot detectors on either side of the interaction region [20].)

In this analysis, a diffractive W or Z candidate event is identified by the presence of a rapidity gap in the forward region of the detector. The gap is identified by a concurrent lack of activity in both the LevelØ detector and the end cap calorimeter(see Chapter 4 for details). For the purpose of this analysis, we consider the pomeron as the mechanism for diffractive W and Z production. We measure the rapidity gap fraction in data, and then compare the result to predictions made using the Ingleman and Schlein model. As mentioned above, the various pomeron models predict very different diffractive W and Z gap fractions. This difference is large enough that we should be able to tell a pomeron dominated by quarks from one dominated by gluons. Combining the information from diffractive W and Z pro-

duction with that from complementary diffractive dijet and heavy flavor production will give an even better picture of the pomeron structure.

2.6 Soft Color Model

In the past few years, a new mechanism for the production of rapidity gap events has been developed. This soft color interaction model [21] [22] [23] [24] does not involve the concept of a pomeron. Rather, it explains rapidity gap events by introducing non-perturbative soft color interactions (SCI) between the partons and the proton or antiproton remnant. These SCI change the color of the partons (but not the momentum), thus altering the color structure of the event and creating rapidity gaps. Figure 2.10 shows a typical event without soft color interactions (a), as well rapidity gap events resulting from SCI beginning with the same event. Although it is not explicitly compared to the W and Z data in this analysis, the Soft Color Model does provide an alternate mechanism for rapidity gap production.

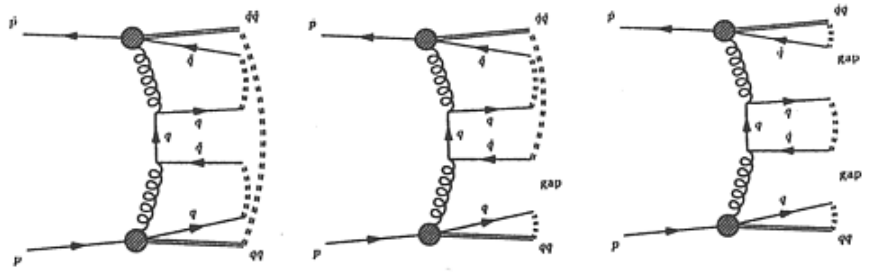

Figure 2.10. Rapidity gap events created through non-perturbative Soft Color Interactions (b,c) through a modification of (a) [25].

CHAPTER 3

THE DØ DETECTOR

The 5500 ton, 40 foot tall DØ detector is a huge monster of a machine designed to record extremely complicated processes on a minute scale with an impressive degree of accuracy and detail. It is a multipurpose detector used to study various phenomena resulting from high energy,$\sqrt{s}$ = 1.8 TeV, $p\overline{p}$ collisions. The detector is geared primarily toward the investigation of large p_T phenomena and high mass states. Observation of the top quark, precision measurements of W and Z bosons, production of b-quark hadrons, testing of perturbative QCD, and the search for new physics beyond the standard model were all within the design goals. In order to successfully study such processes, the detector was designed to provide excellent identification of electrons and muons along with good measurement of high p_T jets and missing transverse energy which indicates the presence of non-interacting particles like neutrinos.

The DØ detector is made up of three major components: the central detector, the calorimeter, and the muon spectrometer (see Fig. 3.1). Four detector systems make up the central detector (CD) which is used for vertex finding, particle tracking, and particle identification. The vertex drift chamber (VTX), the innermost of these four systems, is located immediately outside the beam pipe. Continuing radially out from this device, one finds the transition radiation detector (TRD) and the central drift chamber (CDC). Two forward drift chambers, oriented perpendicular to the beam pipe and located at each end of the CDC, complete the central detector. The

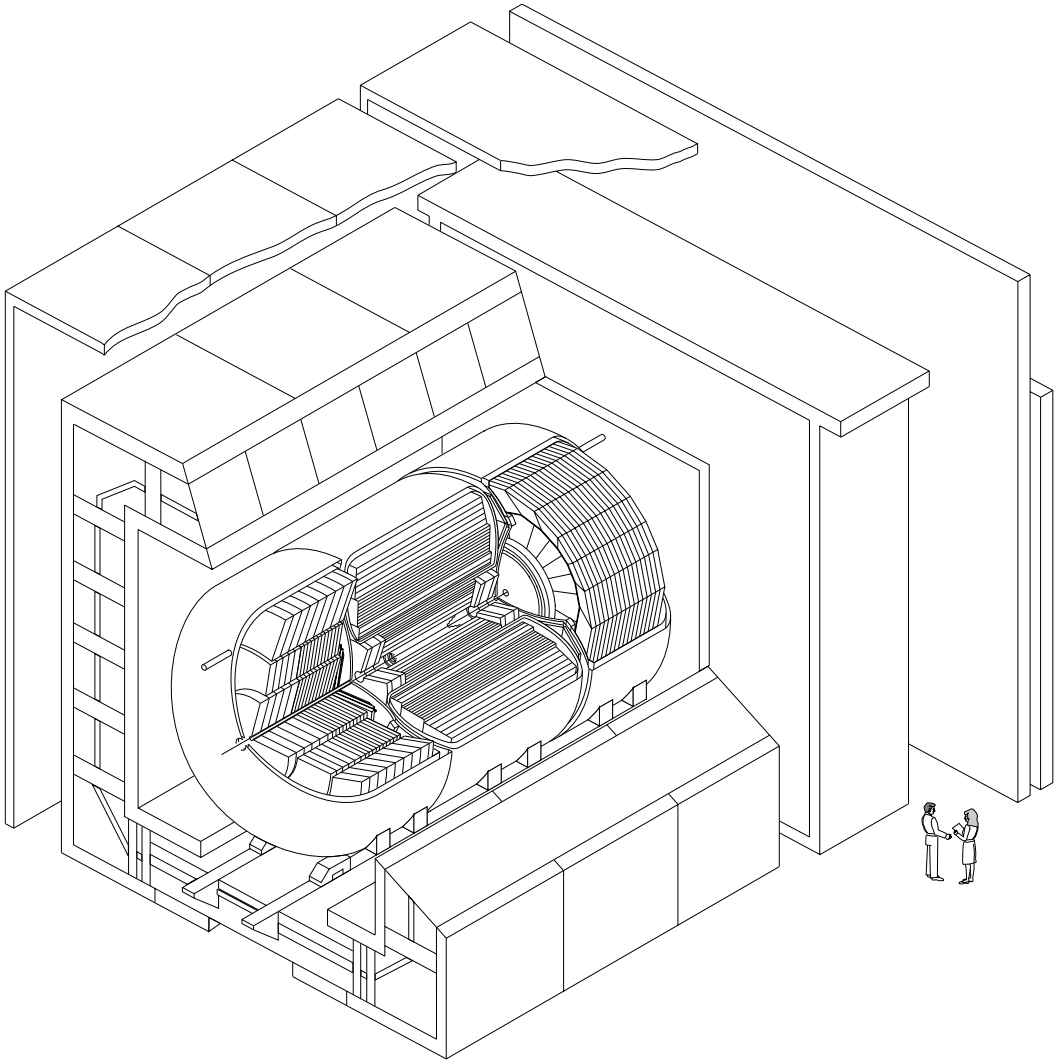

Figure 3.1. Isometric view of the DØ detector showing the three main systems: the central tracking and vertexing detector, the calorimeter, and the muon system.

liquid-argon/uranium sampling calorimeter surrounds the CD and provides crucial information necessary for many physics analyses. Since there is no central magnetic field available to measure the momentum of charged particles, the calorimeter provides the only energy measurement for electrons, photons, and jets. Additionally, it aids in particle identification and is responsible for determining the balance of transverse energy in events. The third significant part of the DØ detector is the muon spectrometer which is composed of proportional drift tube chambers (PDTs) and thick magnetized iron absorbers. This outermost system is responsible for the identification of muons and the measurement of their momenta and trajectories.

In addition to these major systems, there are several supplemental detectors used to compensate for the lack of active instrumented material in the regions between the central and end calorimeter cryostats. These include the scintillation counter arrays of the intercryostat detectors (ICD) mounted on the front surface of the end calorimeters, and the massless gap detectors located within both the central and end calorimeters. Combining these detectors provides a good approximation of the DØ sampling of electromagnetic showers. The LevelØ scintillation detectors surround the beam pipe and are also mounted on the front surface of the end calorimeters. These scintillators are typically used to identify the presence of an inelastic $p\overline{p}$ collision as part of the DØ trigger system. A detailed description of the full DØ detector can be found in Ref [26]. The following sections will focus on elements of the detector which contributed directly to this analysis.

3.1 Coordinate System

Several different coordinate systems can be used to describe the DØ detector including Cartesian (x,y,z), cylindrical (r,ϕ,z), spherical (r,ϕ,θ), and a combination of these (z,η,ϕ). Each of these originates at the geometric center of the detector with the positive z axis in the direction of the proton (see Fig. 3.2). The positive y

axis then points vertically up, with the x axis horizontal and perpendicular to the beam pipe. The angular coordinates ϕ and θ are the aximuthal and polar angles respectively, where $\theta = 0$ along the proton beam direction.

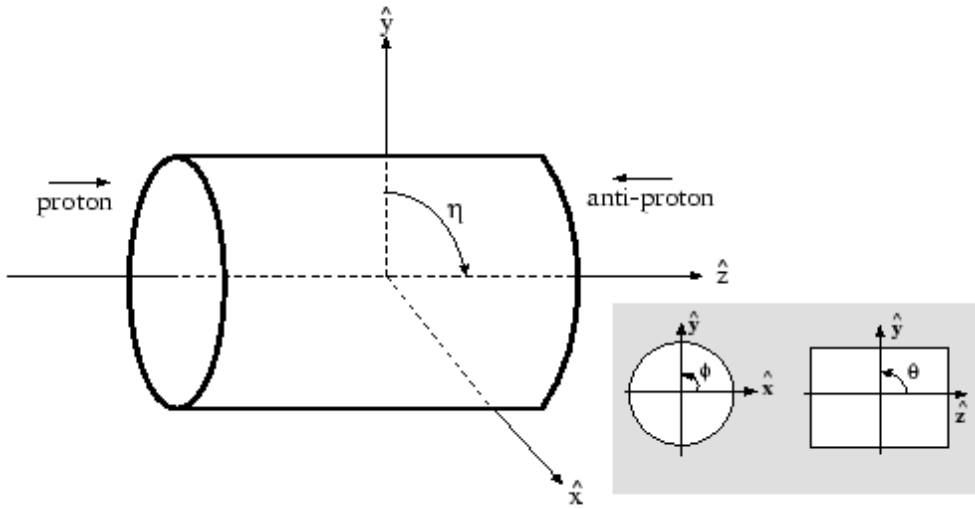

Figure 3.2. Coordinate systems for the DØ detector. The coordinates chosen to describe events are z(beamline direction), η (pseudorapidity), and ϕ (azimuthal angle).

The choice of coordinate system depends on the situation involved. For example, the geometry of the tracking and calorimetry systems is easily described by cylindrical coordinates; however, to represent an interaction at rest one would use spherical coordinates. On the other hand, if the partons in a collision carry different fractions of the initial hadron momentum, the event will not be at rest. Instead, the center of mass of the partons is boosted along the beam direction in the lab frame. This motivates the use of a coordinate system invariant under such boosts. The best coordinate system for the DØ detector is a combination of the usual options: (z,η,ϕ). The z coordinate is used primarily to determine the event vertex location along the beam pipe. The azimuthal angle, ϕ, is perpendicular to z (see Fig. 3.2). The polar

angle (θ) is replaced by η, the pseudorapidity. This is an important change because when the energy of a particle is much larger than its mass, the pseudorapidity (η) is approximately equal to the rapidity (y). Rapidity is a Lorentz invariant variable defined as:

$$y = \frac{1}{2} \ln \left(\frac{E + p_z}{E - p_z} \right) \tag{3.1}$$

where E is the total energy and p_z is the longitudinal (z) component of the particle momentum. This variable (y) provides a way in which to describe particle distributions which is invariant under longitudinal boosts of the system. At Tevatron energies, the momentum of a particle is much larger than its mass ($p^2 \gg m^2$); therefore,

$$E^2 = p^2 \Rightarrow p_z = \text{p} \cos\theta = \text{E} \cos\theta \ .$$

Using this information, rapidity becomes:

$$y = \frac{1}{2} \ln \left[\frac{E(1 + \cos\theta)}{E(1 - \cos\theta)} \right] = -\frac{1}{2} \ln \left(\frac{1 - \cos\theta}{1 + \cos\theta} \right) = -\ln \left(\frac{1 - \cos\theta}{1 + \cos\theta} \right)^{\frac{1}{2}} . \tag{3.2}$$

Finally, using the identities:

$$\sin\tfrac{\theta}{2} = \sqrt{\tfrac{1}{2}(1 - \cos\theta)} \quad \textit{and} \quad \cos\tfrac{\theta}{2} = \sqrt{\tfrac{1}{2}(1 + \cos\theta)}$$

we have the definition of pseudorapidity:

$$\eta \equiv -\ln \left(\tan \frac{\theta}{2} \right) , \tag{3.3}$$

where $\eta = 0$ at $\theta = \frac{\pi}{2}$ and η goes to infinity at the beampipe where $\theta = 0$. There is also be a distinction between η_d (detector pseudorapidity) and η (physics pseudorapidity), where the latter is used when an event vertex is displaced from the center of the detector. The 'physics coordinates' use this shifted vertex as the origin of the coordinate system.

It is also important to note that since most of the longitudinal momentum in $p\bar{p}$ collisions escapes down the beampipe, it becomes useful to work with transverse energy(E_T) and momentum(p_T). These are projections of the energy and momentum of particles onto a plane perpendicular to the beam pipe, and are particularly useful when dealing with events containing neutrinos. A neutrino is not detected directly; rather, its presence is inferred by an imbalance in momentum in the detector. Although this cannot be done with longitudinal quantities, in the transverse plane momentum and energy conservation requirements can be applied to identify the neutrino. Transverse momentum and energy are defined as:

$$p_T = p \sin\theta \quad and \quad E_T = E \sin\theta$$

where $E_T = p_T$ when $p^2 \gg m^2$. Additionally, in the limit $m \to 0$, the invariant mass of two massless particles can be written as: $M_I^2 = 2E_{T1}E_{T2}(\cosh\delta\eta - \cos\delta\phi)$ [27].

3.2 Central Tracking System

The DØ central tracking detector (CD) is made up of four separate systems, namely the vertex drift chamber (VTX), the transition radiation detector (TRD), the central drift chamber (CDC), and two forward drift chambers (FDC) (see Fig. 3.3). These central detectors are used to reconstruct the paths of charged particles through the detector and to provide event vertex information as well as particle indentification. Good two-track resolving abilities, high efficiency, and accurate measurement of energy loss due to ionization (dE/dx), are needed in order to accomplish the design goals. The latter provides distinction between single electrons and closely spaced photon conversion pairs. Note that the system operates without a magnetic field and therefore does not measure the momenta of charged particles. This task is left to the calorimeter and muon spectrometer.

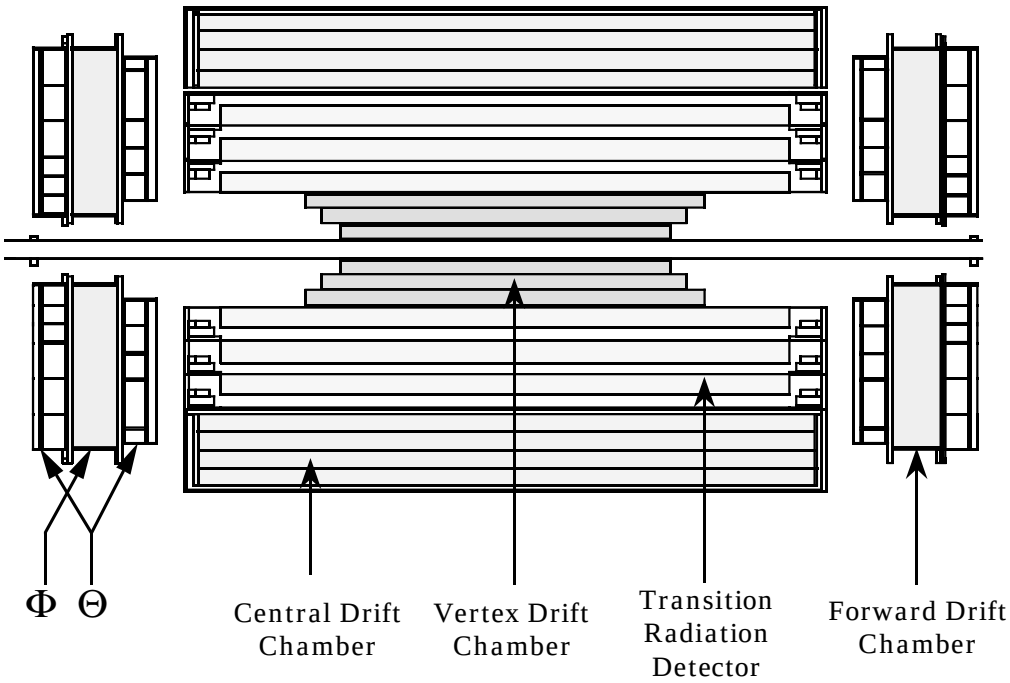

Figure 3.3. The four systems that make up the central tracking detector.

The VTX, CDC, and FDC detectors are each composed of multiwire drift chamber cells filled with a gaseous medium and arranged to measure specific geometric coordinates of charged particle tracks. The VTX contains CO_2(95%)-ethane(5%) gas, while both the CDC and FDC are filled with Ar(92.5%)-CH_4(4%)-CO_2(3%) mixed with a small amount of H_2O. Charged particles which traverse the detector volume produce an ionization trail by colliding with the atomic electrons in the gas and creating electron-ion pairs. Each cell contains a series of precisely located positively charged sense wires. When an electric field is present, the electrons drift toward these wires. The ions also move in the opposite direction, but at a slower rate due to their much higher mass. With a strong enough field, the drift electrons acquire sufficient energy to create additional ionization of the gaseous medium. When repeated, this process causes an avalanche of electron-ion pairs and amplifies the signal to a measurable current. To increase spatial resolution in a wire chamber,

the drift time (from creation to collection) of the ionization electron is recorded. At DØ the drift time is defined to be the time between the $p\overline{p}$ collision and the pulse arrival at the sense wire. Used in conjunction with the known electron drift velocity in the relevant gas, drift-time measurement allows interpolation of the track position and improves position resolution of the detector by an order of magnitude [28].

In addition to detecting the passage of charged particles, the tracking chambers must be able to distinguish between the signal from an overlay of two tracks and that from a single track. Photon conversion into an electron-positron pair would produce such an overlay, and could lead to misidentification of the photon as an electron. The amount of energy lost due to ionization of the gas in the detector is reflected by the amount of charge collected on sense wires in the tracking chambers. It follows that this loss in energy would be different for a one vs. two-track scenario, and could provide discrimination between these cases even without spatial track separation. Figure 3.4 shows dE/dx for one and two tracks in the CDC and clearly indicates the ability to separate the one and two-track signals.

The VTX, TRD, and CDC are nested concentric cylinders beginning with the vertex drift chamber located immediately outside the beam pipe. The two FDC detectors are oriented perpendicular to the beam pipe. The entire central tracking system has a radius of 75 cm and a length of 270 cm and fits in the inner cavity of the calorimeter. The VTX is the innermost DØ detector with an inner radius of 3.7 cm. It is made up of three layers of drift chamber cells aligned to give measurement of the r-ϕ coordinate (see Fig. 3.5) as well as position in z. Surrounding the VTX, the TRD is the next central tracking system detector and is used primarily to distinguish between electrons and hadrons independent of the calorimeter. It detects transition radiation X-rays produced when highly relativistic particles traverse boundaries of material with different dielectric constants [29]. The energy spectrum of the X-rays

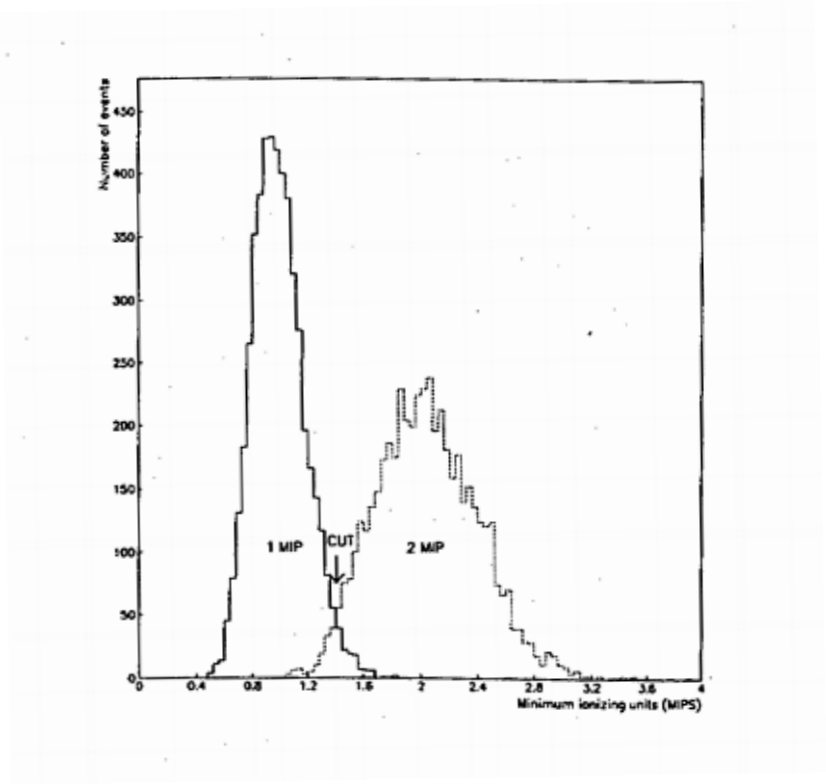

Figure 3.4. dE/dx for one and two tracks seen in the full CDC chamber [26].

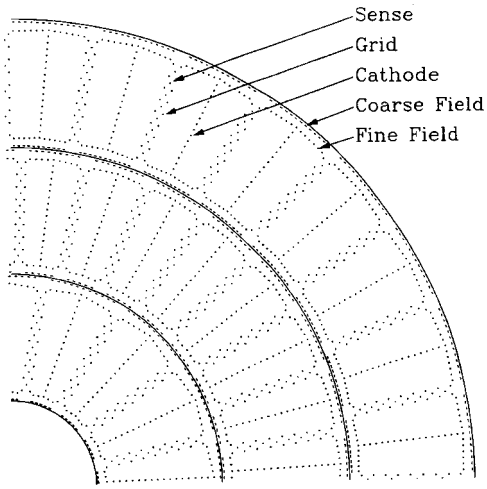

Figure 3.5. R-ϕ view of one quadrant of the VTX chambers.

produced is a function of γ, where

$$\gamma = \frac{E}{mc^2},$$

enabling the differentiation between electrons and pions due to their mass difference. Three separate units contain proportional wire chambers which detect these X-rays after their conversion within the TRD (see Fig. 3.6).

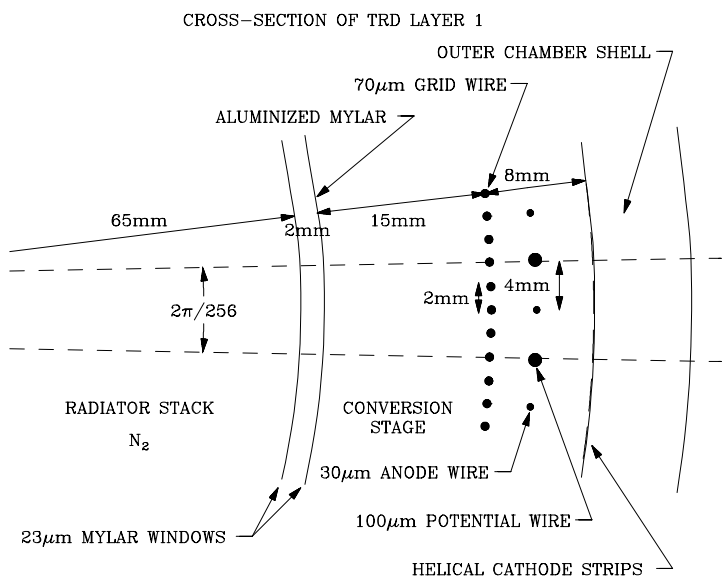

Figure 3.6. Cross section of the TRD.

Ionization is also produced when charged particles pass through the detector. Patterns in magnitude and time of arrival of charge deposited by the X-rays and from this ionization enable differentiation between electrons and pions (see figure 3.7). Located between the TRD and the central calorimeter, the CDC is the outermost large angle track detector. It is built of four concentric rings, each with 32 cells, and measures track position in r-ϕ (see Fig. 3.8) and z much like the VTX. Finally, the FDC completes the central tracking system and extends the charged particle

tracking coverage to approximately $\eta = 3.13$. Both FDC detectors are made up of three chambers: one Φ module, with radial sense wires to measure the ϕ coordinate of tracks, sandwiched between two Θ modules rotated 45 ° in ϕ with respect to each other (see Fig. 3.9). Each Θ chamber contains four quadrants with rectangular cells at increasing radii, perpendicular to the radial direction, designed to measure the θ coordinate of tracks. Detailed descriptions of the central tracking detectors can be found in [30], [31], [32], [33], [34], and [35].

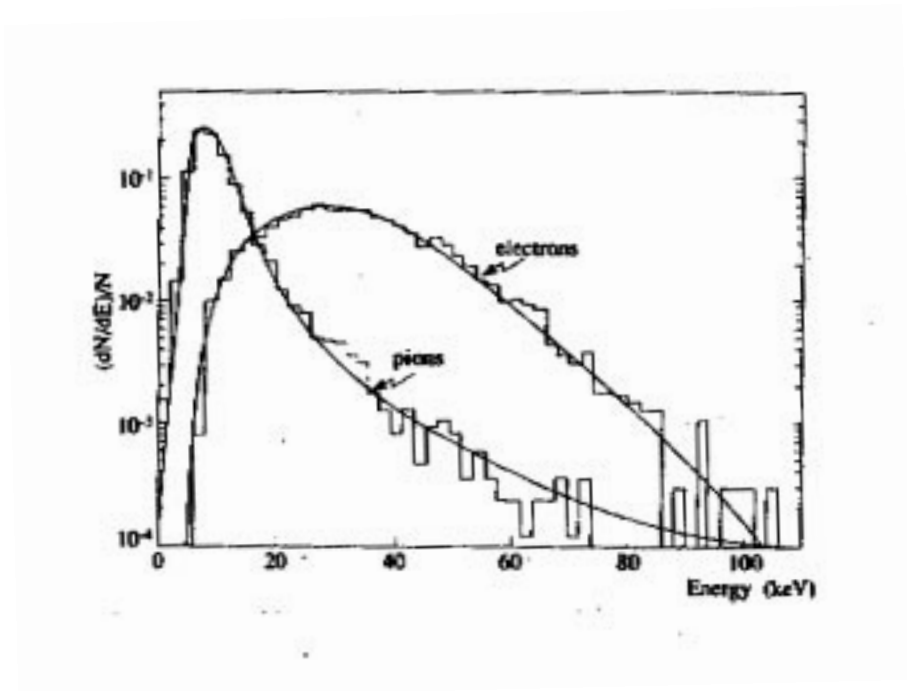

Figure 3.7. Distribution of total energy observed on the three TRD layers for both electron and pion traversals [26].

3.3 Calorimeter

The DØ detector design relies heavily on excellent calorimeter performance. Without a central magnetic field, the burden of jet, electron, and photon energy measurement falls solely on this part of the detector. In addition to providing accurate

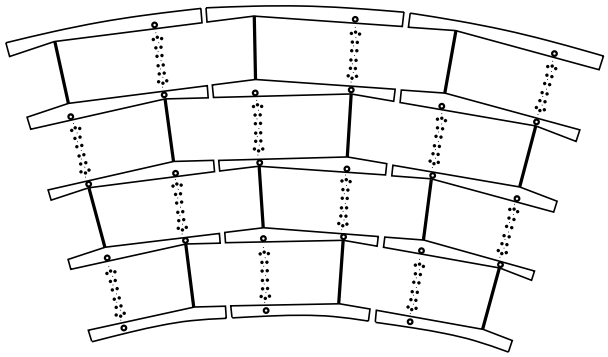

Figure 3.8. R-ϕ view of one quadrant of the CDC chambers.

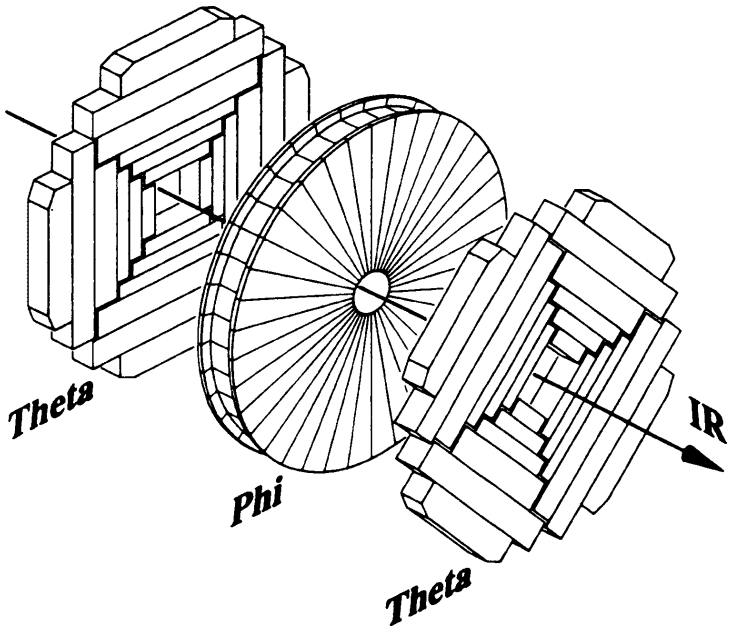

Figure 3.9. Expanded view of one set of FDC modules showing chamber orientation.

event energy and kinematic data, the calorimeter must also contribute to particle identification. Such demanding requirements call for a stable, linear, finely segmented device able to survive the high radiation environment at DØ and thick enough to completely contain hadronic showers. To meet these goals, the DØ collaboration chose a liquid argon/uranium sampling calorimeter (see Fig. 3.10). This type of calorimter is made of many layers of dense absorber alternating with an active ionizing medium. Quarks and gluons from the $p\overline{p}$ collision hadronize, creating particles which must pass through the calorimeter. These particles lose energy in the passive absorber layers, composed chiefly of depleted uranium, and in the process produce a cascade of low-energy secondary particles called a shower. The shower particles ionize the active medium, in this case liquid argon, and the energy fraction and location in (η, ϕ) space of the shower are measured. Successive sampling of this shower energy is used to infer the total energy of a particle.

As they pass through the dense absorber material of the calorimeter, high energy electrons and photons lose energy primarily through Bremsstrahlung and pair production respectively. Bremsstrahlung, or "braking radiation", occurs when an electron interacts with the electric field of the uranium atomic nuclei causing it to decelerate and emit a photon. Photons in turn perpetuate the shower by pair-producing electrons and positrons (e^+e^-). Electromagnetic (EM) showers are the result of an alternating sequence of these processes: an incident electron loses energy by emitting an energetic photon which then converts into an e^+e^- pair leading to another set of photon emissions. Each successive interaction increases particle multiplicity exponentially while decreasing the average energy of a shower particle. The cascade continues until this average energy drops to a point where other loss mechanisms dominate the interaction and further multiplication stops. The energy loss of electromagnetic particles depends on the radiation length (X_0) of the detector

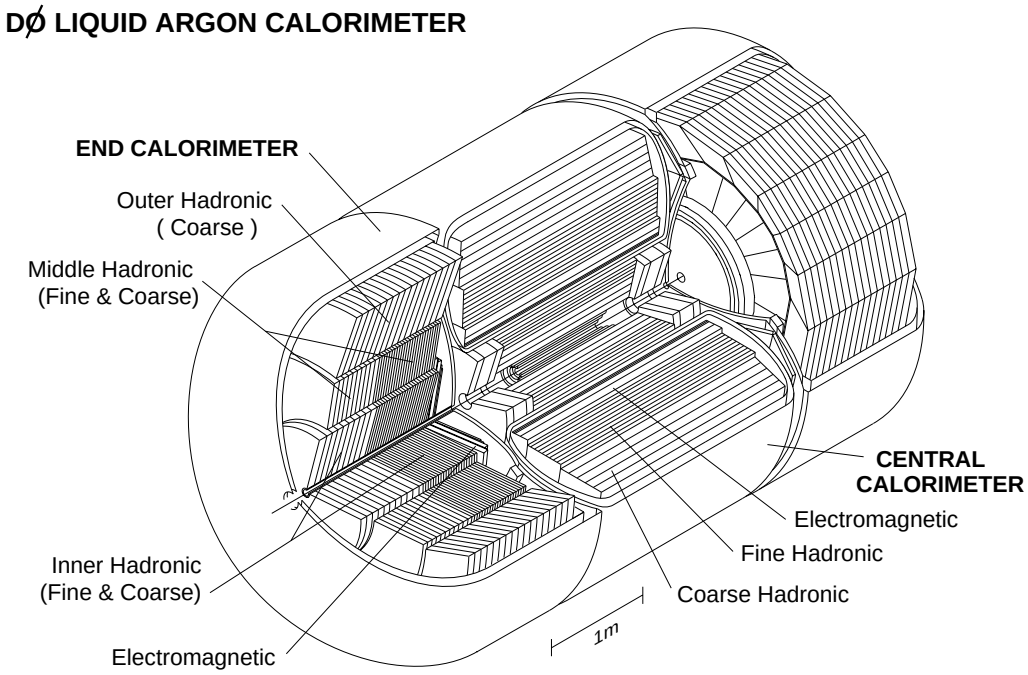

Figure 3.10. An isometric view of the DØ calorimeter which is separated into the central cryostat (CC) and two end cryostats (EC). The central tracking system is shown in the center of the calorimeter, surrounded by the EM and hadronic calorimeter.

material as follows:

$$\frac{dE}{E} = \frac{dx}{X_0},$$

where X_0 can be approximated as $X_0 = 180A/Z^2$ g/cm^2 [28]. The radiation length of uranium is 0.32 cm while $X_0 = 14$ for liquid argon. Typically, 25-30 X_0 are needed to completely contain an electromagnetic shower [36].

Strongly interacting particles also cascade in the detector, but these high energy hadrons interact with the uranium in a much different manner than the electromagnetic particles. Hadrons lose energy through successive inelastic collisions with atomic nuclei and the prolific production of secondary hadrons like pions and kaons. These secondary particles interact in the same way, creating a hadronic shower in the calorimeter. Longitudinal development of these showers depends on the nuclear absorption length, λ, (or interaction length) of the material just as EM shower length scales with the radiation length (X_0). However, for uranium, $\lambda \approx 10.5$ cm which means that hadronic showers are much longer than EM showers of the same initial energy. As a result, hadronic calorimeters are usually much larger than their electromagnetic counterparts, especially since 8-10 λ are needed to completely contain hadronic showers.

The DØ calorimeter is divided into three separate cryostats: the central calorimeter (CC) and a pair of end cap calorimeters (ECN and ECS). The CC and EC cryostats are 306 cm and 263 cm long, respectively, with an outer diameter of 518 cm. The cryogenic system is required to keep the liquid argon at a temperature of 78 K, and splitting it into three sections simplifies access to the inner tracking detectors. The CC is cylindrical and well-measured within the region $|\eta| \leq 1.0$. The EC devices sandwich the CC between them and physics objects can be well-measured within the region $1.5 < |\eta| < 2.5$ (see Fig. 3.11). Electrons can be measured well

within these regions which are kept away from the ICD. Additionally, at very forward rapidities uncertainties in the energy scale increase. As a whole, the calorimeter provides nearly complete pseudorapidity coverage for $|\eta| < 4.1$ and partial coverage out to $|\eta| = 5.2$. Both the EM and hadronic calorimeter provide nearly (the qualification 'nearly' is mentioned because of the ICD region) hermetic coverage out to $|\eta| = 4.0$. However, at $|\eta| = 4.1$, the EM calorimeter ends, and only the hadronic calorimeter continues out to $|\eta| = 5.2$ providing only partial calorimeter coverage.

A typical calorimeter unit cell with uranium absorber and liquid argon ionizing medium is shown in Figure 3.12. In a geometry based on EM and hadronic shower characteristics, layers of these cells are assembled in towers that extend radially outward from the interaction region. Cell widths correspond to the transverse size of these showers: approximately 1-2 cm for EM and 10 cm for hadronic showers. Typically, towers are segmented such that $\Delta\eta \times \Delta\phi = 0.1 \times 0.1$, although some layers are more finely divided to better probe shower shapes.

There are three types of modules within the calorimeter: the electromagnetic (EM), the fine hadronic (FH), and the coarse hadronic (CH). The EM calorimeter is designed to accurately measure the energy of electromagnetic particles and is separated into four longitudinal layers. In the CC, energy measurement is provided at 2.0, 4.0, 10.8, and 20.6 X_0 and in the EC at 0.3, 2.9, 10.8, and 20.1 X_0. These innermost calorimeter layers contain closely spaced thin uranium absorber plates. This spacing is possible because EM showers are relatively short. The first two layers are used to measure longitudinal shower development and to distinguish between photons and π^0s. While the other layers are segmented in the standard $\Delta\eta \times \Delta\phi = 0.1 \times 0.1$, the third is divided twice as finely (0.05×0.05) to facilitate precise shower centroid location. Attention is focused here because the average EM shower deposits most of its energy in this region. This segmentation holds true for the entire CC,

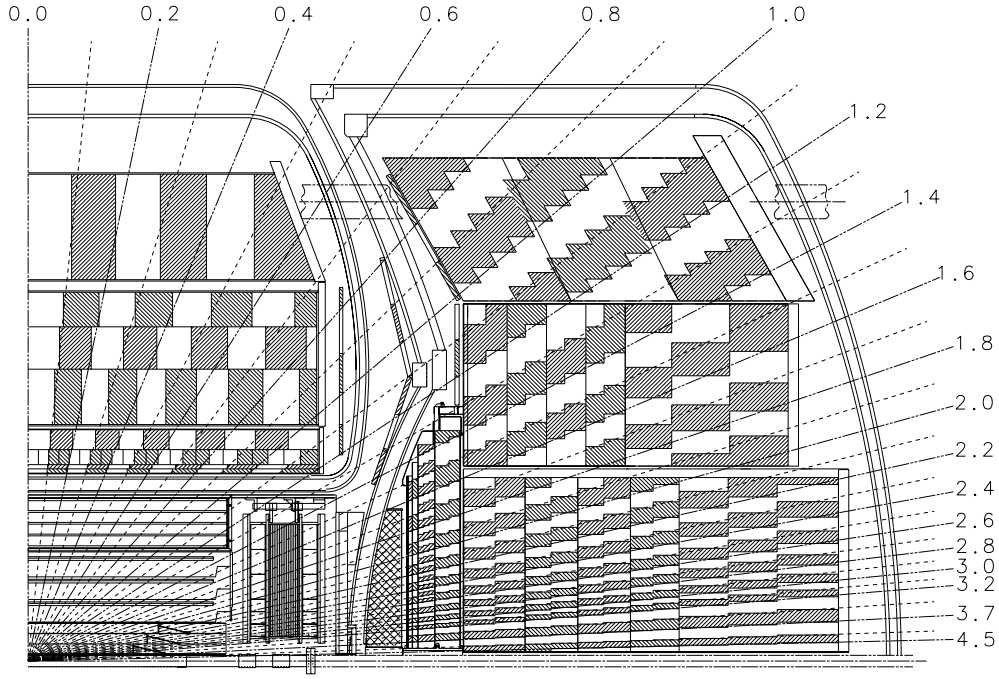

Figure 3.11. Side view of one quarter of the DØ calorimeter showing the tower structure in terms of pseudorapidity.

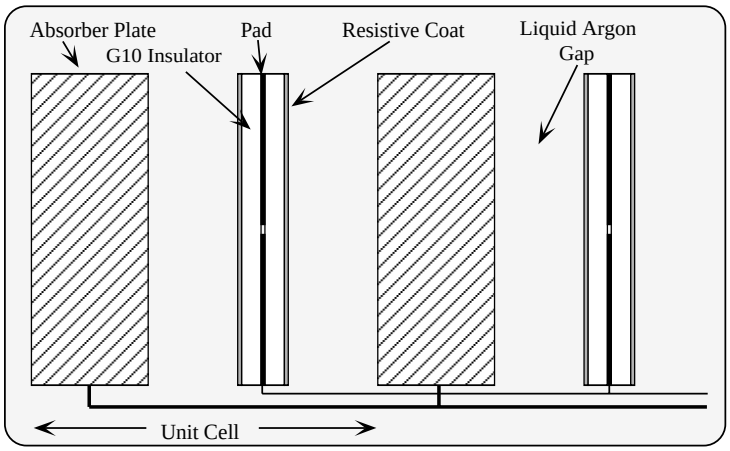

Figure 3.12. A typical calorimeter cell is shown with uranium absorber and liquid argon for the ionizing medium.

but in the EC it extends only out to $|\eta| = 2.6$. After this point, the segmentation is reduced to $\Delta\eta \times \Delta\phi = 0.1 \times 0.1$ until $|\eta| = 3.2$ at which point it decreases further. At such high values of η, the cell sizes get extremely small and it becomes necessary to group them together in these larger dimensions of $\eta - \phi$. The fourth layer completes the EM coverage of 20 X_0 and is meant to fully contain the energy from EM showers.

The outer portion of the calorimeter is devoted to the measurement of hadronic particle energy. The fine hadronic sections are made of uranium absorber plates thicker than those used for the EM cells, while the coarse hadronic portions of both the CC and EC are built with thick copper or stainless steel absorber plates. The CH sections are designed to allow sampling at the end of hadronic showers while minimizing overall calorimeter size. In the CC, there are three FH layers which provide good hadronic shower energy resolution through nearly four interaction lengths. These are surrounded by one CH layer of 3.2λ. The EC is divided into inner (IH), middle(MH), and outer(OH) hadronic modules located increasingly further from the beam pipe. Each IH and MH module has four fine hadronic sections totaling about 4λ, and a single coarse hadronic section of 4.1λ and 4.4λ respectively. The OH modules are composed entirely of three CH sections and complete the EC detectors. The total calorimeter depth equals 7.2λ in the CC at $\eta = 0$, and reaches up to 10.3λ at the smallest angles in the EC.

Figure 3.13 shows the calorimeter segmentation in detector η and IETA, the data variable used to indicate a group of calorimeter towers. The vertical axis of figure 3.13 shows the towers moving radially out through the calorimeter. The EM layers are shown first, followed by the hadronic layers. As η increases along the horizontal axis of the figure, the EC towers are shown. The gap in coverage between the CC and EC can be seen, as well as the ICD and massless gap detectors providing supplemental coverage in this region of η_d. The towers have the standard

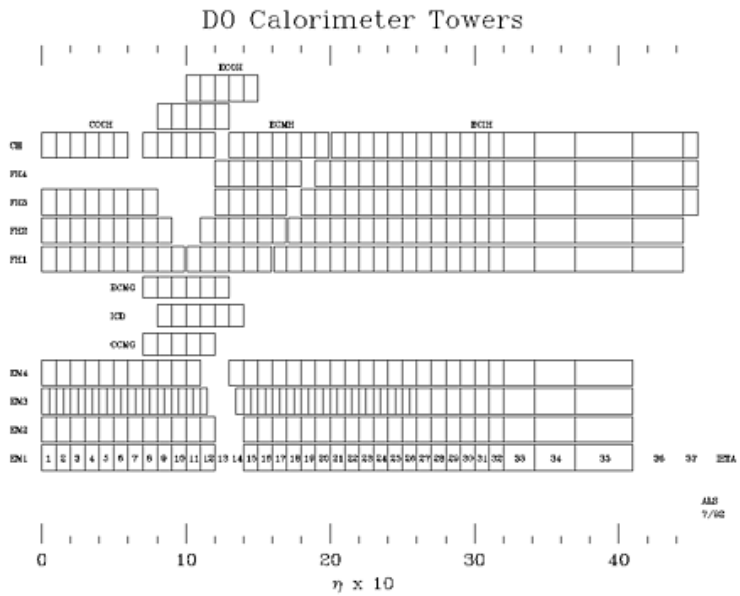

Figure 3.13. Calorimeter segmentation is shown for detector eta (η_d) and IETA.

segmentation of $\Delta\eta \times \Delta\phi = 0.1 \times 0.1$ out to IETA = 32 (or $\eta_d = 3.2$). The third EM calorimeter layer is an exception since it is segmented twice as finely to enable good measurement of EM showers. However, for large η the physical size of the detector slices becomes very small (see figure 3.11, and it is necessary to group cells into larger dimensions of $\eta - \phi$. This happens from IETA = 33 to 37. Table 3.1 shows how IETA is related to detector η.

Table 3.1. Conversion from η_d to IETA.

IETA	pseudorapidity (η_d)
33	3.20 - 3.42
34	3.42 - 3.70
35	3.70 - 4.10
36	4.10 - 4.45
37	4.45 - 5.20

3.4 Muon System

Although it is not used for this analysis, a brief description of the muon system was included for completeness. More detailed information about this detector can be found in [26] and [37].

The muon spectrometer is the outermost DØ detector, and is responsible for the identification of muons and the measurement of their momenta and trajectories. Muons have a long mean lifetime (2.2 μsec) compared to the scale of the detector, and they lose little energy even in dense absorbers. The radiation length for muons in a material scales by a factor of $(m_\mu/m_e)^2$ compared to that for electrons [28]. For example, in uranium X_{0e}=0.32 cm for electrons and $X_{0\mu}$=128 m for muons. The same scaling applies to the critical energy, above which electromagnetic showering occurs because energy loss by radiation dominates. The critical energy for electrons in uranium ≈6 MeV, meaning that it is likely that electrons produced in the $p\overline{p}$ collision will cause a shower. On the other hand, the critical energy for muons in uranium ≈250 GeV; therefore, muons produced are not likely to produce electromagnetic showers in the detector. Since they are not strongly interacting particles, muons do not produce hadronic showers either. As a result, muons at DØ do not shower in the calorimeter and are able to travel through the entire detector. This motivates the necessity of an additional detector outside of the calorimeter. The muon spectrometer is composed of proportional drift tube chambers (PDTs) located on either side of five separate solid iron toroidal magnets with a field strength of about 2 Tesla. These drift chambers are designed to detect muon tracks, and they function in much the same way as the VTX, CDC, and FDC detectors in the central tracking system. As muons pass through the magnetic field, their paths are bent. This change in direction is used to determine the muon momentum.

3.5 Triggering and Data Acquisition

The Tevatron operates with 6 bunches of protons and antiprotons which leaves a $3.5\mu sec$ window of time between crossings. At typical luminosities, almost every crossing leads to at least one collision; however, it is beyond current technological ability to record every event that occurs. At first glance, this would seem damaging to the physics capability of the experiment, but one must remember that most of these collisions are soft interactions. The process of selecting specific events deemed interesting enough to record is referred to as triggering. This filtering proceeds in four consecutive stages: the level 0, level 1, level 1.5, and level 2 triggers. Each trigger demands that events meet increasingly complex requirements in order to avoid rejection. Events that pass all four filters are saved. Eventually, off-line filters, defined by the physics analysis involved, are used to further select events which fit a specific profile.

3.5.1 Level 0

The LevelØ trigger is a scintillator based hardware trigger designed primarily to indicate the presence of an inelastic $p\overline{p}$ collision. The output rate from this initial filter is approximately 150 kHz. Each Level 0 detector consists of two layers of scintillation counters mounted on the front of the end calorimeter cryostats ($\pm 140cm$) around the beam pipe. These provide partial coverage in ϕ for $1.9 < |\eta| < 4.3$ and nearly full coverage for $2.3 < |\eta| < 3.9$. Each layer contains 20 short scintillator tiles (7x7 cm^2) and 8 long tiles (7x65 cm^2) (see Fig. 3.14). A coincidence between these two forward detectors signifies the breakup of the proton and antiproton. In addition to its main function, the Level 0 system monitors luminosity, identifies multiple interactions, and provides z-coordinate information on the event vertex. The latter is determined using the difference in arrival time for particles at the north and south

detectors. Finally, the Level 0 detector provides valuable information for diffractive analyses.

In this analysis, we are interested in identifying W and Z boson events with low particle multiplicities in part of the detector, specifically we look for forward rapidity gaps. Unfortunately, the presence of the standard LevelØ trigger requirement eliminates the possibility of recording events with a forward rapidity gap. However, this strict LevelØ coincidence requirement was modified during the RunI data collection. The LevelØ information was still recorded for use offline, but is was not explicitly part of the trigger. This enabled rapidity gap events, like the one shown in figure 3.14, to pass the trigger. In fact this detector plays an integral role in the search for diffractive W and Z events. Population of hits in the short Level 0 tiles are used along with the forward calorimeter to measure particle multiplicity distributions and define rapidity gaps.

3.5.2 Level 1 and Level 1.5

The Level 1 trigger is a hardware trigger involving the calorimeter and muon system that operates within the 3.5 μsec window between Tevatron bunch crossings. This trigger reduces the 150 kHz input rate from Level 0 to about 200 Hz.

Calorimeter cells are grouped in trigger towers of $\Delta\eta \times \Delta\phi = 0.2 \times 0.2$, and event variables like EM transverse energy (E_T), hadronic E_T, total E_T, and missing E_T are roughly calculated. Comparisons of these calculations to predetermined reference values will determine whether or not an event passes Level 1. A similar evaluation can also be done using individual calorimeter tower E_T information or muon chamber hit data. If an event satisfies Level 1 criteria, then it is passed either to Level 1.5 for further evaluation or directly to the Level 2 trigger.

The Level 1.5 trigger is a slower hardware trigger that requires more processing time than provided by the bunch crossing interval. Higher level transverse energy

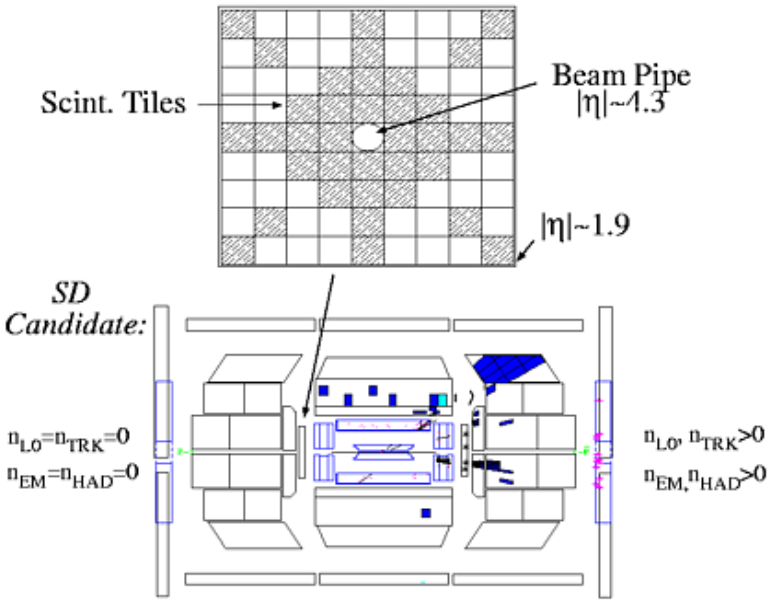

Figure 3.14. The LevelØ detector is made up of scintillating tiles (shaded squares). The two detectors are mounted around the beam pipe on the front of each end calorimeter cryostat. The LevelØ system is most often used to identify inelastic $p\overline{p}$ collisions, but for diffractive analyses it provides a mechanism to identify rapidity gaps. Here, a hard single diffractive candidate event is shown with activity only on one side of the detector and a gap on the other side.

calculations and muon track reconstructions are done and reduce the rate of successful triggers to under 100 Hz. For more information on the Level 1 and 1.5 triggers see [38], [39], [40], and [41].

3.5.3 Level 2

The Level 2 trigger is a software filter which uses information from the entire DØ detector to determine whether or not to permanently save an event. A farm of processors works in parallel using sophisticated algorithms to reconstruct physics objects and identify event characteristics. There are software tools designed to identify jet, muon, and electron candidates and their associated characteristics. Other tools exist to calculate $\not\!\!E_T$ and to determine noise or background conditions. Different types of interesting events have distinct physics object and event characteristic requirements. For example, this analysis requires an electron and $\not\!\!E_T$. Filters based on predetermined indicators make the final event selection which reduces the rate to 2 Hz. Events that pass this final trigger are saved permanently for use in off-line analyses. A detailed explanation of the triggers used to select the data for this analysis can be found in Chapter 4.

CHAPTER 4

DIFFRACTIVE W and Z BOSON ANALYSIS

For this analysis, we use a sample of $W \to e\nu$ events to measure the number of W events with forward rapidity gaps. (Note that the symbol, W, is used to represent both W^+ and W^-.) Only events in which the W decayed to an electron and an electron neutrino are considered. Since DØ had no magnetic field within the central tracking volume, electrons and positrons cannot be differentiated and both are referred to as electrons. We infer the presence of the neutrino from the large $\not{E}_T$ in the event. With this sample, we can measure the ratio of diffractive W bosons to all W bosons and compare it to Monte Carlo expectations. Similarly, a sample of $Z \to ee$ events was used to measure the rate of diffractive Z production.

Extraction of the diffractive W and Z boson production rate is a fairly complex process beginning with the selection of the appropriate data sample. Once we have the W and Z data samples, a method must be developed to identify diffractive events within these samples. There are two ways to accomplish this identification: either the outgoing proton or antiproton can be detected, or events with a rapidity gap can be tagged as diffractive. We do not yet have the capability to detect the outgoing proton (or antiproton). Therefore, we make use of the distinct topology of diffractive events by looking for W and Z events with a rapidity gap. We examine particle multiplicity distributions in the forward calorimeter and the LevelØ detectors to search for events with very low multiplicities (rapidity gaps) on one side of the detector. Once these events have been identified, a procedure is needed to determine

the quantitative diffractive W and Z production rate (in other words, the ratio: diffractive W/all W). This signal extraction is accomplished by simultaneously fitting the inclusive (diffractive and non-diffractive) multiplicity distributions, and is described in detail in the following sections. When the diffractive signals in data have been firmly established, comparisons to Monte Carlo predictions can be made. Such comparisons for several models of the pomeron are made in Chapter 5.

4.1 Data Selection

Candidate $W \to e\nu$ events are identified by the presence of an isolated, high p_T electron and a high p_T neutrino. Similarly, candidate $Z \to ee$ events are identified by the presence of two isolated high p_T electrons. The event selection process occurs in two steps. First, a set of trigger requirements is imposed upon all events at DØ . These vary depending on the target physics involved. For example, different triggers exist that are designed to select events which are likely to involve the top quark, the b quark, QCD mechanisms, or the W and Z bosons. Events which pass the W and Z triggers are written to tape for subsequent analysis. Further requirements are then made offline to maximize the desired data sample while minimizing any background contamination.

4.1.1 Trigger Discussion

The W data were obtained with the high transverse momentum electron trigger EM1 EISTRKCC MS at a center-of-mass energy of 1800 GeV. At Level 1, the signal trigger (EM_1_HIGH) required one or more electromagnetic calorimeter towers with $E_T \geq 10$ GeV. A Level 1.5 trigger tool was also used that required an electromagnetic object with $E_T > 15$ GeV and electromagnetic (EM) fraction $\geq 85\%$, where the EM fraction was the ratio of the EM E_T to the total E_T in the towers. At Level 2, the EM1 EISTRKCC MS filter selected events having one EM object with $E_T > 20$ GeV

that satisfied shower shape cuts (based on test beam electron shower shapes), and was isolated from other objects in the calorimeter. This isolation requirement was calculated with a 0.4 radius cone, in η-ϕ space, which is roughly equivalent to an isolation selection of $f_{iso} < 0.15$ cut offline (see Section 4.1.4 for more information on f_{iso}.). A cut of $\not\!\!E_T > 15$ GeV was also required for the central (CC) and end (EC) calorimeters. Similarly, the Z data were obtained with the EM1 EISTRKCC ESC filter, which had the same requirements at Level 1 and Level 1.5. At Level 2, there was an addeditional demand for two electromagnetic objects with $E_T > 16$ GeV.

4.1.2 Offline Cuts

After events have passed the trigger selection cuts, further processing geared specifically for each analysis is done offline. For this analysis, we need to select single interaction W and Z events (see Section 4.1.3) with good electrons (see Section 4.1.4) and no LevelØ coincidence requirement. Before run number 85277, a LevelØ coincidence was required as part of the trigger. This indicated that an inelastic interaction involving both LevelØ detectors had occurred. Such a requirement would eliminate observable diffractive W and Z events (those with a rapidity gap) from the sample (see Section 3.5.1). Thus for this analysis, we only use the samples of $W \to e\nu$ and $Z \to ee$ events taken after run number 85277, where there was no such restriction. Note: a search for diffractive W production in the muon channel is not possible due to the small statistics. Additionally, the LevelØ coincidence is needed to reduce the background in muon samples.

When selecting candidate events, attention must also be given to the Main Ring, a 150 GeV proton synchrotron that is part of the Fermilab accelerator system. This accelerator is housed in the same tunnel as the Tevatron; in fact, at DØ the Main Ring beam pipe passes through the the outer section of the calorimeter. As a result

of this inconvenient layout, proton bunches passing through the area can deposit significant amounts of energy in the calorimeter. This produces backgrounds in the detector that are eliminated using timing cuts based on the accelerator clock signal [42]. Events within a 1.6 μsec window (the MICRO BLANK window) around these time periods are rejected offline. Large beam losses also occur when beam is being injected into the Main Ring, so events occurring within a 400 msec window (the MRBS LOSS window) are also rejected.

Further requirements were then made on the electron E_T, the $\not\!\!E_T$, and the quality of the electron object in each event. Candidate events for this analysis were selected with the criteria listed in Table 4.1 for central and forward electron W's. Similarly, a search was done for diffractively produced Z bosons using the criteria listed in Table 4.2. First, runs with known problems [43] were removed. Then multiple interaction events (see Section 4.1.3) were cut from the sample. Selection criteria based on the 'electron-ness' of the EM objects were also imposed upon the events (see Section 4.1.4). Standard techniques have been developed to identify electrons while significantly reducing the background [44] [45]. These criteria rely on calorimeter and tracking information. There are four such discriminating variables: the shower isolation fraction (f_{iso}), the electromagnetic fraction (EMf), the track match significance (σ_{track}), and the H-matrix chi-squared (χ^2). The EMf and χ^2 variables make use of the differences between hadronic and electromagnetic showering in the calorimeter. f_{iso} is a topological cut that preferentially selects electrons from the decay of a W or Z boson as opposed to those from heavy quark leptonic decays. The track match significance is used to reject photons which are often produced through the process: $\pi^0 \rightarrow \gamma\gamma$. Candidate W events were required to have one 'tight' electron (see Table 4.1), while candidate Z events required two 'loose' electrons where at least one was also 'tight'. These electron classifications were

based both on detector region and object characteristics. In order to increase statistics, the Z analysis used the combination of CC-CC, and CC-EC electron events, removing those with both electrons in the EC due to difficulty in electron identification in this region of the detector. The event selection tables include cuts on multiple interactions and electron quality variables which are discussed in following sections.

4.1.3 Multiple Interaction Cuts

The effect of multiple interactions must be carefully considered in the search for diffractive W and Z signals using rapidity gaps. The presence of a second $p\overline{p}$ inelastic collision in a diffractive W or Z event will typically spoil any rapidity gap. Therefore, we require a loose veto on multiple interactions. An MIflag value of zero indicates that there was not sufficient LevelØ information to calculate the flag (hits on both sides are required to claim a non-zero flag value). A value of 1 designates that the event likely contained a single interaction. This is determined by using the width of the time distribution of hits in the LØ detector, where multiple interaction event distributions have a larger width. Furthermore, the value of MIrun1 was required to be less than 3. This additional condition using the MIrun1 tool demands that vertex and energy information from the event be consistent with a single interaction.

A secondary interaction will also typically shift the particle multiplicities in events to higher values. The final data sample in a search for rapidity gap events should be composed of single interaction events since any multiple interaction event contamination of the sample would artificially lower the fraction of diffractive events. Therefore, we must understand the data sample composition and calculate a correction to the fraction due to residual multiple interaction contamination (see Section 4.2.3). It is also possible to misidentify single interaction events as multiple interaction events, thereby incorrectly removing them from the sample. The

Table 4.1. Central and Forward W electron event selection criteria. The event selection process removes events from the event sample based on all of the quality characteristics for each electron rather than making cuts on each quality individually. The bold face numbers indicate how the sample size decreases with each cut. The non-bold numbers simply show how many events have electrons with the corresponding electron characteristic.

Variable		**N Events**
filter	EM1_EISTRKCC_MS	**119,890**
run number	> 85277	**84,310**
exclude bad runs		**83,602**
MICRO_BLANK and MRBS_LOSS veto		**63,978**
Mult Int	(MI)flag < 2	**22,945**
	(if MI flag $\neq 0$; mirun1 < 3)	**17,870**
Loose Electron		
electron E_T	$E_T > 25$ GeV	**15,402**
Fiducial cuts: EM cluster in well-measured region		
Central Calorimeter or Endcap Calorimeter	$\lvert\eta_{det}\rvert < 1.1$ $1.5 < \lvert\eta_{det}\rvert < 2.5$	17,626
position in ϕ	$0.05 < e\ \Delta\phi_{crack} < 0.95$	17,228
Quality cuts: identify 'electron-ness' of object		
e isolation	$f_{iso} \leq 0.1$	17,806
e EM fraction	EM$f \geq 0.95$	17,435
shower shape	H-matrix $\chi^2 < 100.0$	17,201
Tight Electron: **Loose Electron** *plus ....*		**13,770**
track match CC track match EC	$\sigma \leq 5.0$ $\sigma \leq 10.0$	17,133
$\not\!\!E_T$	$\not\!\!E_T > 25$ GeV	**12,653**
Reject if $Electron_2$ **Loose**		**12,622**
Total e W **sample**		**12,622**
Final Central e sample	$\lvert\eta_{det}\rvert < 1.1$	**8,742**
Final Forward e sample	$1.5 < \lvert\eta_{det}\rvert < 2.5$	**3,898**

Table 4.2. Central and Forward Z electron event selection criteria. All selection cuts were applied to each electron for events with CC-CC, CC-EC, and EC-EC electrons. The event selection process removes events from the event sample based on all of the quality characteristics for each electron rather than making cuts on each quality individually. The bold face numbers indicate how the sample size decreases with each cut. The non-bold numbers simply show how many events have electrons with the corresponding electron characteristic. Events containing EC-EC events were removed from the sample as a final cut.

Variable		**N Events**
filter	EM1_EISTRKCC_ESC	**13,912**
run number	> 85277	**10,023**
remove bad runs		**9,994**
MICRO_BLANK and MRBS_LOSS veto		**8,751**
Multiple Interaction	(MI)flag < 2	**3,059**
	(if MI flag $\neq 0$; mirun1 < 3)	**2,381**
electron$_2$ E_T	$E_T > 25$ GeV	**1,149**
Loose Electron		N Events
Fiducial cuts: EM cluster in well-measured region		
Central Calorimeter or Endcap Calorimeter	$\lvert\eta_{det}\rvert < 1.1$ $1.5 < \lvert\eta_{det}\rvert < 2.5$	1,718
position in ϕ	$0.05 < e\ \Delta\phi_{crack} < 0.95$	1,680 (for e_1)
Quality cuts: identify 'electron-ness' of object		
e isolation	$f_{iso} \leq 0.1$	1,810 (for e_1)
e EM fraction	EM$f \geq 0.95$	1,748 (for e_1)
shower shape	H-matrix $\chi^2 < 100.0$	1,723 (for e_1)
Tight Electron: Loose Electron *plus ....*		
track match CC	$\sigma \leq 5.0$	1,552 (for e_1)
track match EC	$\sigma \leq 10.0$	
Require 1 Tight and 1 Loose e		**893**
Invariant Mass	$75.0 < M_{ee} < 105$ GeV	**801**
Total e Z **sample**		**801**
Final Z **sample**	CC-CC or CC-EC	**715**

concern is that possible diffractive events may be mistakenly overlooked. However, these single interaction events must mimic the characteristics of MI events in order to be misidentified. This implies that they are likely to be high multiplicity events rather than rapidity gap events. As a result, the loss of such events can be offset by multiple interaction events misidentified as single interactions. No correction is applied for lost single interaction events.

4.1.4 Electron Quality Cuts

Electron quality characteristics (see Tables 4.1 and 4.2) were used to separate electron objects from non-W background objects like photons and pions (the QCD background from pions that mimic electrons dominates). These quality cuts were also effective at rejecting cosmic ray events which are a source of background, particularly in triggers requiring calorimeter activity with no beam interaction tag (coincidence in LØ scintillator). 'Tight' electron requirements used to determine the standard data sample were later relaxed to the 'loose' criteria in order to increase sample statistics in an attempt to stabilize the background shape used for fitting. The Z electron quality cuts were applied to each electron individually, independent of the detector location of the accompanying electron in the event.

The relevant electron quality characteristics include the shower isolation in the calorimeter, the EM fraction of the object, the track match significance, and the shower shape. First, the shower must be isolated from other objects in the calorimeter. The isolation is quantified by comparing the energy in the center of the shower to that in the rest of the shower as follows:

$$f_{iso} = \frac{E^{total}_{\Delta R=0.4} - E^{EM}_{\Delta R=0.2}}{E^{EM}_{\Delta R=0.2}}$$

In the above equation, ΔR indicates the radius of a cone in η-ϕ space, around the center of the shower [42]. The EM fraction, EMf, is defined as:

$$EMf = \frac{E_{EM1} + E_{EM2} + E_{EM3} + E_{EM4}}{E_{EM1} + E_{EM2} + E_{EM3} + E_{EM4} + E_{FH1}}$$

where E_{EM1} is the energy in the first layer of the EM calorimeter, etc. This quantity, EMf, determines what fraction of the cluster energy is contained within the EM calorimeter. To distinguish between electrons (which are expected to have tracks) and photons (which are not), a quantity called the track match significance σ_{track} is used. This indicates the degree to which the calorimeter cluster and nearest track correspond and is defined to be:

$$\sigma_{track} = \sqrt{\frac{(\rho\Delta\phi)^2}{\delta_{\rho\phi}^2} + \frac{\Delta z^2}{\delta_z^2}} \quad and \quad \sigma_{track} = \sqrt{\frac{(\rho\Delta\phi)^2}{\delta_{\rho\phi}^2} + \frac{\Delta\rho^2}{\delta_\rho^2}}$$

for CC and EC electrons, respectively, with

$$\Delta\phi = \phi_{track} - \phi_{cluster} \quad and \quad \Delta z = z_{track} - z_{cluster}.$$

Here, $\rho\Delta\phi$, Δz, and $\Delta\rho$ are the distances in the azimuthal direction, the z direction, and the radial direction respectively. The corresponding position resolutions of the calorimeter are given by $\delta_{\rho\phi}$, δ_z, and δ_ρ [46]. In the CC, the longitudinal and transverse resolutions are $\delta_z = 1.7$ cm and $\delta_{\rho\phi} = 0.3$ cm, respectively. In the EC, the corresponding resolutions are: $\delta_\rho = 0.7$ cm and $\delta_{\rho\phi} = 0.3$ cm [46].

The electromagnetic shower shape quality was quantified in the form of a 41x41 covariance H-matrix determined from test beam data and Monte Carlo calorimeter response simulations. Some observables used to form the matrix include the fraction of the shower energy in layers 1, 2 and 4 of the EM calorimeter, the logarithm of the shower energy, and the position of the event vertex along the beam. The inverse

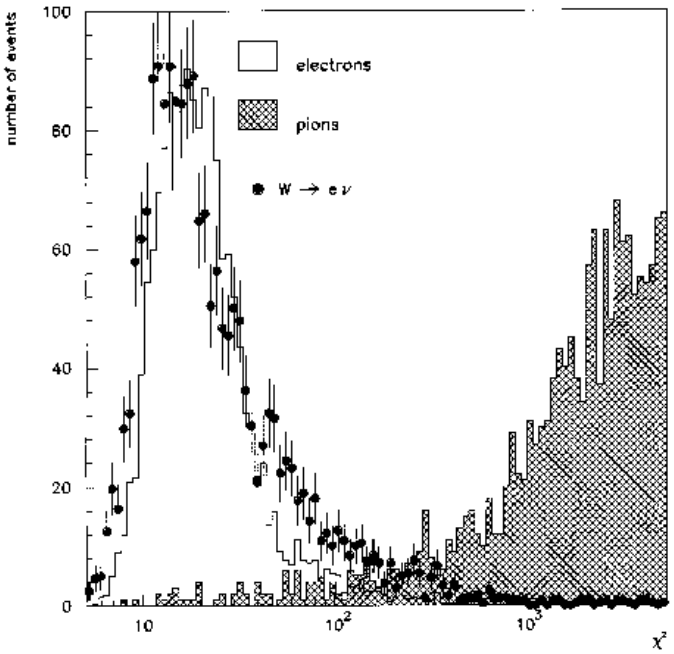

Figure 4.1. H-matrix χ^2 distribution for test beam pions (shaded), test beam electrons (unshaded), and electrons from an early $W \rightarrow e\nu$ sample (data points) [45]. Only true electrons have low χ^2 values, which enables us to efficiently remove the pion background events.

of the matrix was used in the calculation of a chi-squared, χ^2 [47]. This parameter is used to remove pions from the sample of candidate electrons. Figure 4.1 shows the strong pion background rejection power of this variable. Finally, a fiducial cut on electron ϕ was imposed to ensure that the candidates are away from cracks between calorimeter modules where they would not be well measured. After all cuts were applied, the final data samples contained 8,724 central electron W events, 3,898 forward electron W events, and 715 Z events (CC-CC, CC-EC electrons) (see Tables 4.1 and 4.2.) These final samples make up approximately 18% of the total Run1b W and Z data sample. The specific requirements necessary for this analysis, in particular those relating to the LevelØ trigger and multiple interactions, significanlty reduce the sample size.

4.2 Signal Measurement

In order to study hard diffraction, we make use of the distinct topology involved by looking at particle multiplicity. If we plot the number of particles in a certain region of the detector, for color singlet exchange (diffractive events) a rapidity gap is expected. There are no particles in the detector, and this leads to a spike at 0 multiplicity (see Fig. 4.2). On the other hand, for color exchange there is a broad multiplicity peak which tapers off to zero on both sides (see Fig. 4.2). The color exchange multiplicity will also have a very high mean multiplicity ($\sim$ 70 towers) compared to that of the color singlet distribution ($\sim$ 1 tower). These distinct particle multiplicity distributions enable discrimination between diffractive and non-diffractive events when they are combined into an inclusive sample.

We simultaneously examine particle multiplicity distributions in the forward calorimeter and the corresponding LevelØ detector to search for events with very low multiplicities (rapidity gaps) on one side of the detector. This is the signature of diffractively produced Ws and Zs. Figure 4.3 shows the event displays for a

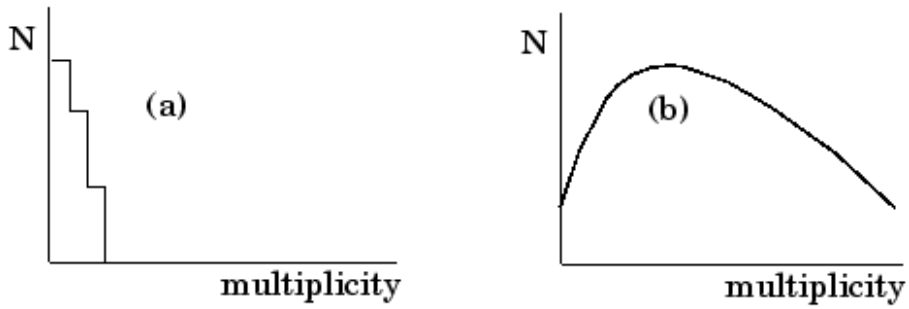

Figure 4.2. The particle multiplicity distributions expected for a) color singlet exchange, and b) color exchange.

typical QCD event and a diffractive W-boson candidate event. The QCD event shows two jets in the calorimeter, beam remnants on both sides from the breakup of the proton and antiproton, and particles scattered throughout the detector. On the other hand, the diffractive W event display shows the electron in the calorimeter with beam remnants on only one side of the detector, and nothing on the other side. This empty region is the rapidity gap used to tag diffractive events, and is easily identified. In this manner, we identify diffractive W and Z events and eventually determine the ratio of diffractive W events to all W events. The same measurement is also made using diffractive Z events. These ratios will then be compared to diffractive W and Z fractions predicted using a Monte Carlo based on the Ingelman and Schlein model of diffraction. (See Section 2.5 for a description of the Ingelman and Schlein model, and Chapter 5 for a description of the Monte Carlo.)

4.2.1 Calorimeter Threshold Selection

In the search for diffractive W and Z events, we measure forward calorimeter tower multiplicities above an energy threshold in the range $3.0 \leq |\eta| \leq 5.2$. A detailed study using a zero-bias data run (which required only a beam crossing) was done to

DØ Event Displays in η– ϕ

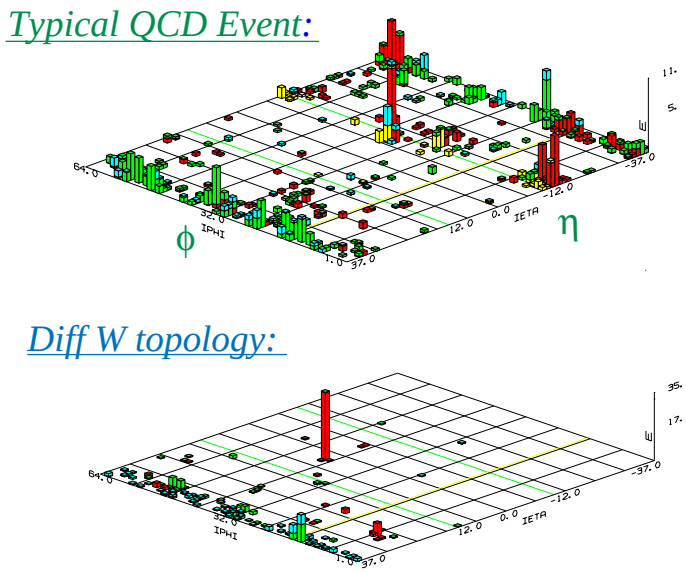

Figure 4.3. Event displays are shown for a typical QCD event and a diffractive W boson candidate event. If the calorimeter is sliced and then unrolled, we get pictures of the detector like those shown here. Each event display shows the amount of energy deposited in the calorimeter, and where these energy deposits were located in ϕ and η. In the QCD event, two jets (localized bunches of energy) can be seen with particles scattered throughout the detector. The diffractive W candidate event has an electron and $\not{E}_T$, with a beam remnant on one side of the detector, but nothing on the other side. This empty region at high η is the rapidity gap which identifies this as a diffractive W event.

determine the appropriate energy thresholds to maximize efficiency for identification of particles while minimizing sensitivity to noise which can ruin rapidity gaps [48]. Ideally this threshold would be just above the calorimeter noise level. This would provide the optimal separation between the diffractive signal and the color exchange background. If the threshold were too high, the background multiplicity distribution would shift lower and confuse the significance of a low multiplicity. Taken to the extreme, a high threshold would cause every event to have a multiplicity of zero. On the other hand, a threshold below calorimeter noise would push real diffractive event multiplicities too high, and rapidity gap events would register as non-zero multiplicity events due to the detector noise contributing to the multiplicity.

For this zero-bias analysis, the calorimeter was separated into three detectors: the EM calorimeter, the forward hadronic calorimeter (FHD), and the last layer of the forward hadronic calorimeter (IH15) which is treated independently because it is constructed of stainless steel instead of uranium. The IETA regions covered are (21 to 35) or $2.0 \leq |\eta| \leq 4.1$ for the EM calorimeter, and (IETA = 33 to 37) or $3.2 \leq |\eta| \leq 5.2$ for the FHD (see Section 3.3 for a discussion of IETA as it relates to η_d). Energy thresholds of 150 MeV for EM, 500 MeV for the FHD, and 50 MeV for the IH15 were chosen such that only 2.0%, 2.0%, and 0.2% of the zero multiplicity events respectively were spoiled by detector noise [48]. With these thresholds, the final algorithm used to identify rapidity gaps was insensitive to noise. A cross-check of this study was also done to ensure that most non-diffractive interaction events registered at least one tower above these thresholds [48]. This is necessary in order to prevent non-diffractive events from being tagged as rapidity gap events.

4.2.2 Diffractive Event Identification

Now that appropriate energy thresholds have been determined for the calorimeter, we can look at the particle multiplicity distributions for the W and Z data samples.

For diffractively produced jets, the rapidity gap is typically located opposite the leading jets [48]. However, for diffractively produced W bosons, the topology is such that the electron may or may not be in the same section of the detector as the W. This is because the massive W decays nearly isotropically with respect to the electron in the lab. As shown in Fig. 4.4, the rapidity gap is more likely to be opposite the electron; however, it is also possible for the gap and electron to be on the same side of the detector. To ensure consistent identification of rapidity gap events, the minimum and maximum multiplicity sides of the detector are determined for each event. The minimum multiplicity side of the detector is defined as the side with the lowest number of calorimeter towers hit. If both forward portions of the detector have the same number of towers hit, then the tie is broken using the LevelØ detector. Then the number of calorimeter towers above threshold (n_{CAL}) is measured on the minimum multiplicity side of the detector. For this analysis, the η range used in the search for a rapidity gap is called the 'far gap', and is defined to be $3.0 \leq |\eta| \leq 5.2$. In addition to the calorimeter multiplicity, that of the LevelØ detector on the minimum calorimeter multiplicity side is also measured. An excess of events at low multiplicity in the resulting two-dimensional multiplicity distribution indicates the presence of diffractively produced W or Z bosons.

This multiplicity distribution is shown in Fig. 4.5 for the central electron W sample, in Fig. 4.6 for the forward electron W sample, and in Fig. 4.7 for the Z sample. All distributions show a distinct peak at $n_{L\emptyset} = n_{CAL} = 0$, consistent with expectations for a diffractive signal component, and a broad large-mean multiplicity distribution associated with standard W or Z production.

4.2.3 Corrections and Uncertainties

Before we can extract a quantitative diffractive W or Z signal, we must investigate any potential stumbling blocks in the way. There are two potentially problematic

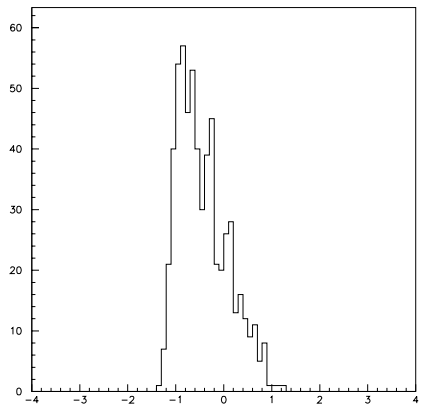

Figure 4.4. POMPYT [49] Monte Carlo electron η distribution (mean e η = -0.4335), for $n_{L\emptyset}$ = n_{CAL} =0 on the south side ($\eta > 0$) of the detector. The electron is more frequently found opposite the rapidity gap which is at positive η for this figure, but it is possible for the gap and electron to be on the same side of the detector.

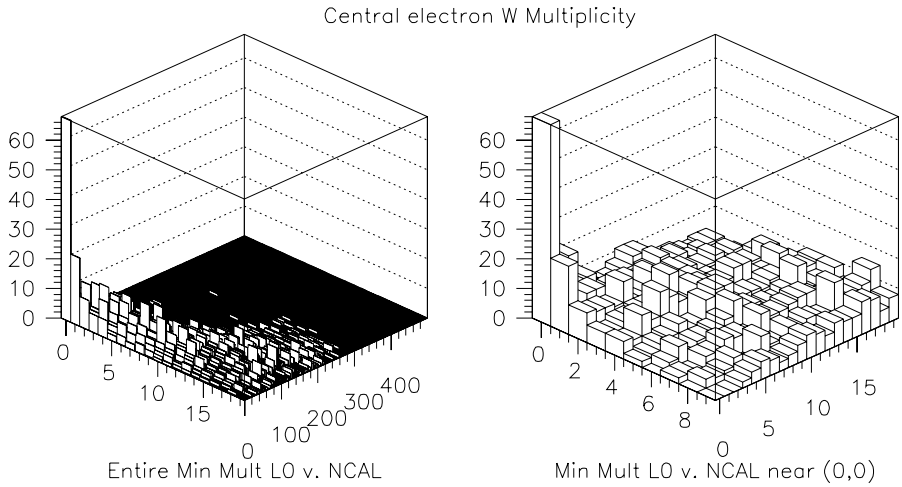

Figure 4.5. The multiplicity of LØ and calorimeter towers above threshold in the minimum multiplicity far gap region for the central electron W sample is shown. The right-hand plot is a close-up of the region near (0,0). The LØ axis runs from 0 to 20 for the plot on the left, and it runs from 0 to 10 on the close-up plot. The calorimeter tower axis runs from a multiplicity of 0 to 500 and 0 to 20 for the entire plot and the close-up, respectively.

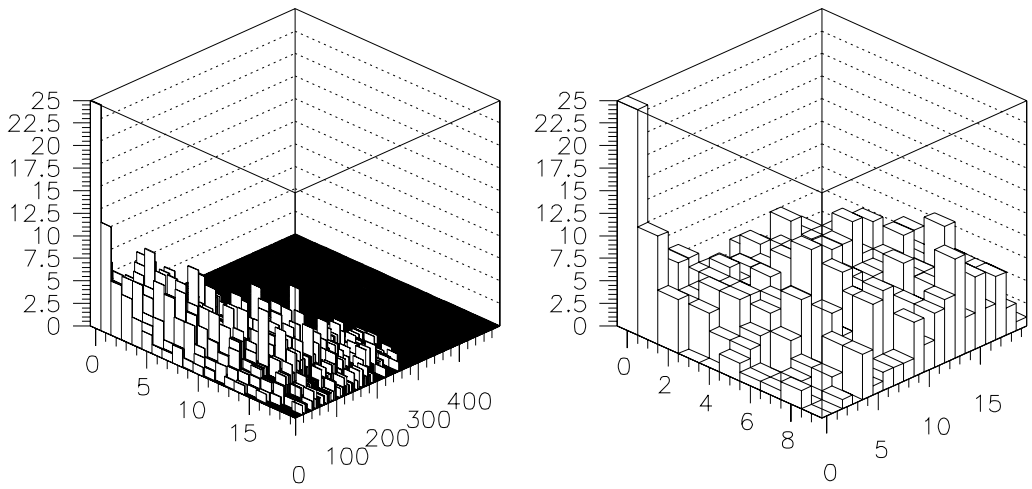

Figure 4.6. The multiplicity of LØ and calorimeter towers above threshold in the minimum multiplicity far gap region for the forward electron W sample. The right-hand plot is a close-up of the region near (0,0). The LØ axis runs from 0 to 20 for the plot on the left, and it runs from 0 to 10 on the close-up plot. The calorimeter tower axis runs from a multiplicity of 0 to 500 and 0 to 20 for the entire plot and the close-up, respectively.

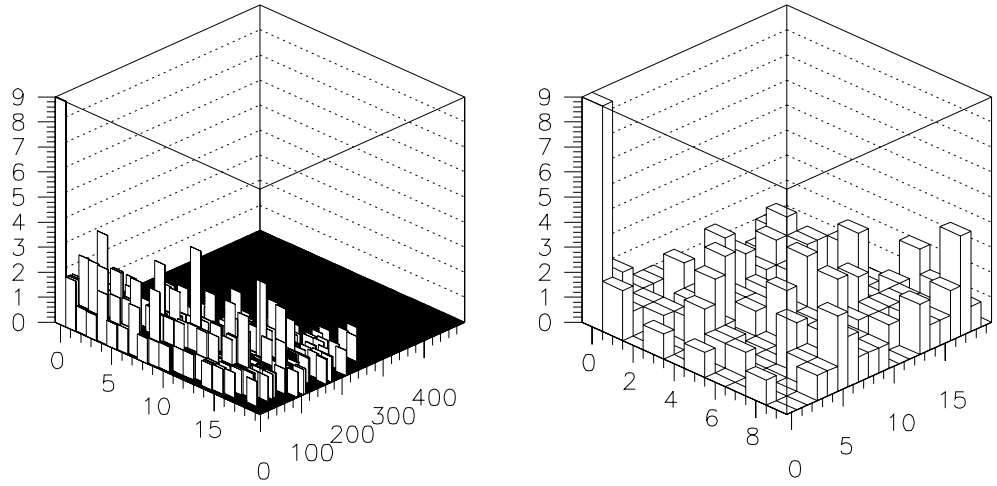

Figure 4.7. The multiplicity of LØ and calorimeter towers above threshold in the minimum multiplicity far gap region for the Z sample. The right-hand plot is a close-up of the region near (0,0). The LØ axis runs from 0 to 20 for the plot on the left, and it runs from 0 to 10 on the close-up plot. The calorimeter tower axis runs from a multiplicity of 0 to 500 and 0 to 20 for the entire plot and the close-up, respectively.

areas for this analysis that could cause a miscalculation of the diffractive W (Z) to all W (Z) fraction. The first is the possible presence of residual multiple interaction events in the final data sample, and the second is negative energy in the detector. The latter is the result of energy in the detector from a previous interaction which raises the calorimeter tower pedestal and lowers the amount of energy attributed to that part of the detector. Each of these potential problems must be examined and, if necessary, corrections applied to the diffractive W and Z data fractions.

The final data sample in any search for rapidity gap events is ideally composed of single interaction events. Any multiple interaction event would most likely not have a rapidity gap even if one interaction were diffractive, because the second event would spoil such a gap. Therefore, retaining multiple interaction events in the sample would artificially lower the fraction of diffractive events. On the other hand, negative energy in the calorimeter could falsely increase this fraction if it were to artificially create excess rapidity gap events. Detailed studies were done to determine the effects of these factors on the diffractive W and Z fractions.

Residual Contamination

A luminosity-dependent residual contamination correction to the fraction is developed by using standard cut data samples ($N = 8,724$ for the central electron W sample and $N = 3,898$ for the forward electron W sample) and samples without cuts on multiple interactions ($N = 27,884$, $N = 13,916$). In the NoCut sample, the MI cuts have been removed. To first order, all events beyond those in the standard sample should be multiple interaction (MI) events.

Estimation of the MI contamination is done by comparing the predicted number of single interactions as a function of luminosity to the standard cut sample distribution. Events in the standard sample should be predominantly single interactions (SI). The probability of a single interaction occurring as a function of luminosity

was calculated in steps of 0.5×10^{30} from a luminosity of 0.0×10^{30} to 20.0×10^{30}. Multiplying the NoCut W sample luminosity distribution by the single interaction probability gives us the expected number of SI events vs luminosity. This predicted distribution is compared to the standard data sample, to which MI cuts have been applied. Any excess is defined as the residual contamination. Figure 4.8 shows these luminosity distributions for the central W sample, Fig. 4.9 for the forward W sample, and Fig. 4.10 for the Z sample.

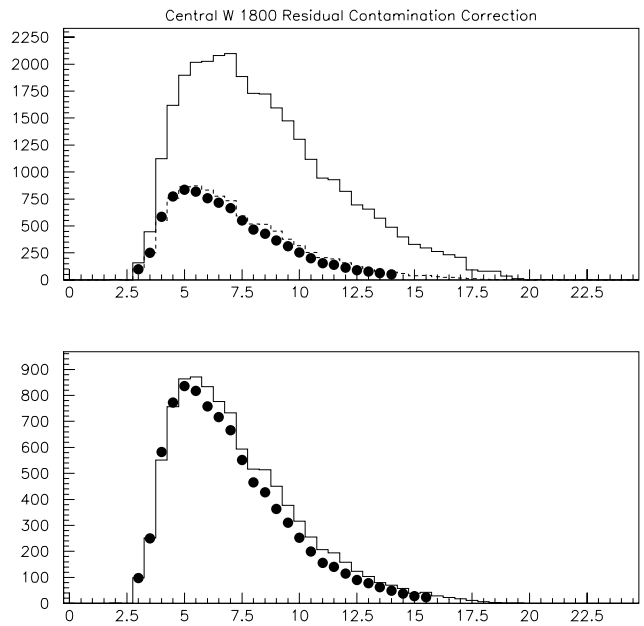

Figure 4.8. Residual contamination calculation for the central electron W sample. The top plot shows the NoCut sample luminosity distribution as a solid line with the standard data sample shown by the dashed line (nearly obscured by the solid points). (The y-axis is the number of events in each luminosity bin, where luminosity is given by the x-axis.) The solid circles represent the predicted number of single interactions for each luminosity bin. The bottom plot again shows the standard sample distribution (solid line) overlaid with the predicted number of single interactions (solid circles) as a function of luminosity.

The percent correction is calculated as (number residual contamination events/total number of events)$\times$100. There is a $9.2 \pm^{5.4}_{5.7}$ % correction due to residual contami-

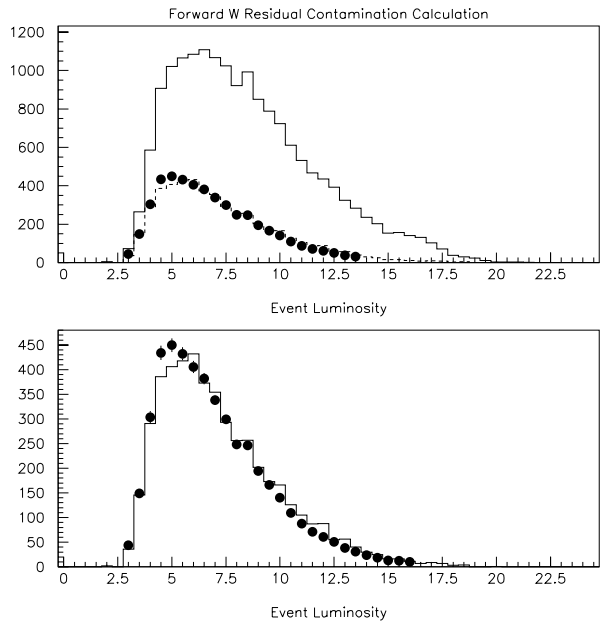

Figure 4.9. Residual contamination calculation for the forward electron W sample. The top plot shows the NoCut sample luminosity distribution as a solid line with the standard data sample shown by the dashed line (nearly obscured by the solid points). (The y-axis is the number of events in each luminosity bin, where luminosity is given by the x-axis.) The solid points represent the predictednumber of single interactions for each luminosity bin. The bottom plot again shows the standard sample distribution (solid line) overlaid with the calculated number of single interactions (solid circles) as a function of luminosity.

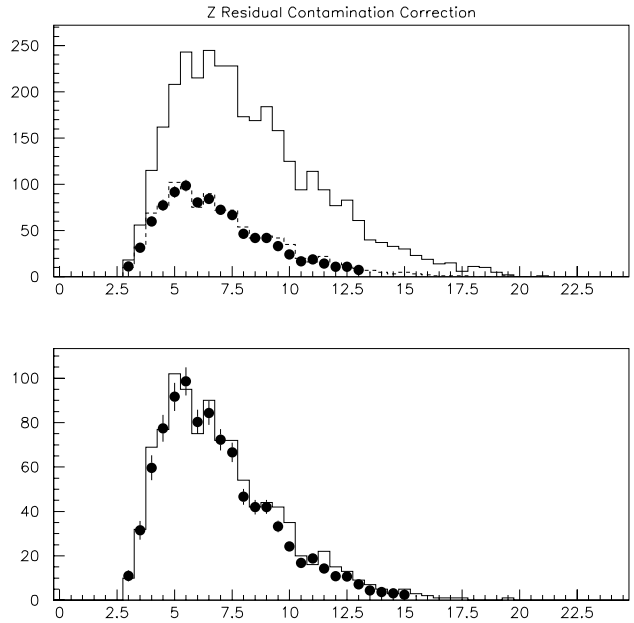

Figure 4.10. Residual contamination calculation for the Z sample. The top plot shows the NoCut sample luminosity distribution as a solid line with the standard data sample shown by the dashed line (nearly obscured by the solid points). (The y-axis is the number of events in each luminosity bin, where luminosity is given by the x-axis.) The solid points represent the predictednumber of single interactions for each luminosity bin. The bottom plot again shows the standard sample distribution (solid line) overlaid with the calculated number of single interactions (solid circles) as a function of luminosity.

nation on the central electron diffractive W fraction, a $0.0 \pm^{5.5}_{6.5}$ % correction on the forward electron W sample, and a $9.3 \pm^{5.2}_{5.7}$ % correction on the Z sample. These corrections are shown in Tables 4.3 and 4.4 for several data sets. The W event sample is divided into several sets which mimic those used to determine the diffractive W and Z fractions (see Section 4.3). The data sample is separated into low and high luminosity samples to determine whether or not there is a systematic luminosity dependence of the gap fraction. The sample is also split into several η regions to look for gap fraction dependence on rapidity. Samples with loose electron quality cuts or fewer restrictions on multiple interaction events have more events, and will be used in the quantitative diffractive fraction determination. (See Section 4.3 for a description of the quantitative signal extraction.) The multiple interaction contamination is determined for each of these samples as described above. To estimate the uncertainty in this method, the SI probability calculations were redone while adjusting the luminosity higher and lower by 5.3% for each point (5.3% was chosen because it is the rms uncertainty on the luminosity). The percent contamination in the forward W sample is lower than that of the central sample because the multiple interaction cuts are more efficient for this sample. As expected, the residual contamination increases dramatically for samples with less restrictive cuts on multiple interactions.

Negative Energy

Negative energy in the detector has the potential to influence the diffractive W fraction in the direction opposite that of MI contamination. Energy in the detector from a previous interaction raises the pedestal for the calorimeter towers involved which lowers the amount of energy attributed to that part of the calorimeter. This could push low multiplicity events into the zero bin which would falsely increase the number of events attributed to diffractive W bosons. The concern is that signal

Table 4.3. Residual contamination correction for several electron samples. The error was found by varying luminosity by 5.3% and recalculating the residual contamination.

Central e W Data Set	**Residual Contamination**
standard e cuts	$9.2\ \pm^{5.4}_{5.7}$ %
lum ≤ 7	$2.7\ \pm^{4.3}_{4.8}$ %
lum > 7	$17.0\ \pm^{6.6}_{7.1}$ %
$0.0 \leq \lvert\eta\rvert < 0.5$	$9.1\ \pm^{5.3}_{5.7}$ %
$0.5 \leq \lvert\eta\rvert < 1.1$	$9.7\ \pm^{5.3}_{5.8}$ %
loose e quality cuts	$8.3\ \pm^{5.4}_{5.8}$ %
E_T >30 $\not{E}_T$ > 30 GeV	$10.1\ \pm^{5.3}_{5.6}$ %
Emthresh 125MeV	$9.2\ \pm^{5.4}_{5.7}$ %
Emthresh 200MeV	$9.2\ \pm^{5.4}_{5.7}$ %
mirun1=1,2 no vtx cut	$23.6\ \pm^{4.5}_{4.8}$ %
flag=0,1 no vtx cut	$26.7\ \pm^{4.3}_{4.6}$ %
Forward e W Data Set	**Residual Contamination**
standard forward electron	$0.0\ \pm^{5.5}_{6.5}$ %
loose e quality cuts	$0.0\ \pm^{6.0}_{6.5}$ %
mirun1=1,2 no vtx cut	$17.1\ \pm^{4.9}_{5.2}$ %
flag=0,1 no vtx cut	$19.6\ \pm^{4.7}_{5.1}$ %
Central and Forward e W Data Set	**Residual Contamination**
standard cen+fwd e W sample	$6.0\ \pm^{5.5}_{6.0}$ %
Z Data Set	**Residual Contamination**
standard Z sample	$9.3\ \pm^{5.2}_{5.6}$ %

Table 4.4. Residual contamination correction for several combined central and forward electron samples. The error was found by varying luminosity by 5.3% and recalculating the residual contamination.

Central and Forward e W Data Set	**Residual Contamination**
standard cen+fwd e W sample	$6.0\ \pm^{5.5}_{6.0}$ %
EMthresh 125 MeV	$6.0\ \pm^{5.5}_{6.0}$ %
EMthresh 200 MeV	$6.0\ \pm^{5.5}_{6.0}$ %
loose e quality cuts	$5.3\ \pm^{5.6}_{6.0}$ %
lum ≤ 7	$0.0\ \pm^{4.5}_{4.5}$ %
lum > 7	$13.2\ \pm^{6.8}_{7.5}$ %
E_T >30 $\not{E}_T$ > 30 GeV	$7.5\ \pm^{5.5}_{5.8}$ %
mirun1=1,2 no vtx cut	$21.6\ \pm^{4.6}_{5.0}$ %
flag=0,1 no vtx cut	$24.5\ \pm^{4.4}_{4.8}$ %

events could be composed primarily of events with large amounts of negative energy compared to that of background events. To check this, the amount of negative energy per event was examined for both signal dominated and background (ie. standard color exchange W) dominated event samples. This was done by looking at events with a minimum side calorimeter multiplicity of $0-2$ and those with a minimum multiplicity of 3-5 respectively (see Figs 4.11 and 4.12).

For the central electron W sample, the signal dominated region had a mean negative energy of -21.76 GeV and the mean for the background region was -22.10 GeV. Note that there is no peak in the low multiplicity bin at large negative energy which would indicate fake gap events. In spite of this, it may still appear that negative energy could create a false signal by preferentially sliding events from low multiplicity bins into the zero bin. While this is partially true (events can be lowered in multiplicity), this effect is taken into account during the signal extraction. Consider the effect of changing the calorimeter tower energy threshold. A similar sliding of the multiplicity distribution into the zero bin occurs as the threshold is raised; however, the shape of the background dominated region does not change.

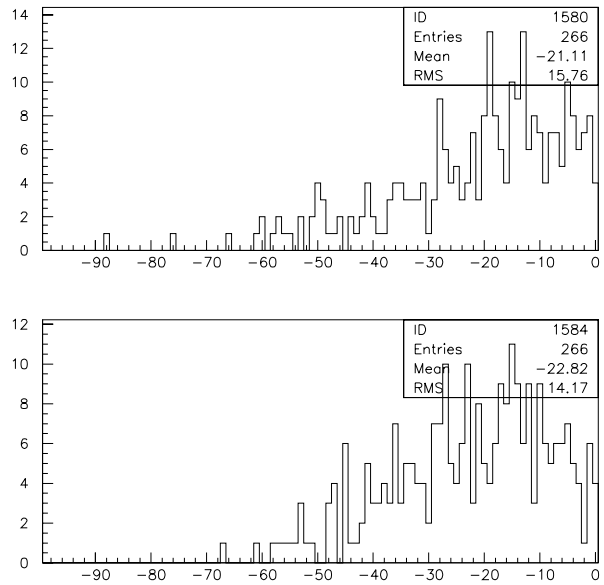

Figure 4.11. Central electron W events: Negative energy (x-axis) for signal dominated events compared to that for color exchange dominated events. The top plot shows the amount of negative energy in the EM calorimeter when the far gap on the minimum multiplicity side of the detector had a multiplicity of 0-2. The bottom plot shows the amount of negative energy in the EM calorimeter when the far gap has a multiplicity of 3-5. An event can only be in one or the other of these distributions, but not both. Therefore, these are mutually exclusive bins.

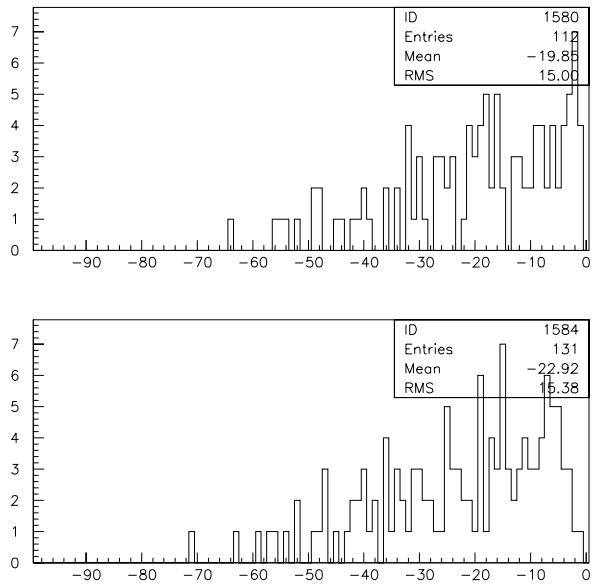

Figure 4.12. Forward electron W sample: Negative energy (x-axis) for signal dominated events compared to that for color exchange dominated events. The top plot shows the amount of negative energy in the EM calorimeter when the far gap on the minimum multiplicity side of the detector had a multiplicity of 0-2. The bottom plot shows the amount of negative energy in the EM calorimeter when the far gap has a multiplicity of 3-5. An event can only be in one or the other of these distributions, but not both. Therefore, these are mutually exclusive bins.

During the signal extraction using a fit to the background, the correct number of background events in the low(est) multiplicity bins will still be determined. Although the number of signal events in the lowest bin may change, the ratio of signal to background should remain the same. Since the amount of negative energy per event is consistent over the particle multiplicity range, any sliding toward low multiplicity bins should mimic the effect seen with increased thresholds. In other words, it too will be a smooth process and will not affect the ratio of signal to background events. The non-diffractive background shape (including that which extends to zero multiplicity) is determined during the quantitative signal extraction. This process accounts for the effect of negative energy when determining the diffractive W and Z signals. Therefore, the negative energy results for the central electron W sample do not indicate a problem, and no error has been assigned here.

Similarly, the negative energy in a signal-dominated sample and in a background-dominated sample were examined for the forward electrons. The mean negative energy in the EM calorimeter was -22.76 GeV for the signal region and -21.51 GeV in the background region. Again, this does not imply a problem, and no error has been assigned here.

4.3 Fitting

4.3.1 Quantitative Signal Extraction Procedure

We have successfully identified diffractive W and Z events within our data samples, and have also considered effects which might bias our results. We now extract the quantitative diffractive W and Z signals from the 2-D distributions of calorimeter tower and LevelØ multiplicities. This is accomplished by using a simultaneous fit of the signal (low multiplicity) and background regions applied to the $n_{L\emptyset}$ vs. n_{CAL} distribution for each W sample, Z sample, and several sub-samples. (See Appendix A for a more detailed description of the fitting method).

In addition to measuring the diffractive rate for the complete central electron W sample, we also divide it into luminosity bins or η bins for furthur study. These individual fits become components of the Range Fit method which is introduced in order to reduce any potential systematic error resulting from the specific choice of bins to include in the fit. In this method we perform many individual 2-D fits for each sample by systematically varying the range used in the fit. We then combine the knowledge gained from each fit to find the final gap fraction.

The Range Fit is applied in two distinct manners. First it is used for fits where both the signal and background are extracted from the same sample (Same Sample Background Fit). It is also applied to fits that use higher statistics samples to determine the shape of the non-diffractive background. This background shape is then applied during a subsequent fit of a low statistics sample to find the diffractive signal. This Alternate Background Sample method improves the error by enabling the fit routine to work with a more reliable background shape. This fitting method is necessary for low statistic samples. Previous analyses, like the study of hard single diffractive jet production, did not need this fitting iteration. The diffractive jet analysis was done using samples with very high statistics, and the range fit results were extremely stable. However, fits to the smaller statistics W and Z samples can change depending on the fit area because of statistical fluctuations in the background shape. As a result, the diffractive W and Z signal must be determined using a background shape found with a higher statistic sample. In fact, the diffractive Z signal can *only* be determined in this manner. All final diffractive W and Z fractions in data will be found using this Alternate Background Sample method. After the diffractive signal fraction is found, it must be corrected to account for contamination of the data sample by residual multiple interaction events. The appropriate correction factors can be found in Tables 4.3 and 4.4.

4.3.2 Range Fit Method

The quantitative diffractive W signal is extracted from the 2-D calorimeter vs. LevelØ multiplicity distributions by doing a two dimensional simultaneous fit of the signal and background which was initially developed for the hard single diffractive and double gap analyses [48]. The signal is fit by a falling exponential in both calorimeter and LØ multiplicities, and the background by a four parameter surface.

Performing the fit, a region around the peak at $(0,0)$ is masked off (2 bins in n_{L0} and 3 bins in n_{CAL}) and a first pass fit of only the non-diffractive background is done. These initial lower limits are chosen such that the signal region is excluded from the fit while the upper limits ensure that the very high multiplicity regions do not influence the background shape. For the calorimeter, this means that the upper limit, which ranges from n_{CAL}=6 to 12, is near but not beyond the color exchange peak around $n_{CAL} = 12$ (see Figure 4.13). This enables us to use as much multiplicity information relevant to the fit as possible without overly complicating the background shape by including the extremely high multiplicity region. The LØ limit, which ranges from 5 - 7, was chosen to be before the LØ multiplicity peak (see Figure 4.13). Once the initial background fit is completed, all of the parameters are relaxed. The signal parameters that were previously fixed and not included in the fit are allowed to vary, and both the background and signal distributions are simultaneously fit (see Figs 4.14 and 4.15).

The number of signal events, S_0, is given by the fit, and the fraction of diffractive W events above the color exchange background is calculated as S_0 divided by the total number of events in the sample. The error on the signal is determined from a MINOS error analysis, or is an estimate from the MINUIT parabolic error if the former is unavailable [48]. Included in the signal error are the statistical error and the systematic error on the fraction due to the fitting process.

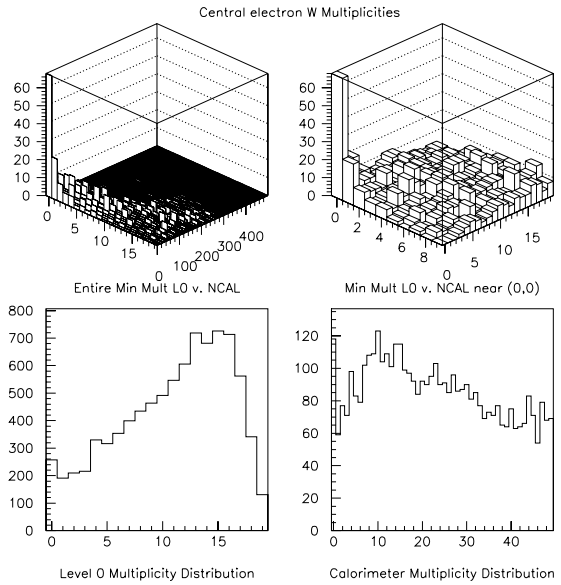

Figure 4.13. The multiplicity of LØ and calorimeter towers above threshold in the minimum multiplicity far gap region for the central electron W sample is shown (top left). The top-right plot is a close-up of the region near (0,0). The bottom left plot shows the LevelØ multiplicity distribution and the bottom right shows the calorimeter multiplicity distribution.

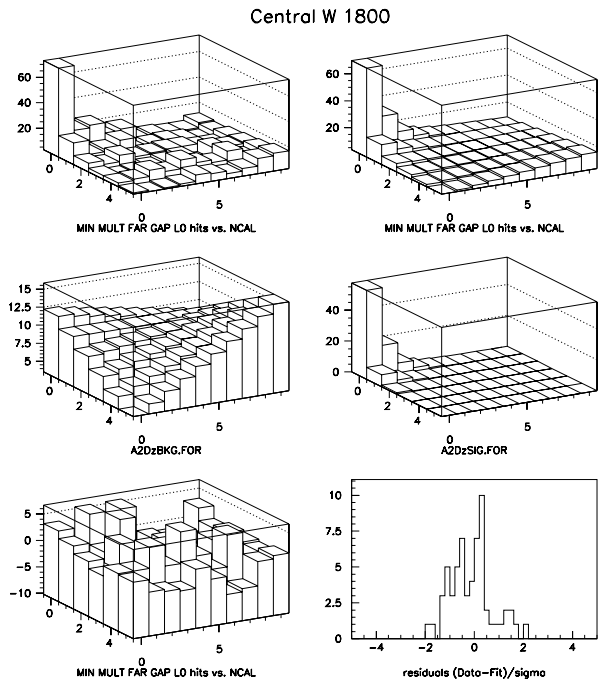

Figure 4.14. Two dimensional multiplicities (LØ vs calorimeter towers) from fitting routine are shown for a single fit for the central electron sample. The top left plot is the 2D $n_{L\emptyset}$ vs. n_{CAL} data distribution. The top right plot shows the 2D $n_{L\emptyset}$ vs. n_{CAL} distribution found using the fit where the signal fit result is added to the background background from the fit. The middle left plot shows the 2D background multiplicity distribution from the fit, and the middle right plot shows the signal multiplicity distribution from the fit. (Note: these two middle plots combine to produce the top right distribution.) The bottom left shows the data - fit distribution, and the bottom right shows the residuals for this single fit. No additional samples were used as background for this case.

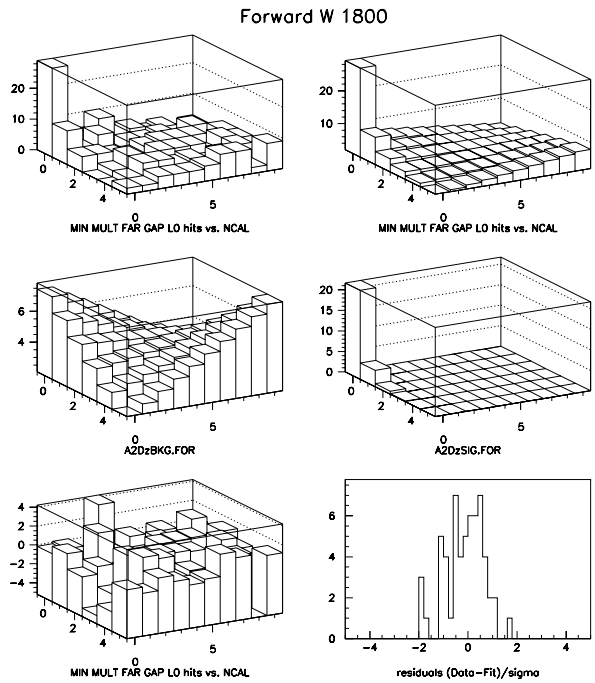

Figure 4.15. Two dimensional multiplicities (LØ vs calorimeter towers) from fitting routine are shown for a single fit for the central electron sample. The top left plot is the 2D $n_{L\emptyset}$ vs. n_{CAL} data distribution. The top right plot shows the 2D $n_{L\emptyset}$ vs. n_{CAL} distribution found using the fit where the signal fit result is added to the background background from the fit. The middle left plot shows the 2D background multiplicity distribution from the fit, and the middle right plot shows the signal multiplicity distribution from the fit. (Note: these two middle plots combine to produce the top right distribution.) The bottom left shows the data - fit distribution, and the bottom right shows the residuals for this single fit. No additional samples were used as background for this case.

Range Fit: Same Sample Background Fit Method

Taking a step beyond the solitary fitting method, a series of fits are performed for each sample. This ensures that there is no signal dependence on the range of bins used in the background fit. For this series of fits, the $n_{L\emptyset}$ and n_{CAL} fit limits are systematically varied. First, a 2D fit is performed with the LevelØ upper limit set to 5 and the upper limit in calorimeter towers set to 6. Then the calorimeter tower upper limit used in the fit is increased from 6 to 12, and a fit is performed for each different n_{cal} upper limit. Then the process is repeated for a LevelØ upper limit set to 6 and 7. The individual fits are done a total of 21 times for this specific case. We then have a distribution of the gap fractions from these 21 fits.

Figures 4.16 and 4.17 show such distributions for the central and forward electron W's respectively. The final gap fraction from the fit for each sample is defined to be the weighted mean of this distribution, where fits with smaller errors are given higher weight in calculating the mean. Additionally, only fits with at least one MINOS error are included in the calculation. The RMS scatter of these signals gives an error on the mean gap fraction. Additionally, the upper and lower fit errors are taken from the means of the MINOS error distributions of the fits included in the gap fraction calculation. Performing the 2-D fit over these LØ and calorimeter multiplicity ranges, we have obtained the gap fraction:

$$\frac{W_{diffractive}}{W_{all}}$$

for several different electron samples.

Tables 4.5 and 4.6 show the gap fraction for the central and forward electron W event samples. Table 4.7 shows the gap fractions for several combined central and forward e W samples. These gap fractions are found using fits of the same sample to find both the background and signal shape. In each case, both the raw gap fraction from the fit and the gap fraction *corrected* for residual multiple interaction

contamination are given. All comparisons between fit results must be done using the *corrected* fraction rather than the raw fit result. After the multiple interaction contamination for each sample is taken into account, we have an accurate fraction of diffractive W to all W events. We can see that the signal for the central electron sample is higher than that for the forward e sample. As would be expected, the combined central and forward electron sample has a gap fraction between that for the individual samples.

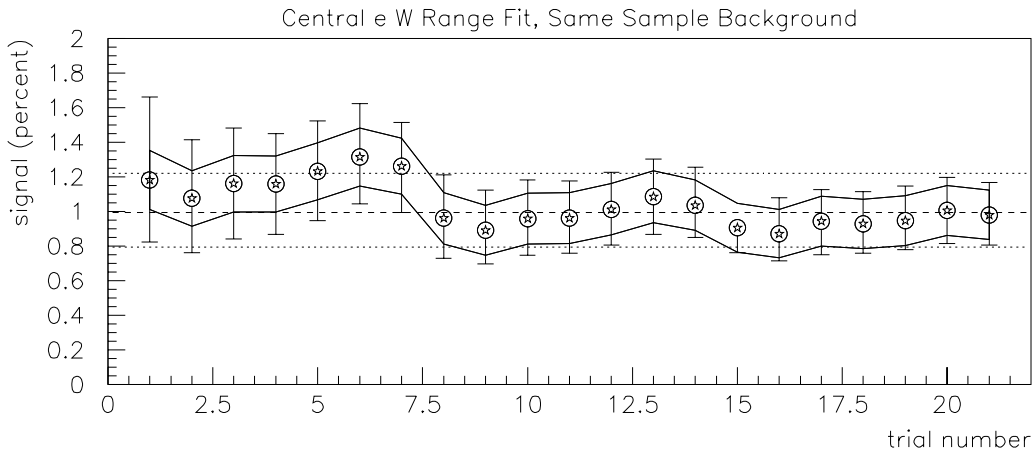

Figure 4.16. The fit results for the 1800 GeV central electron W data sample. Shown is the variation of the signal for fits using an upper limit range of 5-7 in LØ bins and 6-12 in n_{CAL} bins (top). Trial number 1 corresponds to a fit using (LØ ,n_{cal}) upper limits of (5,6). Trial number 2 corresponds to a fit with upper limits of (5,7) and so on until trial number 8 with limits (6,6). Trial number 15 begins the series of fits with LØ upper limit = 7, ending with limits (7,12) for trial 21. The bands represent the parabolic errors from MINUIT and the error bars show the MINOS errors.

It is also important to look for systematic dependence of the gap fraction on event characteristics and fit shape. Tables 4.5 and 4.6 show how the central and forward gap fractions change when different event selection requirements were used.

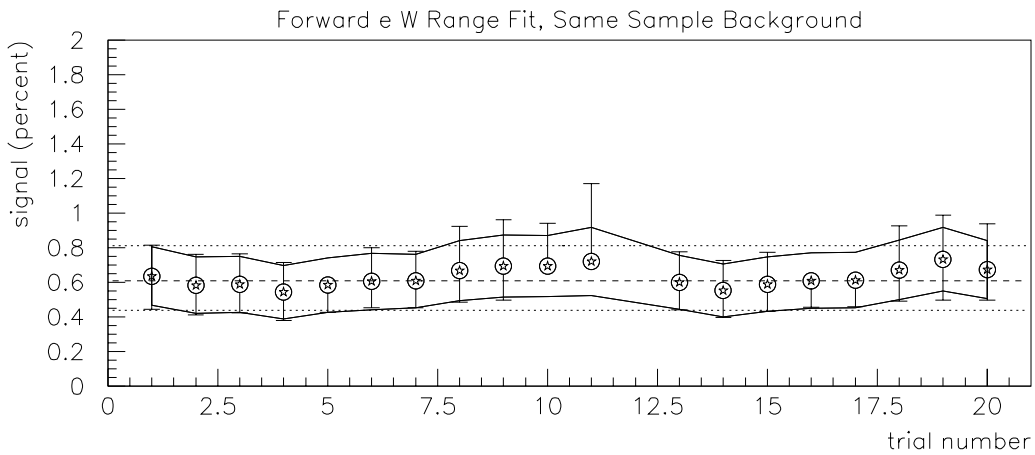

Figure 4.17. The fit results for the 1800 GeV forward electron W data sample. Shown is the variation of the signal for fits using an upper limit range of 5-6 in LØ bins and 6-15 in n_{CAL} bins (top). The upper limits in LevelØ and n_{cal} are stepped through as in the central electron range fit. The bands represent the parabolic errors from MINUIT and the error bars show the MINOS errors.

The 'tight' electron requirement was relaxed to a 'loose' electron (see Table 4.1), the $\not\!\!E_T$ and E_T requirement on the electron were raised to 30 GeV, and the EM calorimeter threshold was lowered to 125 MeV and raised to 200 MeV. The multiple interaction cut was also changed to require mirun1=1,2, and the central electron sample was separated into two different luminosity bins ($\leq 7 \times 10^{30}$ and $> 7 \times 10^{30}$). This is a first look for systematics like residual contamination which would change with luminosity. It is worthwhile to compare the gap fraction found with the chosen fit shape, which has a 4 parameter background, to that found with a 6 parameter background. The extra parameters allow the background shape to have quadratic elements in both $n_{L\emptyset}$ and n_{CAL}.

The gap fractions are consistent within error bars for each variation on the event selection, including the changing EM thresholds and the bins in luminosity. This is true for the central electron samples, the forward electron samples, and the combined sample. Although the six parameter fit result is within error bars of the standard fit result, it does appear to give a consistently higher fraction. The errors for the six parameter fit are also higher than for the four parameter background fit. The fit to the maximum side of the detector is also shown in Table 4.7 for the combined central and forward sample. The gap fraction is very low, nearly zero, which is expected and confirms the fit method.

The central electron W sample is also split into two η bins which give the dependence of the gap fraction on η when combined with the forward electron sample. See Table 4.8 for the gap fraction results as a function of η. There is a definite η dependence on the diffractive W rate, with the very central ($\eta < 0.5$) and forward ($1.5 \leq \eta < 2.5$) electron samples being much lower than that for the mid-central sample ($0.5 \leq \eta < 1.1$) by about a factor of three.

Diffractive W bosons can also be produced via the $gq \rightarrow Wq$ process which

Table 4.5. Measured gap fractions for the far gap region for central electron Ws at 1800 GeV center-of-mass energy. The gap fractions were obtained using the range fit method where BOTH SIGNAL and BACKGROUND shapes were taken from the SAME SAMPLE. The raw gap fraction obtained directly from the fit is given for each sample. This raw fraction is then corrected for residual multiple interaction event contamination for each sample using the contamination values listed in Table 4.3.

Central e W **Event Sample**	Fitted Gap Fraction	Corrected Gap Fraction
standard e cuts	$0.99\ \pm^{0.25}_{0.24}$ %	$1.09\ \pm^{0.28}_{0.27}$ %
loose e quality	$1.04\ \pm^{0.23}_{0.21}$ %	$1.13\ \pm^{0.26}_{0.24}$ %
E_T, $\not{E}_T$ >30 GeV	$0.86\ \pm^{0.24}_{0.21}$ %	$0.96\ \pm^{0.27}_{0.24}$ %
lum ≤ 7	$1.20\ \pm^{0.32}_{0.28}$ %	$1.23\ \pm^{0.33}_{0.29}$ %
lum > 7	$0.70\ \pm^{0.24}_{0.20}$ %	$0.84\ \pm^{0.25}_{0.25}$ %
6param fit	$1.27\ \pm^{0.45}_{0.36}$ %	$1.40\ \pm^{0.50}_{0.41}$ %
Emthresh 125 MeV	$0.84\ \pm^{0.24}_{0.21}$ %	$0.93\ \pm^{0.27}_{0.24}$ %
Emthresh 200 MeV	$1.13\ \pm^{0.25}_{0.26}$ %	$1.24\ \pm^{0.28}_{0.30}$ %
mirun1=1,2 novtx cut	$0.66\ \pm^{0.17}_{0.15}$ %	$0.86\ \pm^{0.23}_{0.20}$ %
miflag=0,1 novtx cut	$0.87\ \pm^{0.20}_{0.21}$ %	$1.19\ \pm^{0.28}_{0.30}$ %

Table 4.6. Measured gap fractions for the far gap region for forward electron Ws at 1800 GeV center-of-mass energy. The gap fractions were obtained using the range fit method where BOTH SIGNAL and BACKGROUND shapes were taken from the SAME SAMPLE. The raw gap fraction obtained directly from the fit is given for each sample. This raw fraction is then corrected for residual multiple interaction event contamination for each sample using the contamination values listed in Table 4.3.

Forward e W **Event Sample**	Fitted Gap Fraction	Corrected Gap Fraction
standard e cuts	$0.61 \pm^{0.21}_{0.18}$ %	$0.61 \pm^{0.21}_{0.18}$ %
loose e quality	$0.61 \pm^{0.21}_{0.18}$ %	$0.61 \pm^{0.21}_{0.18}$ %
6param fit	$0.77 \pm^{0.29}_{0.25}$ %	$0.77 \pm^{0.29}_{0.25}$ %
Emthresh 125 MeV	$0.60 \pm^{0.26}_{0.20}$ %	$0.60 \pm^{0.26}_{0.20}$ %
Emthresh 200 MeV	$0.65 \pm^{0.28}_{0.21}$ %	$0.65 \pm^{0.28}_{0.21}$ %
mirun1=1,2 novtx cut	$0.53 \pm^{0.16}_{0.15}$ %	$0.64 \pm^{0.20}_{0.19}$ %
miflag=0,1 novtx cut	$0.48 \pm^{0.16}_{0.13}$ %	$0.60 \pm^{0.20}_{0.17}$ %

Table 4.7. Measured gap fractions for the far gap region for the combined central and forward electron W's at 1800 GeV center-of-mass energy. The gap fractions were obtained using the range fit method where BOTH SIGNAL and BACKGROUND shapes were taken from the SAME SAMPLE. The raw gap fraction obtained directly from the fit is given for each sample. This raw fraction is then corrected for residual multiple interaction event contamination for each sample using the contamination values listed in Table 4.4.

Combined Cen + Fwd e W **Event Sample**	Fitted Gap Fraction	Corrected Gap Fraction
standard cen+fwd e	$0.84\ \pm^{0.18}_{0.17}$ %	$0.89\ \pm^{0.20}_{0.19}$ %
loose e quality	$0.88\ \pm^{0.17}_{0.16}$ %	$0.93\ \pm^{0.19}_{0.18}$ %
E_T,$\not\!\!E_T$ >30 GeV	$0.76\ \pm^{0.14}_{0.13}$ %	$0.82\ \pm^{0.16}_{0.15}$ %
lum ≤ 7	$1.03\ \pm 0.23$%	$1.03\ \pm^{0.23}_{0.23}$ %
lum > 7	$0.68\ \pm 0.15$%	$0.78\ \pm^{0.19}_{0.18}$ %
6param fit	$1.13\ \pm^{0.36}_{0.34}$ %	$1.20\ \pm^{0.39}_{0.37}$ %
Emthresh 125 MeV	$0.72\ \pm^{0.17}_{0.15}$ %	$0.77\ \pm^{0.19}_{0.17}$ %
Emthresh 200 MeV	$0.96\ \pm^{0.17}_{0.15}$ %	$1.02\ \pm^{0.19}_{0.17}$ %
mirun1=1,2 novtx cut	$0.61\ \pm^{0.13}_{0.11}$ %	$0.78\ \pm^{0.17}_{0.15}$ %
miflag=0,1 novtx cut	$0.72\ \pm^{0.16}_{0.14}$ %	$0.95\ \pm^{0.22}_{0.19}$ %
North side	$0.65\ \pm 0.19$%	$0.69\ \pm 0.21$%
South side	$0.35\ \pm^{0.07}_{0.06}$ %	$0.37\ \pm^{0.08}_{0.07}$ %
Max mult	$0.04\ \pm^{0.03}_{0.02}$ %	$0.04\ \pm^{0.03}_{0.02}$ %

results in a final state jet with the W. This process is suppressed by order α_s, and the diffractive W production rate will depend highly on the pomeron composition. The parton component of the pomeron involved in the diffractive W production can be found by studying the gap fraction of W+jets events. See Table 4.9 for the number of events in several $W + jet$ samples and Table 4.10 for the gap fraction fit results for each $W + jet$ event sample.

Table 4.8. Measured far gap fractions for several electron η bins at 1800 GeV center-of-mass energy. The gap fractions were obtained using the range fit method where BOTH SIGNAL AND BACKGROUND shapes were taken from the SAME SAMPLE.

W **Event Sample** η **bins**	**Fitted Gap Fraction**	**Corrected Gap Fraction**
$\eta < 0.5$	$0.47 \ \pm^{0.17}_{0.15}$ %	$0.52 \ \pm^{0.19}_{0.17}$ %
$0.5 \leq \eta < 1.1$	$1.43 \ \pm^{0.33}_{0.30}$ %	$1.58 \ \pm^{0.38}_{0.35}$ %
$1.5 \leq \eta < 2.5$	$0.61 \ \pm^{0.21}_{0.18}$ %	$0.61 \ \pm^{0.21}_{0.18}$ %

Table 4.9. Number of events with at least one jet from the central + fwd electron W sample for several jet E_T thresholds.

jet E_T threshold for jets with $\lvert\eta_{jet}\rvert < 3.0$	Num Evts
$E_T > 8$ GeV	2,025
$E_T > 15$ GeV	1,742
$E_T > 25$ GeV	1,531

Motivation for Alternate Background Sample Fit Method

Due to the small number of events in the low statistics samples which include the central W data and the forward electron W, (on the order of 10/bin near the signal region), the fit results vary depending on the initial parameters chosen (see Fig-

Table 4.10. Measured gap fractions for the far gap region for all W+jet events at 1800 GeV center-of-mass energy. Signal extracted using SAME SAMPLE to find SIGNAL and BACKGROUND. NO CORRECTION for residual contamination was performed.

Central + Forward e (W + jet) events Sample	Fitted Gap Fraction
$E_T Jet > 8$ GeV	$0.47 \ \pm^{0.24}_{0.17}$ %
$E_T Jet > 15$ GeV	$0.36 \ \pm^{0.29}_{0.27}$ %
$E_T Jet > 25$ GeV	$0.38 \ \pm^{0.24}_{0.16}$ %

ures 4.16 and 4.17). This is especially true for the Z sample, in fact, it is impossible to get a fit of the Z sample as described above. It is therefore advantageous to find a reasonable way to increase statistics in order to establish the background shape. With a more populated background multiplicity, the shape becomes more apparent and the fit results stabilize.

We use several methods to increase the statistics used in the fit: (i) we combine the central and forward electron samples (see Fig. 4.18), (ii) we loosen the electron quality cuts, and (iii) we change the multiple interaction cuts such that mirun1=1,2 with no restriction on the value of miflag or the number of vertices in the event. The last case increases the number of events by including multiple interaction events which were previously removed when a purely single interaction sample was the selection goal. Restrictions on miflag and the number of event vertices would remove likely multiple interaction events from the sample. Here, we are interested in keeping more events, so we keep the multiple interaction events.

For each method, there must be no bias effects that would alter the background shape. In other words, we must ensure that the background shapes in the high statistics samples are not fundamentally different from those in the low statistics

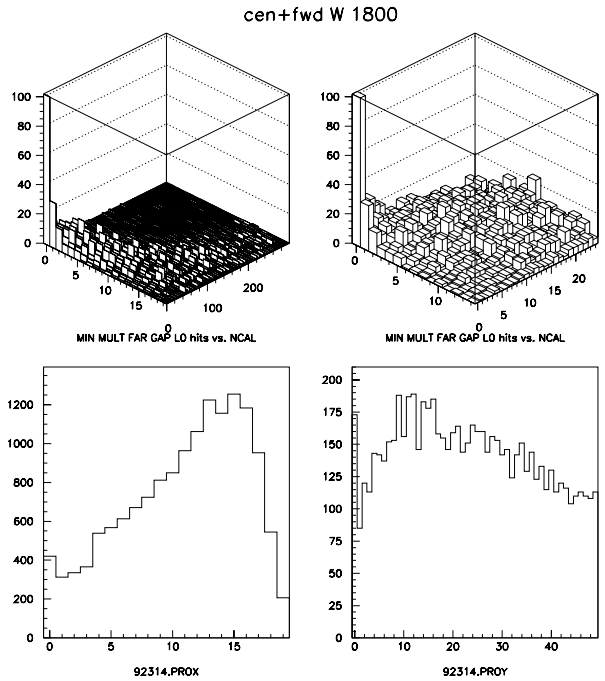

Figure 4.18. The 2-D multiplicity of LØ tiles and calorimeter towers above threshold in the minimum multiplicity far gap region for the combined central and forward electron W samples.

samples. The mean of the minimum side calorimeter multiplicity is a gauge of the background shape, and is given in Table 4.11 for several central electron W event samples, Table 4.12 for forward electron W, and Table 4.13 for several Z samples. The samples can basically be separated into two categories: relatively low statistics samples where we would like to measure the gap fraction signal, and high statistics samples that we would like to use to find the background shape to aid in the fitting of the smaller statistics samples.

Table 4.11. Mean of the minimum side calorimeter multiplicity for several electron W samples.

Central e W Event Sample	Mean Min Multiplicity (GeV)	Num Events
standard	65.61	8,724
lum ≤ 7	69.23	4,746
lum > 7	61.28	3,978
$0.0 \leq \|\eta\| < 0.5$	65.31	4,109
$0.5 \leq \|\eta\| < 1.1$	66.45	4,173
E_T,$\not\!\!E_T$ >30 GeV	65.38	6,206
EMthresh 125 MeV	68.91	8,724
EMthresh 200 MeV	62.95	8,724
Potential bkgnd shape samples		
standard central+fwd	64.86	12,622
cen+fwd EMthr 125MeV	68.14	12,622
cen+fwd EMthr 200MeV	62.20	14,768
cen loose e quality cuts	65.79	9,000
cen mirun1=1,2 no vtx cut	67.37	10,366
cen flag=0,1 no vtx cut	80.52	10,803
Central + Fwd W+jet samples		
$E_T Jet > 8$ GeV	79.87	2,025
$E_T Jet > 15$ GeV	79.95	1,742
$E_T Jet > 25$ GeV	79.38	1,531

The background shapes can be directly compared by looking at the 1-D minimum side calorimeter multiplicity distributions. (See Figs 4.19, 4.20, 4.21, 4.22, and 4.23). Generally, samples which have a higher mean multiplicity on the minimum side are those in which the multiple interaction selection cuts were altered. A higher mean

Table 4.12. Mean of the minimum side calorimeter multiplicity for several forward electron W samples.

Forward e W Sample	Mean Min Multiplicity (GeV)	Num Events
standard	63.19	3,898
E_T,$\not\!\!E_T$ >30 GeV	62.76	2,768
EMthresh 125 MeV	66.44	3,898
EMthresh 200 MeV	60.52	3,898
Potential bkgnd shape samples		
fwd loose e quality cuts	63.25	3,908
fwd mirun1=1,2 no vtx cut	66.07	4,765
fwd flag=0,1 no vtx cut	81.59	4,909

Table 4.13. Mean of the minimum side calorimeter multiplicity for several Z samples.

Z Sample	Mean Min Multiplicity (GeV)	Num Events
standard	61.37	715
EMthresh 125 MeV	64.47	715
EMthresh 200 MeV	58.83	715
standard with EC-EC	62.04	801

indicates that more multiple interaction events were included in the sample. This was verified in the residual contamination study for different data samples. As we can see from both the mean minimum multiplicities and the overlaid multiplicity distributions, the background shape of the combined central and forward electron W sample agrees well with that of the individual central W, forward W, and Z samples. Therefore, it is reasonable to use the combined central e and forward e as the background shape for a fit to the smaller statistics sample. Similarly, the mirun1 cut and the loose quality cut samples for central and forward electron W's can be used to find the background shape of the low statistics samples. The loose electron quality cut variation does not gain much in statistics, so we don't expect much of a change if it is used to find the background shape.

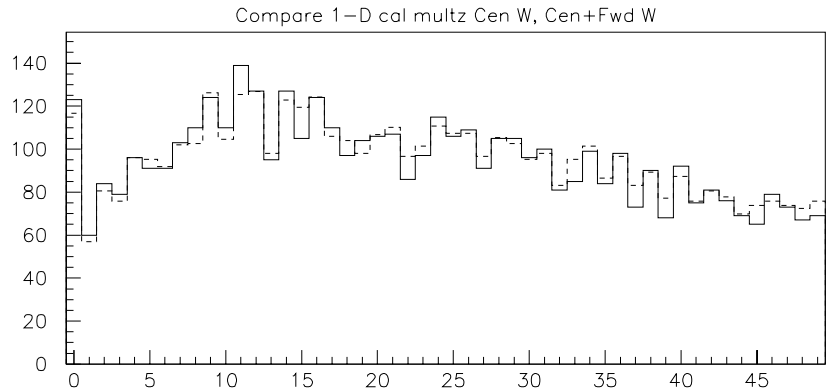

Figure 4.19. One dimensional calorimeter multiplicity distributions (the number of calorimeter towers hit on the x-axis and the number of events on the y-axis). The solid line is the Central W electron sample, and the dashed line is the combined Central + Forward W samples, which is scaled to the central sample.

Range Fit: Alternate Background Sample Fit Method

This second evolution of the fitting is a more complicated version of the earlier method. We will still be fitting the signal with a falling exponential and the background with a plane, but the two parts of the fit will be done on separate data

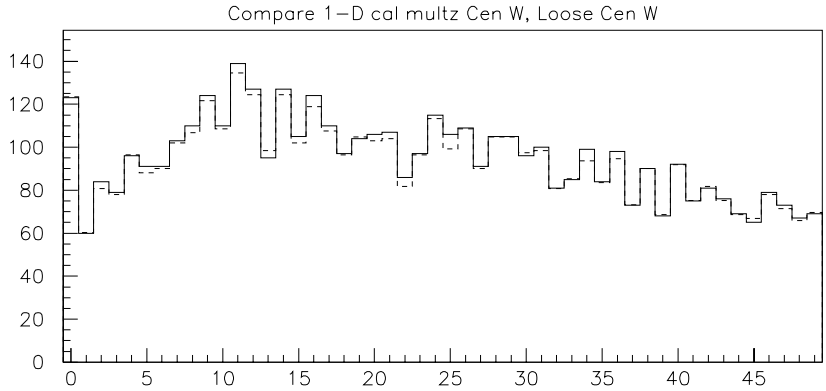

Figure 4.20. One dimensional calorimeter multiplicities distributions (the number of calorimeter towers hit on the x-axis and the number of events on the y-axis). The solid line is the standard Central W electron sample, and the dashed line is the Central loose electron quality cut sample, which is scaled to the standard central sample.

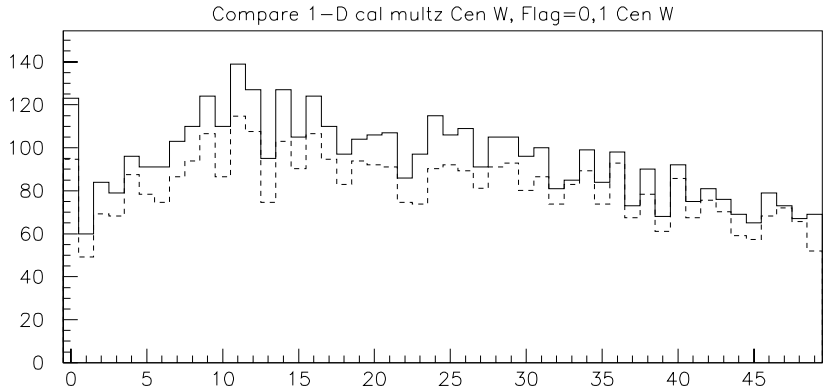

Figure 4.21. One dimensional calorimeter multiplicities (the number of calorimeter towers hit on the x-axis and the number of events on the y-axis). The solid line is the standard Central W electron sample, and the dashed line is the Central electron sample where only an miflag multiple interaction cut was imposed. Note that the normalization between the two distributions is correct. The miflag sample multiplicity distribution is pushed out to much higher n_{cal} than the standard sample. This is an indication that the miflag sample background shape does not match that of the standard sample; therefore, it is not used for the Alternate Background Sample Fitting Method.

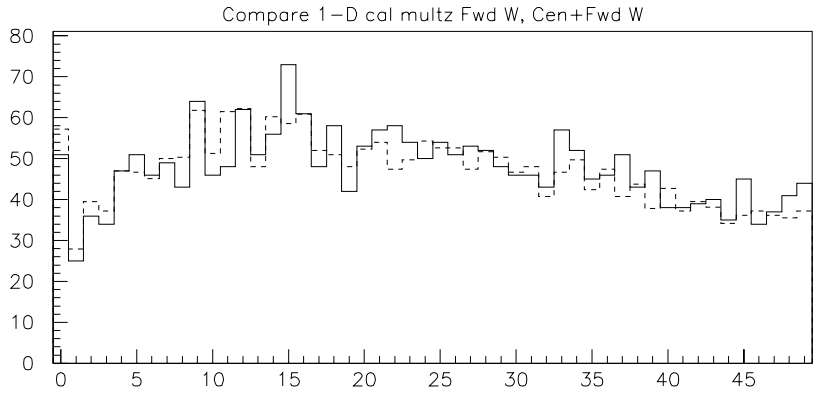

Figure 4.22. One dimensional calorimeter multiplicities: the solid line is the standard Forward W electron sample, and the dashed line is the combined Central + Forward W sample which has been scaled to the forward electron W sample size.

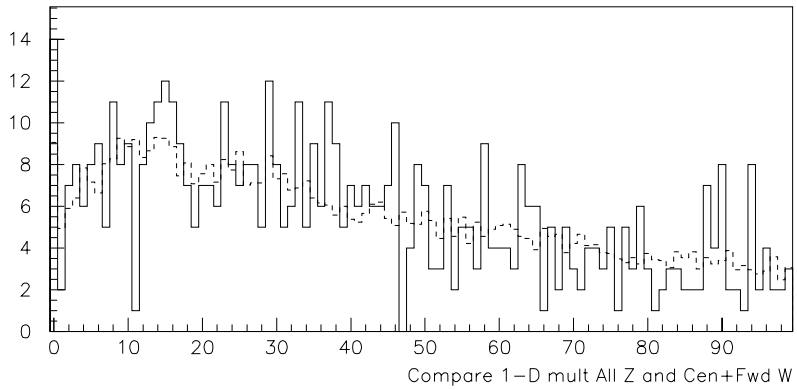

Figure 4.23. One dimensional calorimeter multiplicities: the solid line is the standard Z sample, and the dashed line is the combined Central+Forward W sample which has been scaled to the Z sample size.

samples. We will be using one of several high statistics samples to find the 2-D background shape. As an example, consider the specific case where we want a signal from the central electron W's using the combined central plus forward sample to obtain the background shape. Initially, the 2-D simultaneous signal and background fit is done on the central+forward sample. The background parameters from this fit are saved and scaled to the sample size of the central e W's. They are then used as input parameters to the fit of the central e sample. During the fitting of the central electron sample, the background shape is fixed and only the signal parameters are included in the fit.

Figures 4.24, 4.25, and 4.26 show *one fit* for the central e W's, the forward e W's, and the Z samples respectively. As before, this process is repeated over a systematically varied range of $n_{L\emptyset}$ and n_{CAL} limits to remove any signal dependence on the fit region chosen. The result is a distribution of gap fractions from the fit, and the final signal is defined to be the mean of this distribution. The gap fraction distributions for the central e W's, forward e W's, and Z's are shown in Figures 4.27, 4.28, and 4.29. Due to the very small statistics in the Z sample, the fit was difficult to complete even using the alternate background shape. Final gap fraction results are shown in Table 4.14 for central electron Ws, in Table 4.15 for forward electron Ws, in Table 4.16 for Zs, and in Table 4.17 for $W + jet$ events. In each case, the error is due to fitting systematics and statistics.

4.3.3 Event Characteristics

To ensure that the rapidity gap signatures are not due to pathologically unusual W or Z boson events or fakes in the signal region ($n_{L0} = n_{CAL} = 0$), various event characteristics are examined. Figure 4.30 shows the electron E_T, $\not{E}_T$, and transverse mass for central electron W events with $n_{CAL} > 1$, which are dominantly non-diffractive (left column), and diffractive W candidate events ($n_{L0} = n_{CAL} = 0$,

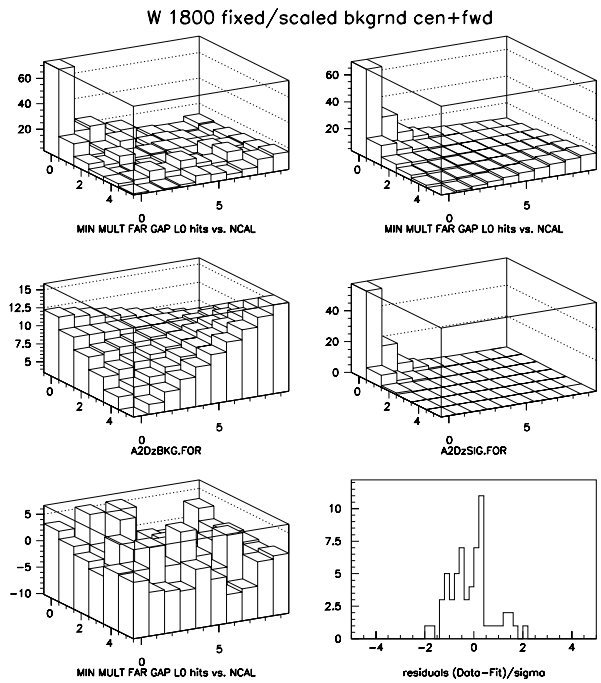

Figure 4.24. Two dimensional multiplicities (LØ vs calorimeter towers) from a single 2D fit extraction of the quantitative signal for the central electron W sample. The background shape was taken from the combined central+forward electron W samples, scaled to the statistics in the central only W sample, and fixed for the fitting procedure. The top two plots show i) only the data $n_{L\emptyset}$ vs. n_{CAL} multiplicity plot, and ii) the signal and background $n_{L\emptyset}$ vs. n_{CAL} multiplicity distribution from the fit. The middle plots show the individual multiplicities for iii) the background,and iv) the signal from the fit. (Note: these two middle plots combine to produce the top right distribution.) Finally, the bottom plots show v) data - fit, and vi) residuals for this individual fit.

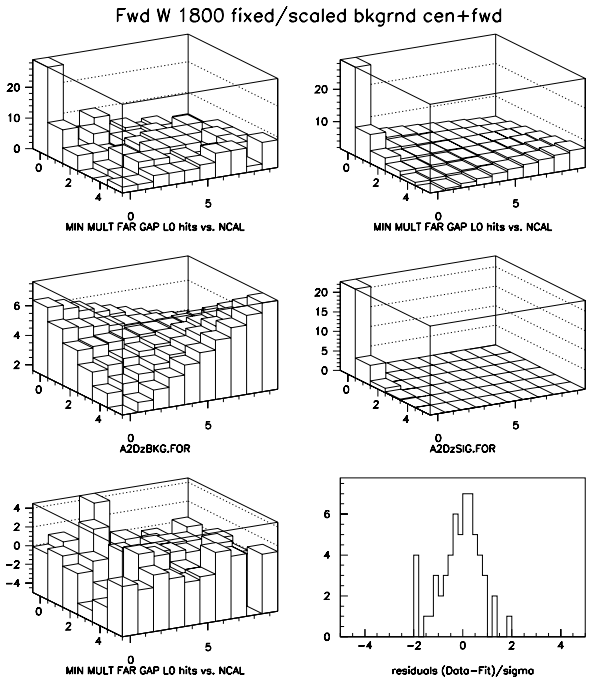

Figure 4.25. Two dimensional multiplicities (LØ vs calorimeter towers) from a single 2D fit extraction of the quantitative signal for the forward electron W sample. The background shape was taken from the combined central+forward electron W samples, scaled to the statistics in the forward only W sample, and fixed for the fitting procedure. The top two plots show i) only the data $n_{L\emptyset}$ vs. n_{CAL} multiplicity plot, and ii) the signal and background $n_{L\emptyset}$ vs. n_{CAL} multiplicity distribution from the fit. The middle plots show the individual multiplicities for iii) the background,and iv) the signal from the fit. (Note: these two middle plots combine to produce the top right distribution.) Finally, the bottom plots show v) data - fit, and vi) residuals for this individual fit.

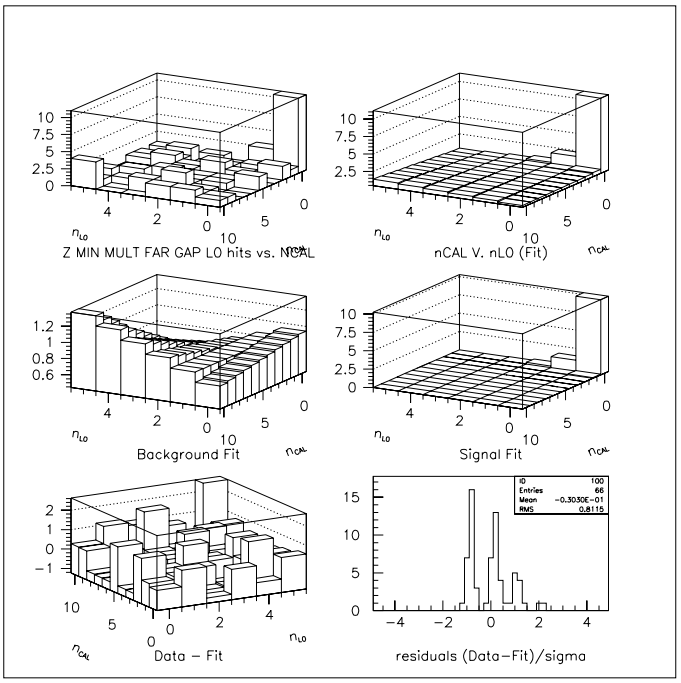

Figure 4.26. Two dimensional multiplicities (LØvs calorimeter towers) from a single 2D fit extraction of the quantitative signal for the Z sample. The background shape was taken from the combined central+forward electron W samples, scaled to the statistics in the Z sample, and fixed for the fitting procedure. The top two plots show i) only the data $n_{L\emptyset}$ vs. n_{CAL} multiplicity plot, and ii) the signal and background $n_{L\emptyset}$ vs. n_{CAL} multiplicity distribution from the fit. The middle plots show the individual multiplicities for iii) the background,and iv) the signal from the fit. (Note: these two middle plots combine to produce the top right distribution.) Finally, the bottom plots show v) data - fit, and vi) residuals for this individual fit.

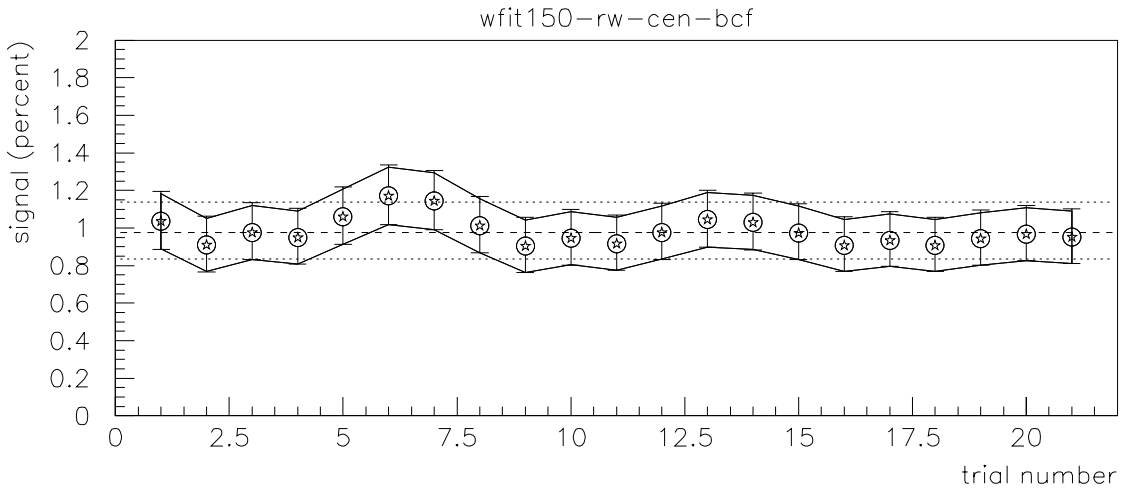

Figure 4.27. The fit results for the 1800 GeV central electron W data sample are presented. Shown is the variation of the signal for fits using an upper limit range of 5-7 in LØ bins and 6-12 in n_{CAL} bins (top). The bands represent the parabolic errors from MINUIT and the error bars show the MINOS errors. The combined central and forward electron W sample was used to find the background shape for this fit.

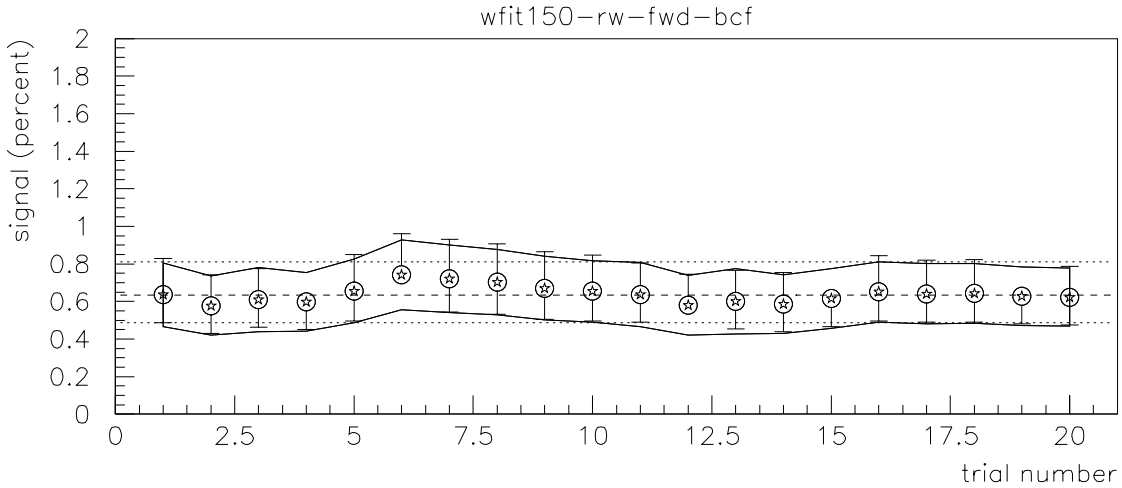

Figure 4.28. The fit results for the 1800 GeV forward electron W data sample are presented. Shown is the variation of the signal for fits using an upper limit range of 5-7 in LØ bins and 6-12 in n_{CAL} bins (top). The bands represent the parabolic errors from MINUIT and the error bars show the MINOS errors. The combined central and forward electron W sample was used to find the background shape for this fit.

Table 4.14. Measured gap fractions for the far gap region for central electron W's at 1800 GeV center-of-mass energy using HIGH STATISTICS SAMPLES to determine the BACKGROUND SHAPE.

Central e W Event Sample	**Background Sample**	**Fitted Gap Fraction**	**Corrected Gap Fraction**
standard	cen$W$+fwd$W$	$0.98 \pm^{0.18}_{0.16}$ %	$1.08 \pm^{0.21}_{0.19}$ %
standard	cen+fwd$W$ 125 emthr	$0.96 \pm^{0.17}_{0.15}$ %	$1.06 \pm^{0.20}_{0.18}$ %
standard	cen+fwd$W$ 200 emthr	$1.01 \pm^{0.20}_{0.18}$ %	$1.11 \pm^{0.23}_{0.21}$ %
standard	loose e quality	$1.01 \pm^{0.20}_{0.18}$ %	$1.11 \pm^{0.23}_{0.20}$ %
standard	mirun1=1,2	$0.99 \pm^{0.19}_{0.17}$ %	$1.09 \pm^{0.22}_{0.20}$ %
E_T,$\not\!\!E_T$ >30 GeV	cen$W$+fwd$W$	$0.95 \pm^{0.22}_{0.19}$ %	$1.06 \pm^{0.25}_{0.22}$ %
lum ≤ 7	cen$W$+fwd$W$	$0.96 \pm^{0.21}_{0.19}$ %	$0.99 \pm^{0.22}_{0.20}$ %
lum > 7	cen$W$+fwd$W$	$1.06 \pm^{0.33}_{0.29}$ %	$1.28 \pm^{0.41}_{0.37}$ %
$\eta < 0.5$	cen$W$+fwd$W$	$0.53 \pm^{0.25}_{0.18}$ %	$0.58 \pm^{0.28}_{0.20}$ %
$0.5 \leq \eta < 1.1$	cen+fwd$W$	$1.34 \pm^{0.26}_{0.22}$ %	$1.48 \pm^{0.30}_{0.26}$ %

Table 4.15. Measured gap fractions for the far gap region for forward electron W's at 1800 GeV center-of-mass energy using HIGH STATISTICS SAMPLES to determine the BACKGROUND SHAPE.

W Forward e Sample	**Background Sample**	**Fitted Gap Fraction**	**Corrected Gap Fraction**
standard	cen$W$+fwd$W$	$0.64 \pm^{0.19}_{0.16}$ %	$0.64 \pm^{0.19}_{0.16}$ %
standard	cen loose e	$0.65 \pm^{0.20}_{0.16}$ %	$0.65 \pm^{0.20}_{0.16}$ %
standard	mirun1	$0.68 \pm^{0.22}_{0.18}$ %	$0.68 \pm^{0.22}_{0.18}$ %

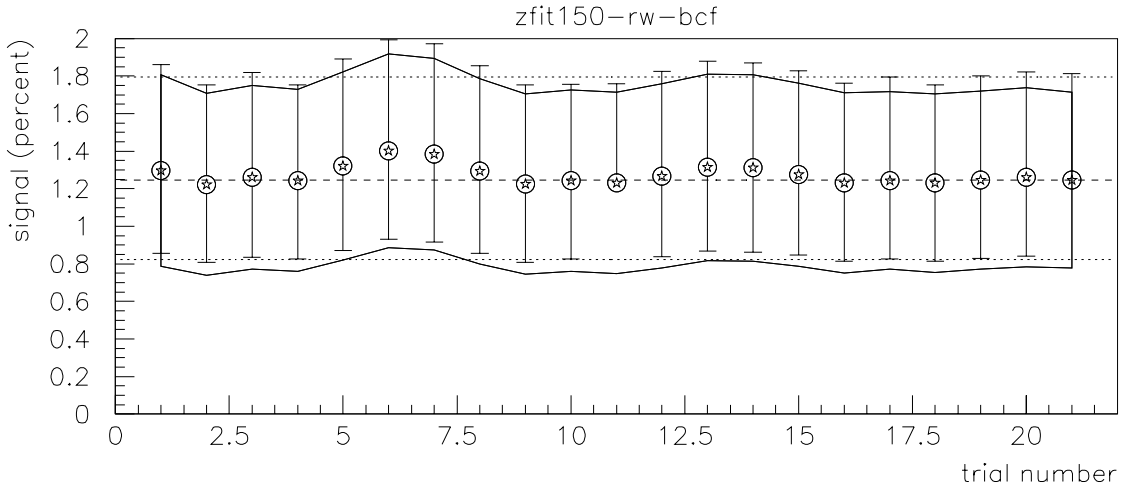

Figure 4.29. The fit results for the 1800 GeV Z data sample are presented. Shown is the variation of the signal for fits using an upper limit $n_{L\emptyset}$ and n_{CAL} range of (5-6:6-12). The bands represent the parabolic errors from MINUIT and the error bars show the MINOS errors. The combined central and forward electron W sample was used to find the background shape for this fit.

Table 4.16. Measured gap fractions for the far gap region for all Z's at 1800 GeV center-of-mass energy. The COMBINED CENTRAL and FORWARD electron W sample was used to find the BACKGROUND SHAPE for the Z sample fit.

Z e **Sample**	**Background Sample**	**Fitted Gap Fraction**	**Corrected Gap Fraction**
standard	cen+fwd W	$1.25\ \pm^{0.56}_{0.43}\ \%$	$1.38\ \pm^{0.62}_{0.48}\ \%$

Table 4.17. Measured gap fractions for the far gap region for all central + forward electron $W + jet$ events at 1800 GeV center-of-mass energy. The COMBINED CENTRAL and FORWARD electron W sample was used to find the BACKGROUND SHAPE for the $W + jet$ samples.

Central e W + jet events Sample	Fitted Gap Fraction
Jet $E_T > 8$ GeV	$0.31 \ \pm^{0.19}_{0.15}$ %
Jet $E_T > 15$ GeV	$0.31 \ \pm^{0.20}_{0.14}$ %
Jet $E_T > 25$ GeV	$0.31 \ \pm^{0.20}_{0.14}$ %

right column). Figure 4.31 shows the same quantities for the forward electron W sample. In spite of low statistics for the diffractive candidates, the distributions for all three variables examined (electron E_T, $\not{E}_T$, transverse mass) are very similar. The mean values of these distributions are almost identical for the standard W events and the rapidity gap events. There is no distinguishable difference between the characteristics of the two samples for either the central or forward electron W's. A similar examination is performed for the diffractive Z candidates using the electron E_Ts and the invariant mass distribution for a standard Z sample and the diffractive candidates. Although there are only a few diffractive Z candidates, again we have found no discernable pathology that would indicate these are not genuine Z events.

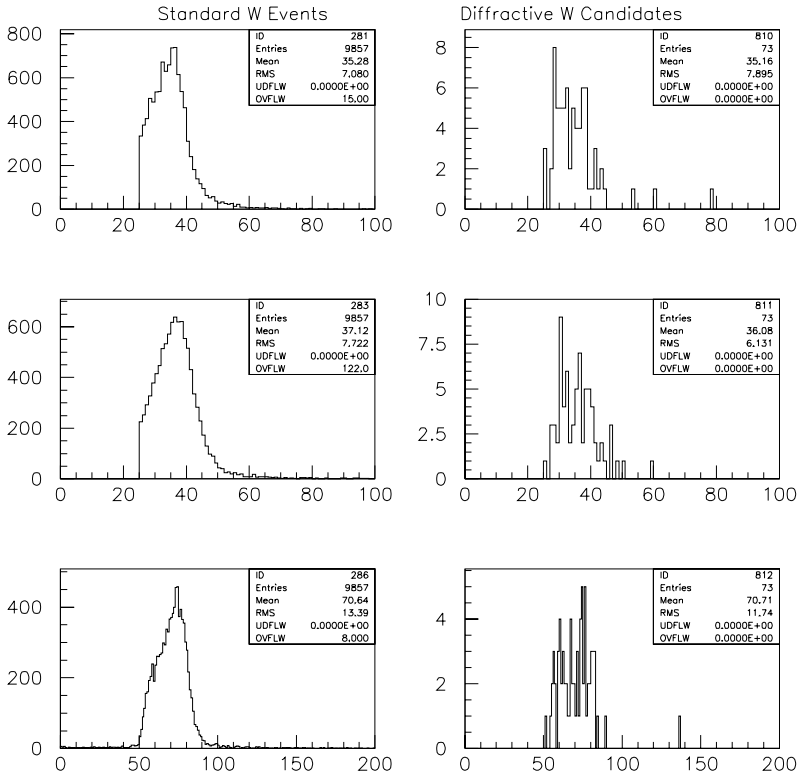

Figure 4.30. Event characteristics for standard central electron W boson events (left column, $n_{CAL} > 1$) compared to diffractive W boson candidate events (right column, $n_{L0} = n_{CAL}$ =0). The top plots compare electron E_T (on the x-axis), the middle show $\not{E}_T$ (on the x-axis) in the events, and the bottom plots compare the transverse mass (x-axis) for the two cases. Note: Events either fall into the standard W event sample or the diffractive candidate event sample; therefore, for each set of comparisons mutually exclusive data sets are examined.

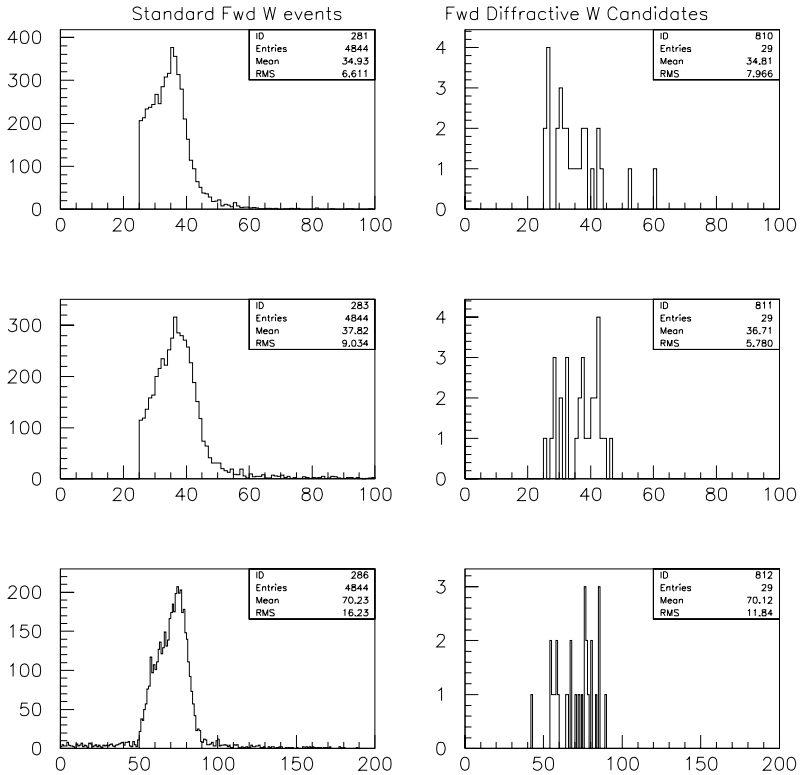

Figure 4.31. Event characteristics for standard forward electron W boson events (left column, $n_{CAL} > 1$) compared to diffractive W boson candidate events (right column, $n_{L0} = n_{CAL}$ =0). The top plots compare electron E_T (on the x-axis), the middle show $\not{E}_T$ (on the x-axis) in the forward electron events, and the bottom plots compare the transverse mass (x-axis) for the two cases. Note: Events either fall into the standard W event sample or the diffractive candidate event sample; therefore, for each set of comparisons mutually exclusive data sets are examined.

CHAPTER 5

MONTE CARLO

POMPYT26 [49] is the Monte Carlo used to model diffractive W and Z scattering at the particle level. As an extension of PYTHIA [50], POMPYT26 has the capability to produce pomeron-proton collisions, where PYTHIA produces $p\overline{p}$ collisions. Several parameters can be varied at generation including the proton structure function, the pomeron flux, and the pomeron structure function. The proton structure function chosen for all following Monte Carlo studies was CTEQ3M [51] [52] [53]. This is the third in a series of proton parton distribution functions (PDFs) determined by the CTEQ Collaboration [54] through a global QCD analysis of fixed target and collider data. The CTEQ3M PDFs incorporate lepton asymmetry data taken at CDF [55] and Drell-Yan data from the NA-51 experiment [56] in addition to the experimental information used for previous iterations of the structure functions.

POMPYT has the capability to model diffractive W and Z production by replacing the standard PYTHIA proton-antiproton collision with a pomeron-proton collision. In reality, either the proton or the antiproton could diffract, but currently POMPYT only permits the antiproton to emit the pomeron. In order to study potential diffractive event production dependence on the pomeron structure, several pomeron structure functions can be selected in POMPYT. These include a hard quark structure, a hard gluon structure, and a soft gluon structure.

The leading order process for diffractive W and Z production is thought to involve a quark structure pomeron. This model consists of two quarks which share

the pomeron momentum: $\frac{6}{4}\beta(1-\beta)$. Diffractive W and Z production is also possible with a hard gluon pomeron, which shares its momentum between two gluons: $6\beta(1-\beta)$. However, this process is suppressed by order α_s and is associated with a jet in the final state with the W or Z. A soft gluon pomeron, $6(1-\beta)^5$, would produce the W and Z through the same mechanism as the hard gluon. However, the fraction of W and Z bosons produced diffractively is expected to be much lower since each parton in the soft gluon model carries only a small fraction of the pomeron momentum. All three of these pomeron structures were examined as part of this study, since any information either proving or disproving expectations about diffractive W and Z production is useful.

Using POMPYT, we can compare the diffractive W and Z results found in data to expectations based on the Ingelman and Schlein model of pomeron exchange [5]. In particular, we can determine the predicted fraction (POMPYT/PYTHIA) of diffractive W and Z-bosons produced for the three pomeron structure functions mentioned above. In order to accomplish a direct comparison to data, we must first learn how efficient the rapidity gap tagging method is at selecting diffractive W and Z events. This 'gap efficiency' is found by combining information from POMPYT Monte Carlo events and non-diffractive data background events. Once the predicted fraction (POMPYT/PYTHIA) and the gap efficiency for each pomeron structure function are known, we can then calculate the final MC diffractive W and Z fractions which can be compared to data. In addition to this comparison, POMPYT can also be used to study the fraction of the proton momentum carried by the pomeron (ξ).

5.1 Method

As in the data, central and forward electron W-boson and Z-boson events are studied in the Monte Carlo. POMPYT is used to generate diffractive W and Z events, while PYTHIA is used to generate the non-diffractive W and Z background. Figure 5.1

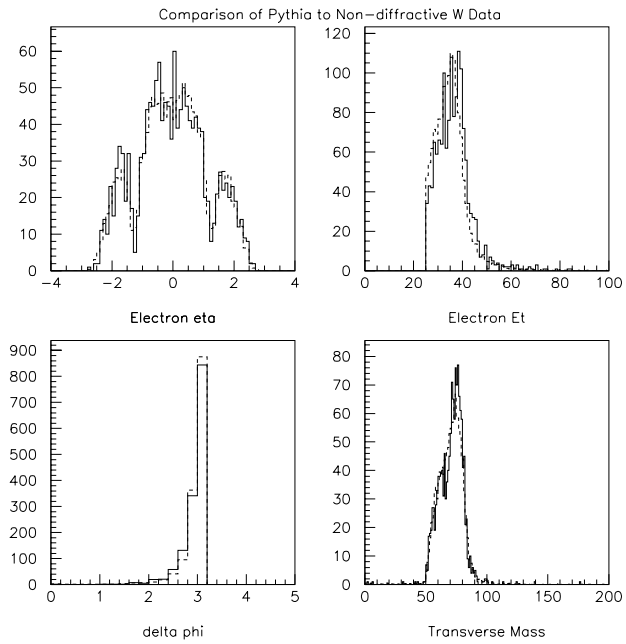

Figure 5.1. Comparison of PYTHIA (solid line) W event characteristics to high multiplicity non-diffractive W data (dashed line). The PYTHIA events have been run through a full simulation of the DØ detector using GEANT. The top left plot shows a comparison of the electron η_d. Note that the distributions both dip around $\eta_d = \pm 1.2$. This is a detector effect. The top right plot shows a comparison of the electron E_T for PYTHIA and the non-diffractive data. The bottom left plot shows a comparison of $\Delta\phi$ for the electron and neutrino. This shows that they are equally back-to-back in data and PYTHIA. Finally, the bottom right plot shows the transverse mass for both PYTHIA and non-diffractive data.

shows a comparison of event characteristics for PYTHIA W events (solid line) and high multiplicity non-diffractive W data (dashed line). For this comparison, the PYTHIA events have been run through the detector simulation (GEANT [57]). As shown in each histogram, the Monte Carlo recreates the data characteristics very well. Additionally, PYTHIA is a well established Monte Carlo that has been used in precision W and Z measurements [44] [45], and we can be confident that it provides a reliable reproduction of non-diffractive W and Z data.

As in data, we look at the side of the detector with the fewest calorimeter towers above threshold in a search for rapidity gaps. This minimum side multiplicity

distribution is shown in Figure 5.2 for both POMPYT and PYTHIA forward electron Ws at particle level. This is before any processing through a trigger simulation or detector simulation. The diffractive distribution in POMPYT is distinctly peaked at zero, while the PYTHIA multiplicity shows a broad distribution with a much higher mean that tapers off to zero to both sides. The marked difference between these distributions indicates that multiplicity is an appropriate variable for identifying diffractive events using rapidity gaps.

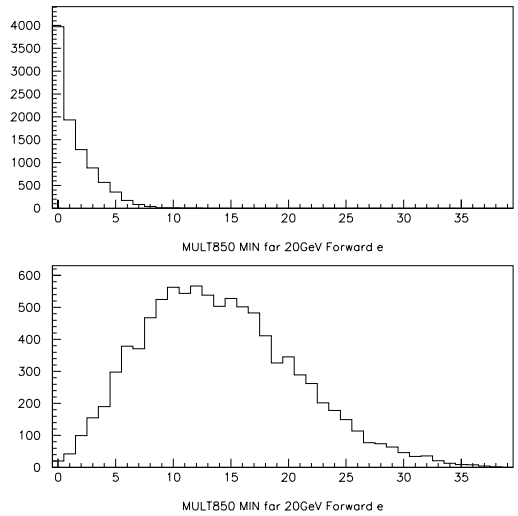

Figure 5.2. POMPYT (top plot) and PYTHIA (bottom plot) minimum side particle multiplicity distributions using a far gap for forward electron W's. The POMPYT multiplicity is peaked at low multiplicities, while the PYTHIA multiplicity is a broad distribution with a much higher mean.

The minimum side multiplicity is used rather than the side opposite the gap because the electron can be on the same side of the detector as the rapidity gap (see Fig. 5.3). This is true even though the diffractive events are pushed forward in rapidity. Since the pomeron carries a small fraction of the initial proton momentum, the W and Z events are expected to be boosted in the lab frame. The amount of

boost depends on the pomeron structure assumed. For example, the soft gluons involved in W production on average carry much less momentum than the hard gluons or quarks from the pomeron; therefore, the soft gluon events will be pushed farther forward than quark events. This difference can be seen in Figure 5.3 where the soft gluon events (dotted line) are definitely farther forward in η than the quark or hard gluon events.

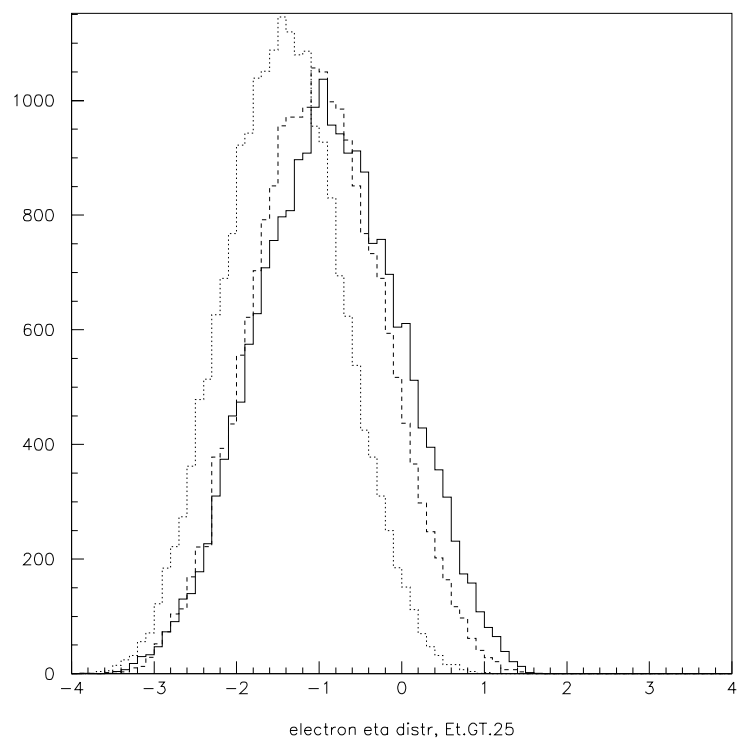

Figure 5.3. The electron η distributions for W boson events generated in POMPYT using a quark pomeron structure (solid line), a hard gluon structure (dashed line), and a soft gluon structure (dotted line). The rapidity gap for all events in these samples is located at $+\eta$. Although it is less common, it *is* possible for the electron to be located on the same side as the gap.

Since POMPYT and PYTHIA have both been incorporated into the DØ zebra structure, events can be run through the full detector simulation (GEANT). Monte

Carlo events can then be processed in the same manner as the data. The Monte Carlo event samples are selected using the same requirements on electron E_T, $\not\!\!E_T$, detector location, and electron quality (see Tables 4.1 and 4.2) as in the data. The sample of diffractive W-boson events is divided into those with central electrons and those with forward electrons. As in data, the Z sample contains CC-CC and CC-EC electron events. This parallel handling of events facilitates Monte Carlo comparisons to data. The two dimensional Level Ø and calorimeter tower (above threshold) multiplicity distributions for central electron POMPYT and PYTHIA W-boson events after GEANT [57] are shown in Fig. 5.4. Again, it is very clear that the diffractive distribution peaks at (0,0) while the non-diffractive distribution drops off to zero at low multiplicity. Although the POMPYT distribution does favor the low multiplicity bins, there *are* events at slightly higher multiplicities. This becomes more evident when the gap efficiency is calculated for several Monte Carlo samples.

5.2 Gap Efficiency

In order to compare the Monte Carlo model to data, we need to determine the fraction of diffractive W and Z bosons predicted by POMPYT. However, not every diffractive W or Z event registers as a rapidity gap event. In some events, the gap is spoiled by a particle from the interaction; therefore, the particle multiplicity registers as nonzero. These events populate the tails of the POMPYT distributions in figures 5.2 and 5.4. We therefore need to know what our efficiency is for finding diffractive events by tagging rapidity gaps. In other words, the visible fraction of diffractive W bosons must be found for each Monte Carlo pomeron model. This quantity is called the 'gap efficiency' (ϵ_{gap}) and must also be determined for the diffractive Z Monte Carlo. For each structure function used, the gap efficiency associated with that model corrects the Monte Carlo fraction for comparison to

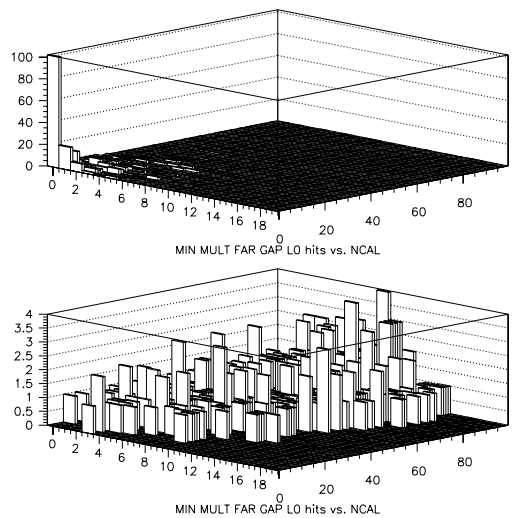

Figure 5.4. The quark pomeron POMPYT (top plot) and PYTHIA (bottom plot) n_{LO} vs n_{CAL} minimum side multiplicity distributions in the far gap region for central electron W's.

data. This puts all pomeron models on the same level, where $f_{visible} = f_{true} \times \epsilon_{gap}$ can be directly compared to f_{data}.

We extract the gap efficiency by simultaneously fitting a non-diffractive background and the diffractive signal. This is done in the same manner as the signal extraction for the data. The two-dimensional LevelØ and calorimeter tower Monte Carlo multiplicity distribution is combined with the background fit multiplicity from the appropriate data sample. In data, the final gap fraction was determined using the background shape taken from the combined central electron and forward electron W sample. Therefore, the combined central and forward sample is also used to calculate the gap efficiency. First, the standard two-dimensional simultaneous fit is performed on the data sample to extract the background shape (see Fig. 5.5). The POMPYT LevelØ vs. calorimeter tower multiplicity is then added to this background shape. The new distribution is fit and the number of visible POMPYT

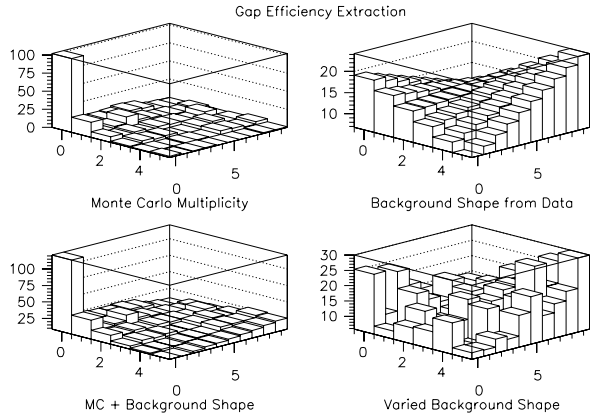

Figure 5.5. The gap efficiency was extracted by simultaneously fitting a non-diffractive background and the diffractive signal. The Monte Carlo Level Ø vs. calorimeter tower multiplicity (top left histogram) and the background multiplicity histogram from a fit to data (top right) were added together (bottom left). This combined sample was then fit several times to find the number of Monte Carlo events detected. Each fit used a slightly different background shape (example at bottom right).

events is extracted. The nominal gap efficiency is then the number of signal events from the fit divided by the true number of POMPYT events in the sample. The process is repeated, each time manipulating the background shape about its mean value to remove any potential bias from the exact shape. The gap efficiency error is then calculated using the rms from the distribution of fit results as well as the systematic error based on the 13% energy scale difference between Monte Carlo and data [58].

Table 5.1 shows the quark, hard gluon, and soft gluon gap efficiencies for central and forward electron W samples and the Z sample. For these events, the maximum possible ξ (the fraction of the proton momentum carried by the pomeron) value was

limited to: $\xi_{max} = 0.1$ at generation. Diffraction is thought to dominate for $\xi \leq 0.1$, although it has been shown that rapidity gap events can be produced for much higher values of ξ. It was recently shown that the ξ distribution for diffractively produced dijet systems extended well beyond 0.1 for events produced at $\sqrt{s} = 1800$ GeV [59]. For this analysis, the gap efficiencies and Monte Carlo rapidity gap fractions were calculated for events generated with $\xi_{max} = 0.1$ and with $\xi_{max} = 0.2$. Figures 5.6 and 5.7 show the central and forward electron W Monte Carlo multiplicity plots for the three pomeron structure models. Figure 5.8 shows the Monte Carlo multiplicity distributions for diffractive Z events. Table 5.2 shows the number of central W, forward W, and Z POMPYT events for the three pomeron structures.

Table 5.1. Gap efficiencies for several structure function models of diffractive W and Z boson production using events generated with the POMPYT Monte Carlo package. The maximum possible ξ value was limited to: $\xi_{max} = 0.1$ at generation.

Pomeron Structure Function	**Sample**	**Gap Efficiency**
QUARK	central electron W	21 $\pm$ 4%
	forward electron W	35 $\pm$ 6%
	Z (CC-CC, CC-EC electrons)	21 $\pm$ 4%
HARD GLUON	central electron W	33 $\pm$ 5%
	forward electron W	42 $\pm$ 6%
	Z (CC-CC, CC-EC electrons)	33 $\pm$ 5%
SOFT GLUON	central electron W	2 $\pm$ 1%
	forward electron W	5 $\pm$ 1%
	Z (CC-CC, CC-EC electrons)	5 $\pm$ 8%

The gap efficiencies for all samples are rather low, and may seem unfairly so upon initial examination of the relevant multiplicity distributions. However, the

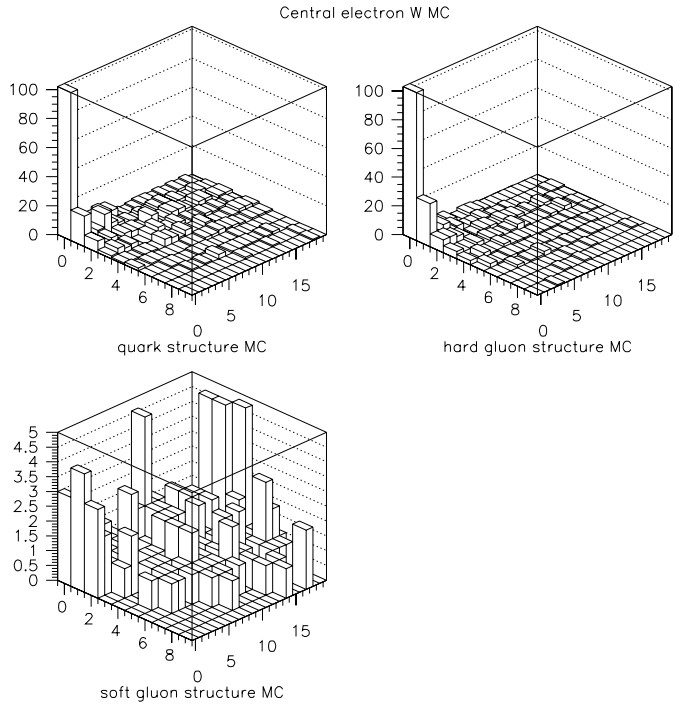

Figure 5.6. Multiplicity distributions for central electron W events are shown for a quark pomeron structure (top left), hard gluon (top right) structure, and soft gluon (bottom left) structure. The distributions for quark and hard gluon structures look very similar and both have a pronounced peak in the (0,0) bin. For each distribution, the LevelØ multiplicity runs from 0 to 10 and the calorimeter tower multiplicity from 0 to 20.

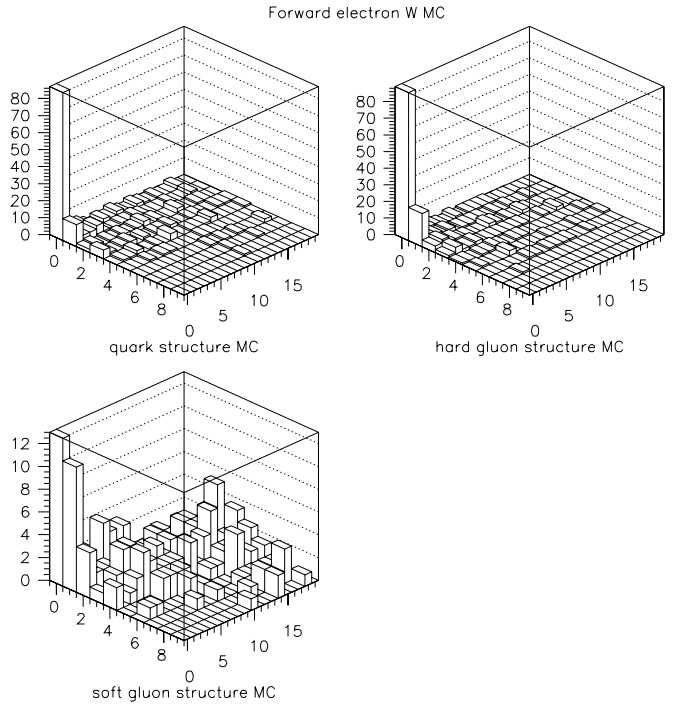

Figure 5.7. Multiplicity distributions for forward electron W events are shown for a quark pomeron structure (top left), hard gluon (top right) structure, and soft gluon (bottom left) structure. As in the central electron case, the distributions for quark and hard gluon structures look very similar and both have a pronounced peak in the (0,0) bin. For each distribution, the LevelØ multiplicity runs from 0 to 10 and the calorimeter tower multiplicity from 0 to 20.

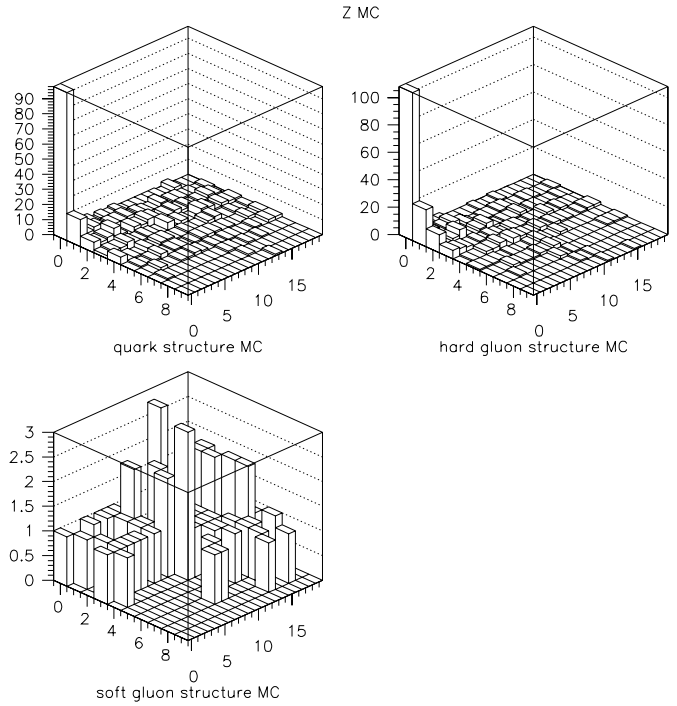

Figure 5.8. Multiplicity distributions for Z events are shown for a quark pomeron structure (top left), hard gluon (top right) structure, and soft gluon (bottom left) structure. Again, the distributions for quark and hard gluon structures look very similar and both have a pronounced peak in the (0,0) bin. For each distribution, the LevelØ multiplicity runs from 0 to 10 and the calorimeter tower multiplicity from 0 to 20.

multiplicity distributions can be quite deceiving. Although they do indeed peak at the (0,0) bin (certainly for the quark and hard gluon structures), a large portion of events have at least a few hits in the detector. This can be seen by comparing the number of events in each POMPYT sample to the number of events in the (0,0) bin only. For example, the central electron W quark structure sample has approximately 100 events in the (0,0) bin, but there are 528 events in the entire sample. Assuming that only events in the (0,0) bin are selected as rapidity gap events (a rather conservative assumption), a rough gap efficiency of $\epsilon = 19\%$ can be calculated. This compares favorably to the $\epsilon = 21 \pm 4\%$ found using the two-dimensional fitting method, confirming that the fit gives a reasonable result.

Table 5.2. The number of events in each Monte Carlo sample are shown for quark pomeron events, hard gluon pomeron events, and soft gluon events.

POMPYT Monte Carlo Sample	Num Events Quark	Num Events Hard Gluon	Num Events Soft Gluon
Central W	528	383	225
Forward W	262	244	384
Z	488	392	111

The soft gluon gap efficiencies were difficult (if not impossible) to determine, and were extremely low when the could be calculated. This becomes understandable upon examination of the multiplicity distributions. In each case (central, forward W or Z), there are two contributing factors to this difficulty: low statistics and the shape of the multiplicity distributions. The soft gluon pomeron is not expected to produce many diffractive W or Z bosons. To first order, they are produced from a quark component in the pomeron. Additionally, these are very massive particles, so the pomeron must carry a significant amount of energy in order to produce a W or Z. The maximum diffractive mass possible is given by: $M_x = \sqrt{\xi s}$. For the typical ξ range (approximately 0.005 to 0.10) expected for diffraction, we have 130

GeV $< M_x <$ 570 GeV. However, the nature of the soft gluon pomeron structure is such that each gluon carries only a small fraction of the pomeron momentum. Therefore, high values of ξ are needed in order to produce diffractive W and Z bosons with a soft gluon pomeron. These effects combine to produce low statistics for this pomeron model. Soft gluon events also tend to populate higher multiplicities than in equivalent distributions for hard gluon or quark events (see Fig. 5.9). The mean of the minimum side calorimeter multiplicity for soft gluon events is twice that for the quark events.

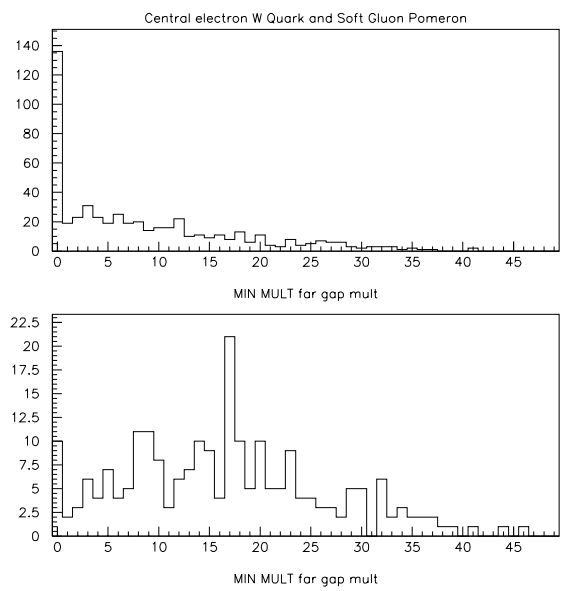

Figure 5.9. Calorimeter multiplicity (x-axis) distributions are shown for central electron W events: quark structure pomeron (top plot) mean number of calorimeter towers above threshold =8.9, and soft gluon structure (bottom) mean = 16.8 towers.

The central electron W gap efficiency is lower than that of the forward electron sample for all three pomeron structures. As the high mass system from the W or Z is moved closer to the rapidity gap region, the percent of events in the (0,0) bin decreases, leading to a decrease in gap efficiency. This is expected since the forward

electron events are farther from the gap, and therefore are less likely to spoil it. The Z gap efficiency is comparable to that of the central electron W sample. This is reasonable considering that every Z event has at least one electron in the central region of the detector.

The central electron events are also typically produced from a pomeron with a higher fraction of the initial proton momentum, a higher ξ. Earlier, diffractive event boost was discussed as the result of an overpowering imbalance in momentum between the pomeron and the proton. This causes diffractive events to be pushed forward in η; however, we have required a sample of events to have a central electron. In order to meet this demand, the pomeron must be able to balance the momentum from the other parton in the event. Therefore, the pomeron carries a higher fraction of the proton momentum. The high mass systems created in such interactions have the potential to ruin more rapidity gaps, so the gap efficiency depends on the ξ of the pomeron. This dependence can be seen in figure 5.10 for the central electron W events. As the pomeron ξ increases, the number of events in the sample increases, but the percentage of events at low multiplicities decreases. Therefore, the gap efficiency decreases with increasing ξ. The forward electron W events show similar behavior (see figure 5.11), although it is less dramatic because most of the forward electron events have a low pomeron ξ. The gap efficiency was also calculated for events with a $\xi_{max} = 0.2$ set at generation, as opposed to the default $\xi_{max} = 0.1$. Table 5.3 shows the gap efficiency results for these events. As expected, the gap efficiency is lower for all samples (W and Z) at higher ξ.

Events with rapidity gaps occur through color singlet exchange processes. Pomeron exchange is one such process, but it is not the only possibility. To facilitate study of alternative color single exchange processes, POMPYT has the capability to generate pion exchange events. At this point, only π^0 and π^+ exchange have been implement-

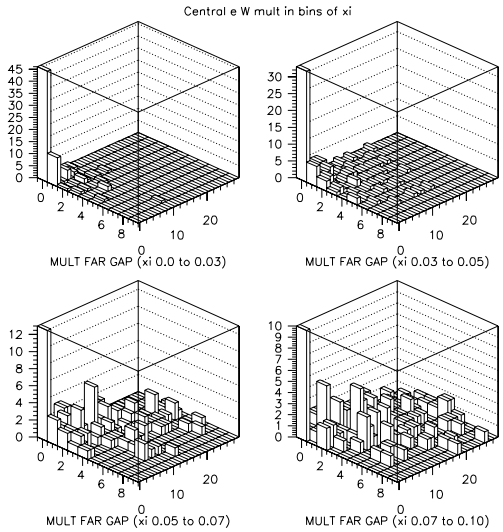

Figure 5.10. Multiplicity distributions for central electron W events in bins of ξ (the fraction of the initial proton momentum carried by the pomeron). As ξ increases (top left $\rightarrow$ top right $\rightarrow$ bottom left $\rightarrow$ bottom right), a lower percentage of events are at low multiplicities, and the gap efficiency decreases. For each distribution, the LevelØ multiplicity runs from 0 to 10 and the calorimeter tower multiplicity from 0 to 30.

Table 5.3. Gap efficiencies for several structure function models of diffractive W and Z boson production using events generated with the POMPYT Monte Carlo package. The maximum possible ξ value was limited to: $\xi_{max} = 0.2$ at generation.

Pomeron Structure Function	**Sample**	**Gap Efficiency**
QUARK		
	central electron W	11 $\pm$ 2%
	forward electron W	27 $\pm$ 7%
	Z (CC-CC, CC-EC electrons)	15 $\pm$ 3%
HARD GLUON		
	central electron W	15 $\pm$ 4%
	forward electron W	22 $\pm$ 6%
	Z (CC-CC, CC-EC electrons)	17 $\pm$ 4%

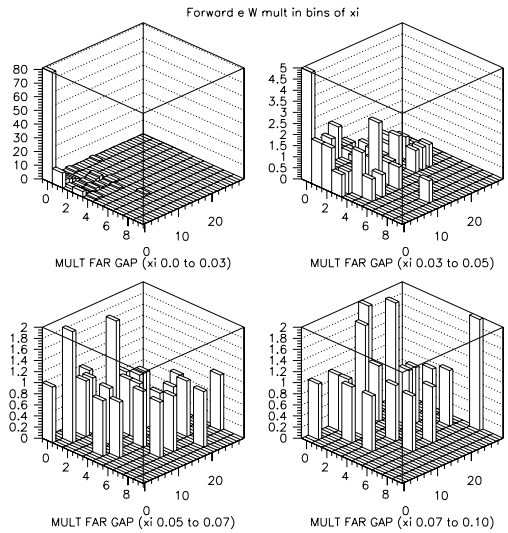

Figure 5.11. Multiplicity distributions for forward electron W events in bins of ξ (the fraction of the initial proton momentum carried by the pomeron). As ξ increases (top left $\rightarrow$ top right $\rightarrow$ bottom left $\rightarrow$ bottom right), a lower percentage of events are at low multiplicities, and the gap efficiency decreases.

ed where the proton 'emits' a pion instead of a pomeron. Of course, if the proton 'emits' a π^+, charge must be conserved, and we have $p \rightarrow \pi^+ n$. Factorization is applied to this type of exchange as it is for pomeron exchange. Pion flux factors are used instead of the pomeron flux factors, and the pion parton densities are those available through PYTHIA [49]. These events are processed just like the pomeron exchange events, leading to the same type of multiplicity distribution possibilities. The gap efficiencies for π^0 and π^+ exchange are shown in Table 5.4, and are extremely small with large errors for each W or Z sample. As in the soft gluon case, these gap efficiencies are very difficult to determine, but in this case it is an exercise in futility. It will be shown later, that the fraction of diffractive W and Z production through pion exchange is miniscule. (See Section 5.3 for the Monte Carlo diffractive fraction results.) Even if 100% of these events could be detected ($\epsilon_{gap} = 100\%$),

these processes would not come close to matching the fraction of diffractive W and Z bosons production in data.

Table 5.4. Gap efficiencies for diffractive W and Z boson production through pion exchange. Both π^0 and π^+ exchange are modeled using POMPYT.

π^0 **Exchange Sample**	**Gap Efficiency**
central electron W	7 $\pm$ 2%
forward electron W	3 $\pm$ 2%
Z (CC-CC, CC-EC electrons)	5 $\pm$ 2%
π^+ **Exchange Sample**	**Gap Efficiency**
central electron W	5 $\pm$ 2%
forward electron W	2 $\pm$ 5%
Z (CC-CC, CC-EC electrons)	5 $\pm$ 2%

5.3 Monte Carlo Gap Fraction

Now that we have the gap efficiency for each pomeron model, we can calculate the diffractive W and Z fraction predicted by the Monte Carlo. First we will determine the diffractive W and Z fraction for each pomeron model independent of any detection efficiency. Then, these will be combined with the appropriate gap efficiencies to determine the visible fraction of diffractive W and Z bosons. This final $f_{visible}$ can then be compared directly to the data fraction regardless of the pomeron model involved.

The diffractive W and Z fraction depends a great deal on the pomeron structure; therefore, calculations are done for the quark, hard gluon, and soft gluon structure functions. The Monte Carlo fraction is given by the cross section measured in POMPYT divided by the cross section from PYTHIA. Since only the antiproton is allowed to diffract, the POMPYT cross section must be doubled for this calculation. Table 5.5 shows the predicted diffractive W and Z fractions after full detector

simulation. As expected, the quark pomeron model produces by far the highest fraction (on the order of 20%) of diffractive W and Z bosons. Additionally, the three Monte Carlo samples (central W, forward W, and Z) predict very similar percentages at this point. The hard gluon pomeron model produces a much lower fraction of diffractive to all W and Z bosons. With this model, a diffractive fraction of approximately (0.5%) is predicted by POMPYT. Finally, the soft gluon pomeron model is considered. Again, as expected, this model predicts the smallest fraction of diffractively produced W and Z bosons. Table 5.6 shows the predicted diffractive W and Z production fraction for π^0 and π^+ exchange rather than pomeron exchange. Whereas the pomeron models either predict a fairly significant diffractive W or Z signal, or at least a signal fraction on the order of 0.5%, the pion exchange essentially predicts no diffractive events. The predicted MC fractions were also calculated for events with a $\xi_{max} = 0.2$ set at generation, and are shown in Table 5.7. The fraction increases with increased ξ because it becomes easier to produce the massive W and Z systems. This characteristic is reflected in the results for all three pomeron structures.

In order to compare to data, the gap efficiency must be folded into the diffractive fraction calculations since $f_{visible} = f_{true} \times \epsilon_{gap}$. Until this point, we have only been looking at f_{true} in the Monte Carlo. As a reminder, the fractions of diffractive to all W and Z bosons produced in data are listed in Table 5.8. The final Monte Carlo gap fractions are shown in Table 5.9. It is perhaps easier to think of the Monte Carlo fraction without any gap efficiency correction as a *diffractive* fraction, whereas we compare the Monte Carlo *gap* fraction to data. Note that we use the Monte Carlo events generated with $\xi_{max} = 0.1$ to predict the gap fraction for comparison to data. This is done because the ξ distributions in POMPYT show that diffractive W and Z rapidity gap events are produced with ξ values below this limit(See Section 5.4).

Table 5.5. Predicted fractions, (POMPYT/PYTHIA), of diffractively produced W and Z events are shown after full detector simulation for quark, hard gluon, and soft gluon pomeron models. The maximum possible ξ value was limited to: $\xi_{max} = 0.1$ at generation. The gap efficiency has NOT been taken into account.

Pomeron Structure Function	**Sample**	**Monte Carlo Diffractive Fraction**
QUARK	central electron W	$20 \pm 1\%$
	forward electron W	$21 \pm 2\%$
	Z (CC-CC, CC-EC electrons)	$17 \pm 1\%$
HARD GLUON	central electron W	$0.45 \pm 0.02\%$
	forward electron W	$0.61 \pm 0.04\%$
	Z (CC-CC, CC-EC electrons)	$0.42 \pm 0.02\%$
SOFT GLUON	central electron W	$0.10 \pm 0.01\%$
	forward electron W	$0.38 \pm 0.02\%$
	Z (CC-CC, CC-EC electrons)	$0.09 \pm 0.01\%$

Table 5.6. Predicted fractions, (POMPYT/PYTHIA), of diffractively produced W and Z are shown after full detector simulation for π^0 and π^+ exchange. The gap efficiency has NOT been taken into account.

π^0 Exchange Sample	**MC Diffractive Fraction**
central electron W	$1.5 \times 10^{-32} \pm 0.1 \times 10^{-32}\%$
forward electron W	$1.9 \times 10^{-32} \pm 0.2 \times 10^{-32}\%$
Z (CC-CC, CC-EC electrons)	$1.5 \times 10^{-31} \pm 0.1 \times 10^{-31}\%$
π^+ Exchange Sample	**MC Diffractive Fraction**
central electron W	$3.2 \times 10^{-31} \pm 0.2 \times 10^{-31}\%$
forward electron W	$3.6 \times 10^{-31} \pm 0.3 \times 10^{-31}\%$
Z (CC-CC, CC-EC electrons)	$2.1 \times 10^{-31} \pm 0.1 \times 10^{-31}\%$

Table 5.7. Predicted fractions, (POMPYT/PYTHIA), of diffractively produced W and Z events are shown after full detector simulation for quark, hard gluon, and soft gluon pomeron models. The maximum possible ξ value was limited to: $\xi_{max} = 0.2$ at generation. The gap efficiency has NOT been taken into account.

Pomeron Structure Function	**Sample**	**Monte Carlo Diffractive Fraction**
QUARK	central electron W	33 $\pm$ 2%
	forward electron W	27 $\pm$ 3%
	Z (CC-CC, CC-EC electrons)	34 $\pm$ 2%
HARD GLUON	central electron W	1.1 $\pm$ 0.1%
	forward electron W	0.9 $\pm$ 0.1%
	Z (CC-CC, CC-EC electrons)	1.1 $\pm$ 0.1%
SOFT GLUON	central electron W	0.47 $\pm$ 0.03%
	forward electron W	1.0 $\pm$ 0.08%
	Z (CC-CC, CC-EC electrons)	0.42 $\pm$ 0.03%

Table 5.8. The fraction of diffractive to all W bosons produced in data is shown for both central electron Ws and forward electron Ws. The analogous fraction is also reported for diffractively produced Z bosons.

DATA Sample	**Final DATA Gap Fraction**
central electron W	$1.08 \pm^{0.21}_{0.19}$ %
forward electron W	$0.64 \pm^{0.19}_{0.16}$ %
Z (CC-CC, CC-EC electrons)	$1.38 \pm^{0.62}_{0.48}$ %

Table 5.9. Final predicted gap fractions, (POMPYT/PYTHIA), of diffractively produced W and Z events are shown after full detector simulation for quark, hard gluon, and soft gluon pomeron models. The maximum possible ξ value was limited to: $\xi_{max} = 0.1$ at generation. The gap efficiency HAS been taken into account.

Pomeron Structure Function	**Sample**	**Final Monte Carlo Gap Fraction**
QUARK	central electron W	4.1 $\pm$ 0.8%
	forward electron W	7.2 $\pm$ 1.3%
	Z (CC-CC, CC-EC electrons)	3.5 $\pm$ 0.7%
HARD GLUON	central electron W	0.15 $\pm$ 0.02%
	forward electron W	0.25 $\pm$ 0.04%
	Z (CC-CC, CC-EC electrons)	0.14 $\pm$ 0.02%
SOFT GLUON	central electron W	0.003 $\pm$ 0.001%
	forward electron W	0.02 $\pm$ 0.004%
	Z (CC-CC, CC-EC electrons)	0.004 $\pm$ 0.007%

We have now reached a significant point in this analysis. We know the W and Z gap fractions in data, *and* we have the predicted gap fractions in Monte Carlo for several pomeron structures. At this point we can determine whether or not POMPYT predicts what is seen in data by comparing the results in Tables 5.8 and 5.9. The soft gluon pomeron structure function predicts an extremely low gap fraction which does not describe the data. We can take the central electron W sample as a concrete example: the soft gluon pomeron predicts a gap fraction of $0.003 \pm 0.001\%$ compared to $1.08 \pm^{0.21}_{0.19}\%$ in data. This is lower than the observed fraction for data by a factor of 1000. We can eliminate the POMPYT soft gluon as the source of the rapidity gap events seen in data.

We next examine the possibility that a quark pomeron is the source of the diffractive W and Z events. While this model *does* produce a significant number of rapidity gap events, the POMPYT gap fractions are 4 to 11 times higher than those observed in data for the W samples. Additionally, the Z data is not described by a quark pomeron in POMPYT. The hard quark prediction is 2.5 times higher than that observed for the Z data: $3.5 \pm 0.7\%$ in MC compared to $1.38 \pm^{0.62}_{0.48}\%$ in data.

Finally, we can compare the data gap fractions to those from a hard gluon pomeron. According to Bruni and Ingleman [19], this structure function is expected to produce a lower percentage of diffractive W and Z events compared to the quark pomeron. (See Section 2.5.) In fact, the hard gluon fractions from POMPYT *are* much lower than those predicted for the quark pomeron; however, they are also consistently lower than the data fractions (by a factor of 3-10 depending on the sample).

These results are consistent with previous diffractive measurements, which show a normalization problem compared to POMPYT. Recently the rapidity gap fraction for hard single diffraction with jets was measure in $p\overline{p}$ collisions, and none of the

simple POMPYT models described the data well citekristal-thesis. A combination of hard gluons ($\sim 25\%$) and soft gluons ($\sim 75\%$) was needed in order to reproduce the data results. In a similar fashion, we can compare the predictions from a pomeron with both a quark and a hard gluon component. For example, a pomeron with a hard-quark fraction of 0.25 and a hard gluon fraction of 0.75 approximately matches the central electron W data fraction. However, if the pomeron is composed largely of gluons, one would expect a high percentage of the diffractive W events to contain a jet in the final state. Although we do see diffractive $W + jet$ events, they do not dominate the sample (see Table 4.17.)

In addition to the difference in normalization, the Monte Carlo shows a very different dependence of the fraction on rapidity. The W data has a higher fraction in the central region than the forward (see Table 5.8), whereas the Monte Carlo rapidity dependence is the opposite (see Table 5.9). Both the quark and hard gluon pomeron exhibit this η dependence; however, for the quark structure this is entirely due to the different gap efficiencies in the central and forward samples. Incidentally, the soft gluon pomeron also predicts the same η dependence for the fraction as the hard gluon and quark structures.

5.4 ξ Distribution

As we have seen, diffractive event characteristics change depending on the momentum of the pomeron involved. This momentum is given by $\xi = 1 - x_p$, where x_p is the momentum fraction of the outgoing diffracted proton. In addition to providing diffractive W and Z gap fraction predictions, POMPYT can also be used to study the ξ distribution for different types of events. Central events are not boosted forward, implying that they were produced from a pomeron with a higher ξ than forward events. Additionally, the multiplicity distribution changes depending on the ξ of the event. The high diffractive masses produced at increased ξ are more

likely to ruin a rapidity gap in a diffractive event. It is easy to see that different types of diffractive events probe different states of the pomeron. In order to fully understand the events we see in data, it makes sense to learn more about this aspect of diffractive scattering.

Using POMPYT, we have the capability to look at the ξ distributions for different samples of diffractive W and Z events. Figure 5.12 shows the ξ distribution for quark pomeron diffractive W events with electron $E_T > 25$ GeV (solid line) at generation level. The dashed line is the ξ distribution for central electron events, and the dotted line represents forward electron events. Events from the original sample (solid line) which fall into poorly instrumented regions in the detector are excluded from the central and forward electron distributions. As a result, the sum of the two does not equal the original distribution.

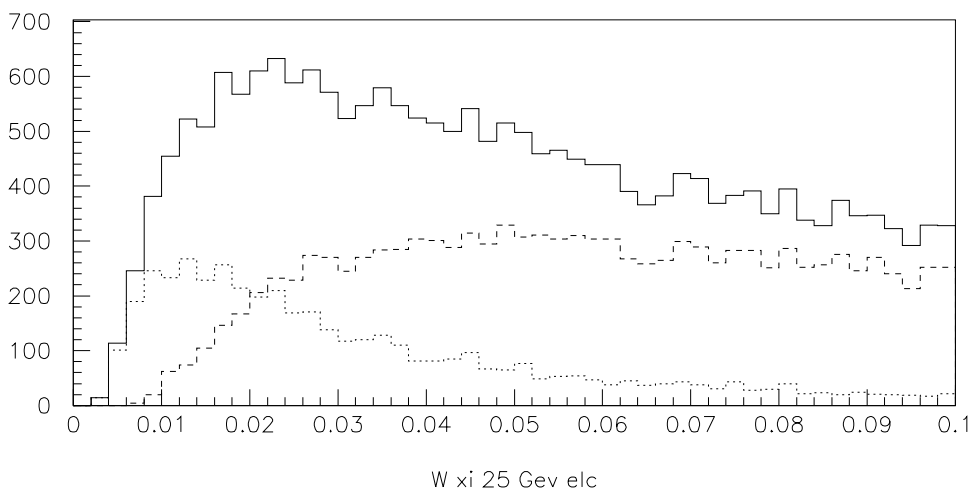

Figure 5.12. The ξ distribution is shown for quark pomeron W events with electron $E_T > 25$ GeV (solid line). The dashed line is the ξ distribution for central electron events, and the dotted line represents forward electron events. The central electron events probe a higher ξ region than the forward events.

The ξ probed in central electron events is higher than that for the forward events which peak much closer to zero. The central electron events have $\xi_{MEAN} =$

0.06, compared to $\xi_{MEAN} = 0.03$ for the forward electron events. As expected, the pomeron carries a higher fraction of the initial proton momentum for events with a central electron. The ξ distribution for quark pomeron Z events is shown in figure 5.13. Again, we can see that the more central events (those with CC-CC electrons) involve a pomeron with a higher ξ. The same general effect is seen for diffractively produced dijets, where jets with significant E_T are required [59]. The forward dijet ξ distribution peaks much closer to zero than the central dijet distribution.

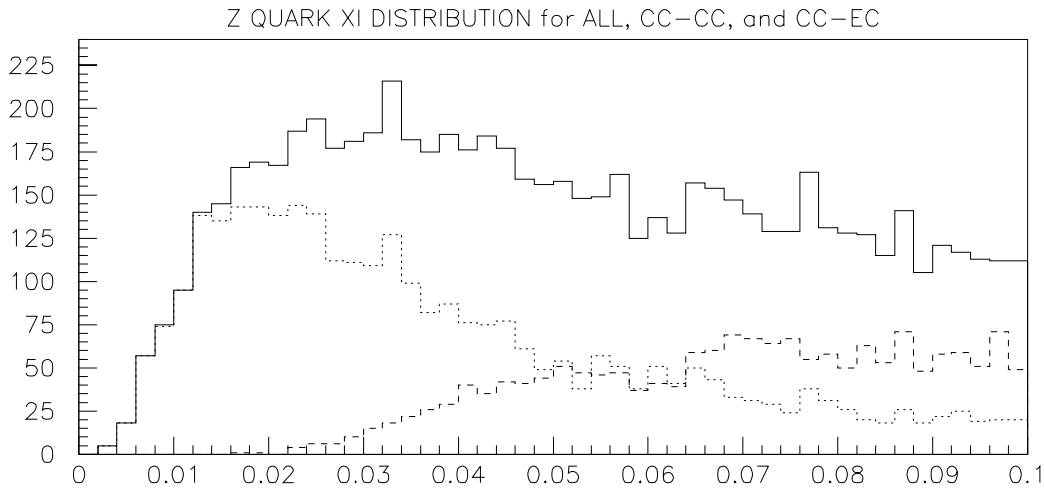

Figure 5.13. The ξ distribution is shown for quark pomeron Z events with electron $E_T > 25$ GeV (solid line). The dashed line is the ξ distribution for CC-CC electron events, and the dotted line represents CC-EC electron events. The CC-CC electron events probe a higher ξ region as did the central electron W events.

So far, we do not have a complete picture of the ξ distribution for events that we are likely to identify as diffractive. The events we are looking for require a rapidity gap, and this additional demand will affect the ξ region probed in the data. Figures 5.14 and 5.15 show how the ξ distribution changes for central and forward quark pomeron W events when a gap is required. Many of the high mass states have been excluded. Figure 5.16 shows the ξ distribution for CC-CC and CC-EC

Z events both with and without a far gap. These ξ distributions confirm that the POMPYT events used in the gap fraction calculations were appropriate. We can see that very few events with ξ near 0.1 remain in the sample once when we look at rapidity gap events. Therefore, it is unlikely that we need to calculate the gap fractions using events generated with $\xi_{max} = 0.2$. We therefore keep the gap fraction results for events generated with $\xi_{max} = 0.1$ as our final Monte Carlo predictions.

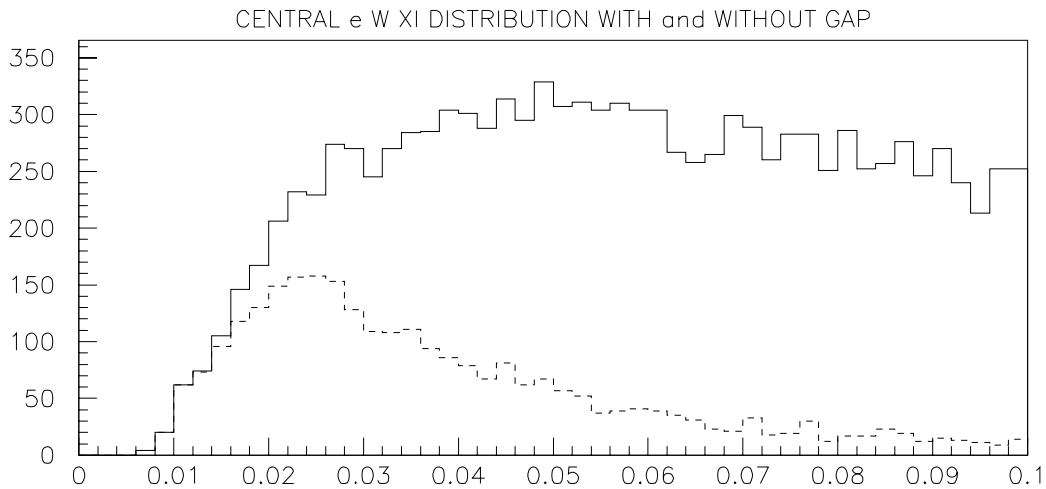

Figure 5.14. The ξ distribution for quark pomeron W events is shown for central electron events with no rapidity gap required (solid line) and for events with a far gap (dashed line). Many of the high mass states have been excluded by demanding a rapidity gap. The mean of the distribution drops from ($\xi_{MEAN} = 0.06$) to ($\xi_{MEAN} = 0.04$) when a far gap is required.

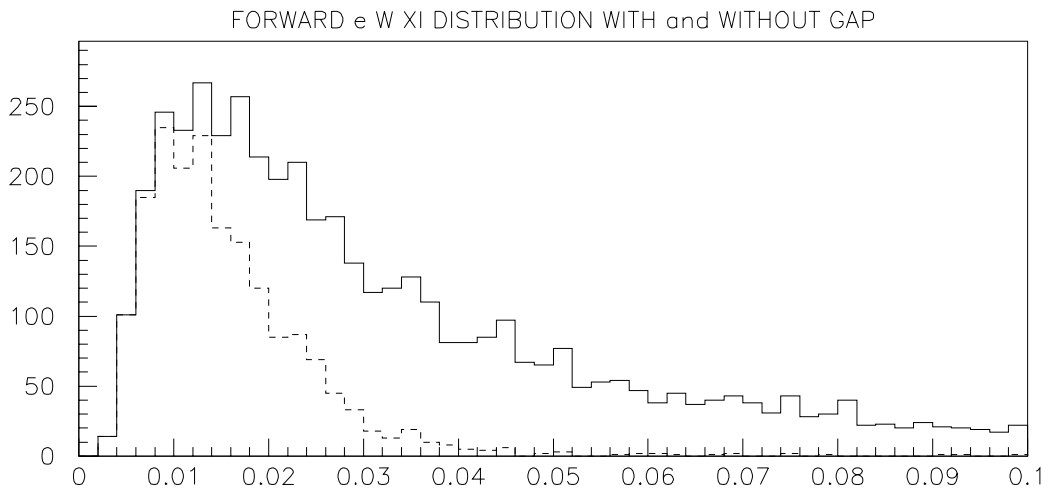

Figure 5.15. The ξ distribution for quark pomeron W events is shown for forward electron events with no rapidity gap required (solid line) and for events with a far gap (dashed line). Again, the higher mass states have been excluded by demanding a rapidity gap. The mean of the distribution drops from ($\xi_{MEAN} = 0.03$) to ($\xi_{MEAN} = 0.02$) when a far gap is required.

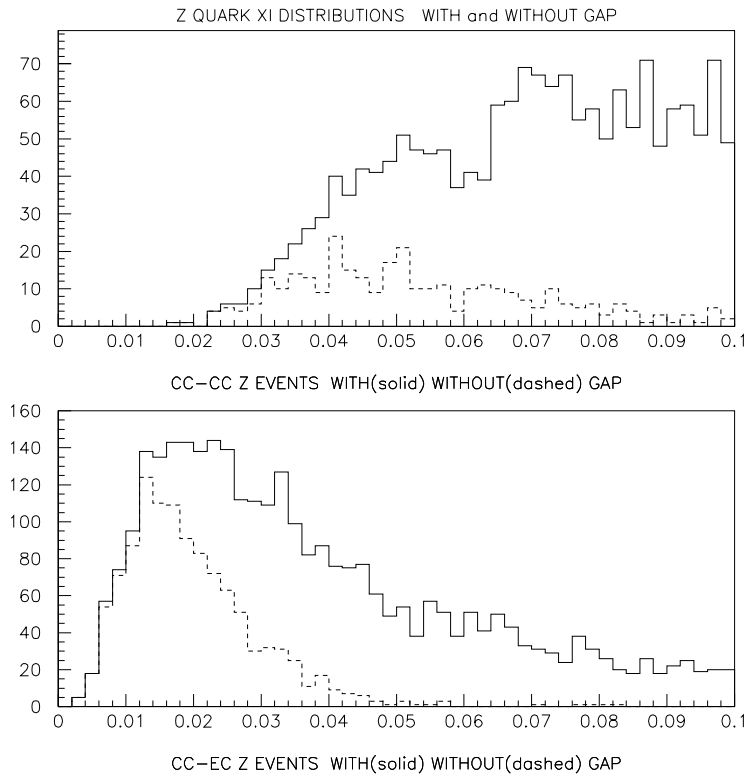

Figure 5.16. The ξ distribution for quark pomeron Z events is shown for CC-CC (top plot) electron events with no rapidity gap required (solid line) and for events with a far gap (dashed line). The distribution is shown for CC-EC events (bottom plot) without (solid) and with a gap (dashed line). Again, many of the higher mass states have been excluded by demanding a rapidity gap.

CHAPTER 6

CONCLUSION

We have observed a clear diffractive W signal for both central and forward electron $W \rightarrow e\nu$ events in $p\overline{p}$ collisions at $\sqrt{s} = 1.8$ TeV. We have measured the signal fractions of diffractive W to all W events for the central electron W events, the forward electron W events, and the combined sample. These signal fractions are shown in Table 6.1. We also measure a rapidity dependence for diffractive W production which can be seen in Table 6.2. The signal fraction measured for events with $0.5 \leq |\eta_{electron}| < 1.1$ is much larger than that for events with very central ($|\eta| < 0.5$) or forward electron Ws.

We also report the first observation of diffractively produced Z bosons in a sample of $Z \rightarrow e^+e^-$ events in $p\overline{p}$ collisions at $\sqrt{s} = 1.8$ TeV. We have measured the fraction of diffractive Z to all Z for this sample to be $1.38 \ \pm^{0.62}_{0.48}$ % (see Table 6.1).

The gap fractions for both W and Z data can be compared to those predicted by POMPYT for several pomeron structure functions. Table 6.3 shows the gap fractions for data, a hard quark pomeron structure, and a hard gluon pomeron structure. The soft gluon pomeron structure function has been eliminated as the source for diffractive W and Z production due to the extremely low signal fractions predicted. For example, the central electron W diffractive rate is predicted to be $0.003 \pm 0.001\%$ for a soft gluon pomeron. This is lower than the observed fraction for data by a factor of 1000. We next examine the possibility that a quark pomeron is the source of the diffractive W and Z events. The hard quark structure pomeron model from

Table 6.1. Measured gap fractions for Ws and Zs at 1800 GeV center-of-mass energy.

$W \to e\nu$	**Measured Gap Fraction**
central, $\lvert\eta\rvert < 1.1$	$1.08 \ \pm^{0.21}_{0.19}$ %
forward, $1.5 < \lvert\eta\rvert < 2.5$	$0.64 \ \pm^{0.19}_{0.16}$ %
total $W \to e\nu$ **sample**	$0.89 \ \pm^{0.20}_{0.19}$ %
$Z \to e^+e^-$	**Measured Gap Fraction**
$Z \to e^+e^-$ **sample CC-CC, CC-EC**	$1.38 \ \pm^{0.62}_{0.48}$ %

Table 6.2. Rapidity (η) dependence of the measured gap fractions for W's at 1800 GeV center-of-mass energy.

$W \to e\nu$ **sample**	**Measured Gap Fraction as a function of** η
$\lvert\eta_{electron}\rvert < 0.5$	$0.58 \ \pm^{0.28}_{0.20}$ %
$0.5 \leq \lvert\eta_{electron}\rvert < 1.1$	$1.48 \ \pm^{0.30}_{0.26}$ %
$1.5 < \lvert\eta_{electron}\rvert < 2.5$	$0.64 \ \pm^{0.19}_{0.16}$ %

POMPYT predicts results 4 to 11 times higher than that observed in data for the W samples. The hard quark prediction is 2.5 times higher than that observed for the Z data. These results are consistent with previous diffractive measurements, which show a normalization problem compared to POMPYT, especially considering that previous results indicate that the pomeron is less than 50% quarks [60]. We can also compare the data rates to those from a hard gluon pomeron. In this case, the hard gluon rate is consistently lower than that in data (by a factor of 3-10 depending on the sample). These normalization problems could perhaps be corrected by a pomeron with both a quark and a hard gluon component. For example, a pomeron with a hard-quark fraction of 0.25 and a hard gluon fraction of 0.75 approximately matches the central electron W data fraction. However, if the pomeron is composed largely of gluons, one would expect a high percentage of the diffractive W events to contain a jet in the final state. Although we do see diffractive $W + jet$ events, they do not dominate the sample.

In addition to the difference in normalization, the Monte Carlo shows a very different dependence of the fraction on rapidity (η). The central electron W data sample has a higher gap fraction than the forward electron W sample. On the other hand, the Monte Carlo gap fraction is *lower* for the central sample than for the forward sample. Both the quark and hard gluon pomeron exhibit this η dependence; however, for the quark structure this is entirely due to the different gap efficiencies in the central and forward samples. These problems with fraction normalization and dependence on η imply that the current POMPYT model of diffraction does not describe the diffractive W or Z data well for a hard quark, hard gluon, or soft gluon pomeron.

It is also useful to compare the fractions of observable diffractive W and Z events to the equivalent diffractive dijet fractions. Eventually, these results will be

Table 6.3. A comparison of diffractive W and Z data gap fractions to those predicted by POMPYT for a hard quark and hard gluon pomeron.

Sample	**Data Gap Fraction**	**Quark MC Gap Fraction**	**Hard Gluon MC Gap Fraction**
central electron W	$1.08 \ \pm^{0.21}_{0.19}$ %	$4.1 \ \pm 0.8\%$	$0.15 \ \pm 0.02\%$
forward electron W	$0.64 \ \pm^{0.19}_{0.16}$ %	$7.2 \ \pm 1.3\%$	$0.25 \ \pm 0.04\%$
Z (CC-CC,CC-EC)	$1.38 \ \pm^{0.62}_{0.48}$ %	$3.5 \ \pm 0.7\%$	$0.14 \ \pm 0.02\%$

combined with those from diffractive photon production and double diffractive dijet production. This will provide a complete picture of diffraction in $p\overline{p}$ interactions.

The observable gap fractions for Z and central electron W boson events are higher than that for diffractive dijets, but are of a similar order (see Table 6.4). In other words, we don't expect to see 1% of W bosons produced diffractively compared to 50% of dijet events produced diffractively. In reality, the fraction of dijets produced diffractively at 1800 GeV is $R_{jjcentral} = 0.20 \pm^{0.08}_{0.05}$ % for central jets and $R_{jjforward} = 0.64 \pm 0.05\%$ for forward jets [48]. Unlike the central fraction, the gap fraction for the forward electron W sample is equal within error bars to that found for the forward dijet event sample. We can also see that where the diffractive W gap fraction *decreases* with increasing η, the diffractive dijet fraction *increases*.

So far, the fractions reported for all samples (W, Z, and dijet) have been those for the *observable* diffractive events (i.e. those with rapidity gaps). If we consider the Ingelman and Schlein pomeron model, we must correct the *observed* fractions by the gap efficiency in order to determine the *actual* diffractive fractions in data. This is the reverse of the process used to bring all Monte Carlo models to the same level for comparison to data (See Section 5.3.) We assume the gap efficiencies in POMPYT are correct, and use them to correct the data gap fractions. The W, Z,

Table 6.4. A comparison of diffractive W and Z data gap fractions to diffractive dijet data gap fractions.

W,Z Sample	**Data Gap Fraction**	**Dijet Data Sample**	**Dijet Gap Fraction**
central electron W	$1.08 \ \pm^{0.21}_{0.19}$ %	Central Jets	$0.20 \ \pm^{0.08}_{0.05}$ %
forward electron W	$0.64 \ \pm^{0.19}_{0.16}$ %	Forward Jets	$0.64 \ \pm 0.05$%
Z (CC-CC,CC-EC)	$1.38 \ \pm^{0.62}_{0.48}$ %		

and dijet data fractions corrected in this manner using the quark pomeron and hard gluon pomeron gap efficiencies are shown in Table 6.6. After this is done, the *total* diffractive W and Z signal fractions are around 5-6% which could be much higher than the dijet fraction. As one might imagine, this final data diffractive fraction depends highly on the true pomeron structure, since the gap efficiency also depends on this structure.

It is difficult to draw any definite conclusions from a comparison at this level between the W and Z diffractive fractions and the dijet diffractive fraction. Up to this point, we have adjusted the Monte Carlo to compare with data, because we do not know which pomeron structure best describes the data. For the same reason we prefer to simply report the observable gap fraction in data. The fractions listed in Table 6.6 have been corrected with only the quark or hard gluon gap efficiency. The dijet quark and hard gluon gap efficiencies for forward jets are higher than those for W and Z production. This generally brings the diffractive fractions for the two types of events closer together, but it is a small effect. However, there may be a soft gluon component to the pomeron which has a much lower gap efficiency (4 ± 3% for the central jet events and 23 ± 5% the forward jet soft gluon events) [48]. If the dijet gap fraction is converted to the dijet diffractive fraction using the soft gluon

gap efficiency, the overall rates will be much higher. Additionally, there have been recent attempts to describe rapidity gap events using soft color rearrangement (see Section 2.6). In this type of model, gaps are produced independent of the hard process, and it is not clear that there is a gap efficiency. For a soft color model the rapidity gap fractions for W, Z, and dijet production would stand as they are. Furthur theoretical work will be needed to fully understand these diffractive results.

Table 6.5. The diffractive W, Z, and dijet gap fractions [48] measured in data are listed with the associated gap efficiencies for a quark pomeron and hard gluon pomeron.

DATA Sample	**Measured Data Gap Fraction**	**Gap Efficiency Quark**	**Gap Efficiency Hard Gluon**
central electron W	$1.08 \pm^{0.21}_{0.19}$ %	$21 \pm 4\%$	$33 \pm 5\%$
forward electron W	$0.64 \pm^{0.19}_{0.16}$ %	$35 \pm 6\%$	$42 \pm 6\%$
Z (CC-CC,CC-EC)	$1.38 \pm^{0.62}_{0.48}$ %	$21 \pm 4\%$	$33 \pm 5\%$
Dijet central jets	$0.20 \pm^{0.08}_{0.05}$ %	$18 \pm 6\%$	$40 \pm 6\%$
Dijet forward jets	$0.64 \pm 0.05\%$	$58 \pm 9\%$	$74 \pm 11\%$

Table 6.6. The diffractive W, Z, and dijet data gap fractions are corrected back to the diffractive fraction using the gap efficiency for a quark pomeron and a hard gluon pomeron.

DATA Sample	**Data Gap Fraction**	**Corrected Using Quark Gap Eff**	**Corrected Using Hard Gluon Gap Eff**
central electron W	$1.08 \ \pm^{0.21}_{0.19}$ %	$\sim 5.1\%$	$\sim 3.3\%$
forward electron W	$0.64 \ \pm^{0.19}_{0.16}$ %	$\sim 1.8\%$	$\sim 1.5\%$
Z (CC-CC,CC-EC)	$1.38 \ \pm^{0.62}_{0.48}$ %	$\sim 6.6\%$	$\sim 4.2\%$
Dijet central jets	$0.20 \ \pm^{0.08}_{0.05}$ %	$\sim 1.1\%$	$\sim 0.5\%$
Dijet forward jets	$0.64 \ \pm 0.05\%$	$\sim 1.1\%$	$\sim 0.9\%$

APPENDIX A

MULTIPLICITY FITS

Signals above underlying multiplicity distributions in the diffractive W and Z analysis are extracted by application of a two dimensional fit to the calorimeter (n_{CAL}) and LevelØ ($n_{L\emptyset}$) multiplicities. Sample multiplicity distributions are shown in Fig. A.1. The upper two plots show a calorimeter versus LØ multiplicity plot from the 1800 GeV central electron diffractive W data set. In the bottom panels the projections onto the LØ and calorimeter axes are shown.

Earlier versions of the analyses fit only to the one dimensional n_{CAL} distribution. A 'leading edge' fit was used to fit n_{CAL} in the region between the low multiplicity peak and the most probable value of the multiplicity distribution. The fit was then extrapolated to zero multiplicity and used as a background estimate for extraction of the diffractive signal. This proved unsatisfactory in some cases, due to large fitting errors. Additionally, the extrapolation of the fit under the peak at zero multiplicity could show large variations based on the functional form selected to model the background. This motivated the move to include more multiplicity information by fitting the 2-D distributions and the precision of the fits was improved. Additionally, the background distribution is nearly flat, making signal extraction significantly less dependent on the choice of functional form used to fit the background.

In the 2-D fits both signal and background are fit simultaneously with the fol-

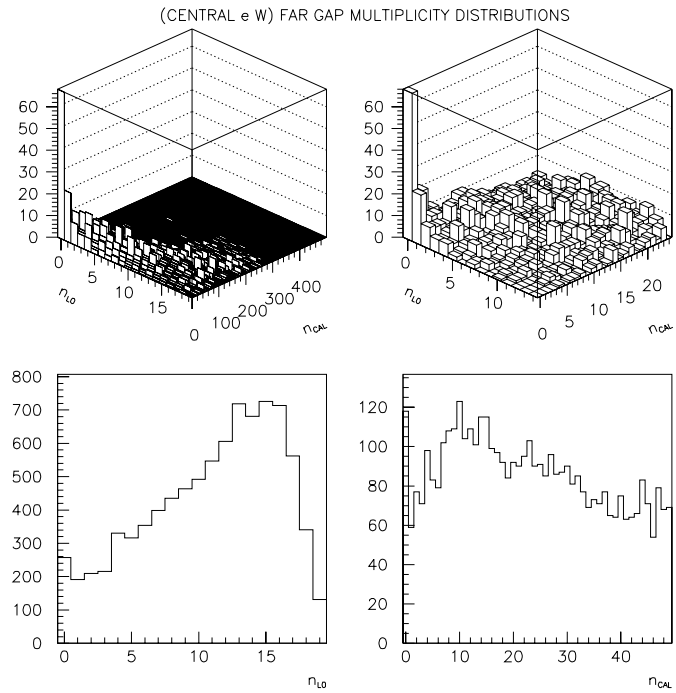

Figure A.1. The multiplicity of LØ and calorimeter towers above threshold in the minimum multiplicity far gap region for the central electron W sample is shown (top left). The top-right plot is a close-up of the region near (0,0). The bottom left plot shows the LevelØ multiplicity distribution and the bottom right shows the calorimeter multiplicity distribution.

lowing function:

$$B_0 + B_1 \cdot \int_{x^i}^{x^f} x dx + B_2 \cdot \int_{y^i}^{y^f} y dy + B_3 \int_{x^i}^{x^f} \int_{y^i}^{y^f} xy dx dy + \frac{S_0}{S_1 \cdot S_2} \cdot \int_{x^i}^{x^f} \int_{y^i}^{y^f} exp(-x/S_1 - y/S_2) dx dy$$

The B_i's are background fit parameters and the S_i's are signal fit parameters. The integrations are meant to illustrate that the function is integrated over each bin for comparison to the data. More complex background functions including high powers in 'x' and 'y' were explored. One such fit is referred to as the "six parameter fit" because the background shape is of the form: $B_0 + B_1 x + B_2 y + B_3 xy + B_4 x^2 + B_5 y^2$.

However, due to the relative flatness of the background distribution, these more complex functions offered no significant improvements in the quality of the fits.

The fit proceeds in two steps. First a region around the signal peak is masked out (typically 2 bins in $n_{L\emptyset}$ by 3 bins in n_{CAL}) and a background only fit is applied to the background region. Then all parameters in the fit are freed and a signal + background fit is applied to the distribution. The parameters are found using a binned maximum likelihood fit.

It is necessary to determine the upper limits on the fit for the background region. In some sense we still apply a 'leading edge' fit, because we do not expect any useful background information to come from the very high multiplicity regions, far removed from the signal peak. Also, fitting over large multiplicity ranges greatly complicates the shape of the background function and can cause large biases in the background extraction if the shape is being strongly constrained by bins located far from the signal region. For the diffractive W and Z analysis, the calorimeter upper fit limit is near but not beyond the color exchange peak around $n_{CAL} = 12$.(see Figure A.1.) The LØ limit was chosen to be before the LØ multiplicity peak to maximize the information obtained from LØwhile remaining within the chosen n_{CAL} region. As an example, a fit will be done using upper limits in ($n_{L\emptyset}$,n_{CAL}) = (7,11).

The result of a fit to the central electron W data is shown in Fig. A.2. The top plots show the data and the fit (ranges are set to show the fit region). The middle two plots show the background and signal fits. The bottom plots show the fit residuals in a lego plot and the fractional residuals in histogram form.

The signal is extracted directly from S_0 which represents the number of signal events in the sample (in this case $S_0 = 88$). The fractional signal is then S_0 divided by the total number of events (specifically, 88/8745) . The error on the signal is determined from a MINOS error analysis. The signal error (σ_{S_0}) reflects the

uncertainty in the background fit as well as uncertainty in the signal normalization due to signal statistics. Here the signal fraction = 1.00 $\pm$ 0.19%.

A.1 Dependence of Signal on $n_{L\emptyset}$ and n_{CAL} Ranges

For certain samples, namely those with sufficiently large statistics, the diffractive signal shows little dependence on the range of bins selected for the background fit. For example, if we refit the 1800 GeV hard diffraction with jets sample a number of times choosing different background regions around our original choice, we optain the result shown in Fig.A.3. The top plot shows the variation of the diffractive jet signal using different ranges for the background fit. The bands show the parabolic errors reported from MINUIT and the error bars with horizontal lines show the MINOS errors (NOTE: MINOS errors are not always calculable by the algorithms in MINUIT). Points marked with a star have a $\chi^2/d.o.f.$ with a likelihood of better than 1%.

Depending on which sample is fitted, or on the electron cuts imposed, we may find that a smaller surviving event sample shows more sensitivity to the choice of the fit range. See for example Fig. A.4 which shows a test of fit ranges applied to the central electron W sample. Due to the possible dependence of the signal on the fit range we adopt the following procedure to determine the signal in for each sample:

- a number of fits are performed around a nominal background range
- since fits with at least one calculable MINOS error tend to have better convergence than fits with no MINOS errors, we obtain a weighted average of the fits with at least one MINOS error to find the mean signal value. See Fig. A.4 bottom left.

- we include an error on the mean signal equal to the RMS scatter of the signals used to calculate the average. This is negligible for larger data samples, such as those used in the single diffractive dijet analysis. See Fig. A.4 bottom left.

- upper and lower fit errors are taken as the average values of the weighted MINOS errors from the ensemble. See Fig. A.4 bottom middle and right.

For this example, the central electron W sample was fit over a range of ($n_{L\emptyset}$,n_{CAL}) = (5 -7 ,6 - 12). So, the upper limits in the first fit were ($n_{L\emptyset}$,n_{CAL}) = (5,6). The next fit ran with limits (5,7) which kept the LevelØ limit the same but increased the calorimeter tower limit. The calorimeter tower limit was stepped up until the fit ran with (5,12). Then the LevelØ fit limit was increased, and the fit used limits of (6,6). This process continued until the last fit ran with limits (7,12). The gap fraction obtained from this Range Fit was: $0.99 \pm 0.11 \pm^{0.22}_{0.20}$ %, where the first error is the RMS of the signal distribution and the latter are the means from the weighted upper and lower MINOS error distribution. These errors are added in quadrature to give: $R_{CENTRAL} = 0.99 \pm^{0.25}_{0.24}$ % for the raw gap fraction from the fit (see Table 4.5).

Next, we correct this raw gap fraction for residual contamination (multiple interaction events erroneously included in the sample). The residual contamination for the central electron W sample is calculated to be: $9.2 \pm^{5.4}_{5.7}$ % (see Table 4.3).

$$R_{CORRECTED} = \frac{R_{RAW}}{0.908} = \frac{0.99}{0.908} = 1.09 \pm^{0.28}_{0.27} \%. \tag{A.1}$$

For some events samples with extremely low statistics, the Z data sample is a good example, the range fit does not work well. It is therefore advantageous to find a reasonable way to increase statistics in order to fill out the background shape. With a more populated background multiplicity, the shape becomes more apparent and the fit results stabilize. We use several methods to increase the statistics used in the fit.

As an example we will discuss the method where the combined central and forward electron W samples are used to determine the non-diffractive background shape. In the *Alternate Background Sample Fit Method*, the simple *Range Fit* method is expanded. The same two dimensional fits will be done over the same ranges in upper limits for $n_{L\emptyset}$ and n_{CAL}. However, the shape of the background is taken from the high statistics sample only. For our specific example, we want to find the signal fraction from the central electron W sample using the combined central + forward electron W samples to obtain a reliable background shape. Initially, the 2D simultaneous signal and background fit is done on the central+forward sample. The background parameters from this fit are saved and scaled to the sample size of the central electron sample. These newly scaled background parameters are then used as input parameters to the fit of the central electron W sample. During the fitting of the central electron sample, the background shape is fixed and only the signal parameters are allowed to vary. This process is repeated for each of the 21 range fits. The fit results are shown in Fig. A.5. Again, we determine the weighted mean signal fraction, so now we have $R_{CENTRAL} = 0.98 \ \pm 0.07 \pm^{0.16}_{0.14} \pm 0.02\%$. The first error is again from the mean of the weighted signal distribution, the second is from the weighted upper and lower MINOS error distribution, and the last is the error on the alternate sample background method. This was determined by varying the background parameters in either direction based on the covariant error matrix provided in MINUIT, and then rerunning the fits. Again, we apply the residual contamination calculation and obtain our final central electron diffractive W gap fraction of $R_{CENTRAL} = 1.08 \ \pm^{0.21}_{0.19} \%$.

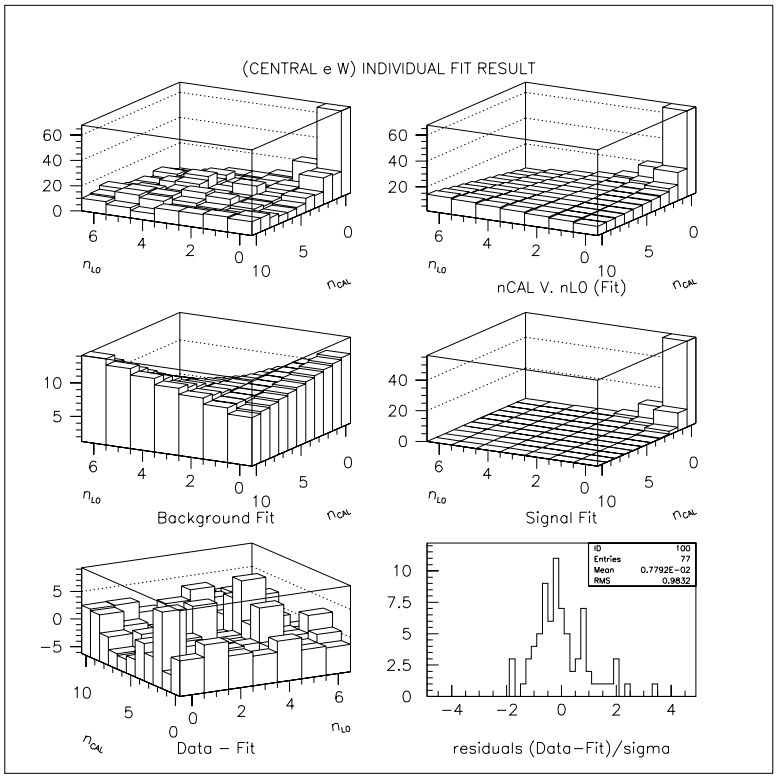

Figure A.2. Two dimensional multiplicities (LØ vs calorimeter towers) from fitting routine are shown for a single fit for the central electron sample. This fit was done using upper limits in ($n_{L\emptyset}$,n_{CAL}) =(7,11). The top left plot is the 2D $n_{L\emptyset}$ vs. n_{CAL} data distribution. The top right plot shows the 2D $n_{L\emptyset}$ vs. n_{CAL} distribution found using the fit where the signal fit result is added to the background background from the fit. The middle left plot shows the 2D background multiplicity distribution from the fit, and the middle right plot shows the signal multiplicity distribution from the fit. (Note: these two middle plots combine to produce the top right distribution.) The bottom left shows the data - fit distribution, and the bottom right shows the residuals for this single fit.

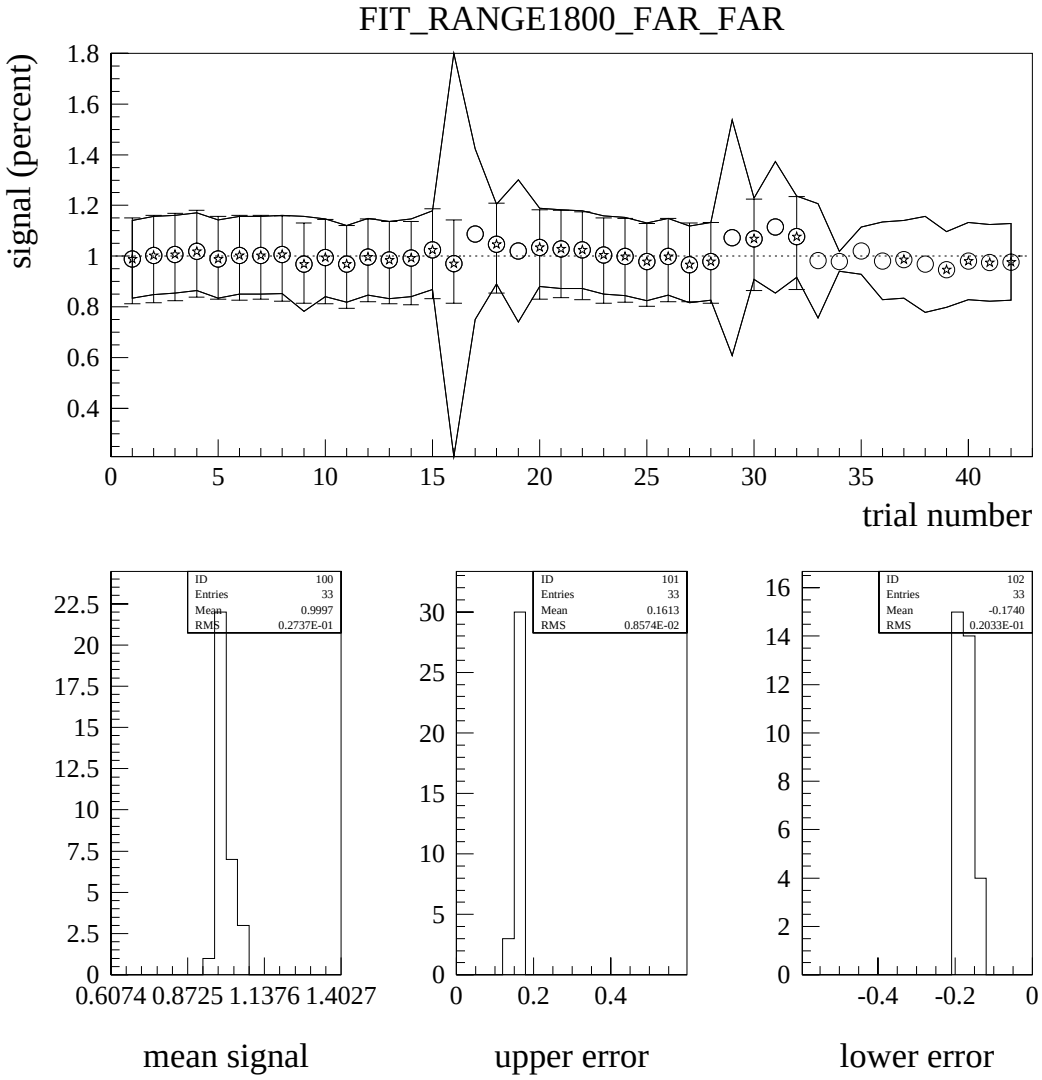

Figure A.3. Top: Variation of hard single diffraction with jets signal where 42 different fits have been done (x-axis) by varying the background region used in the fit. The bottom left plot shows the signal distribution with one entry per fit. This is used to find the mean signal fraction, and the rms error on the distribution. The bottom center and bottom left plots show the distributions of the upper and lower MINOS errors, respectively, for each fit.

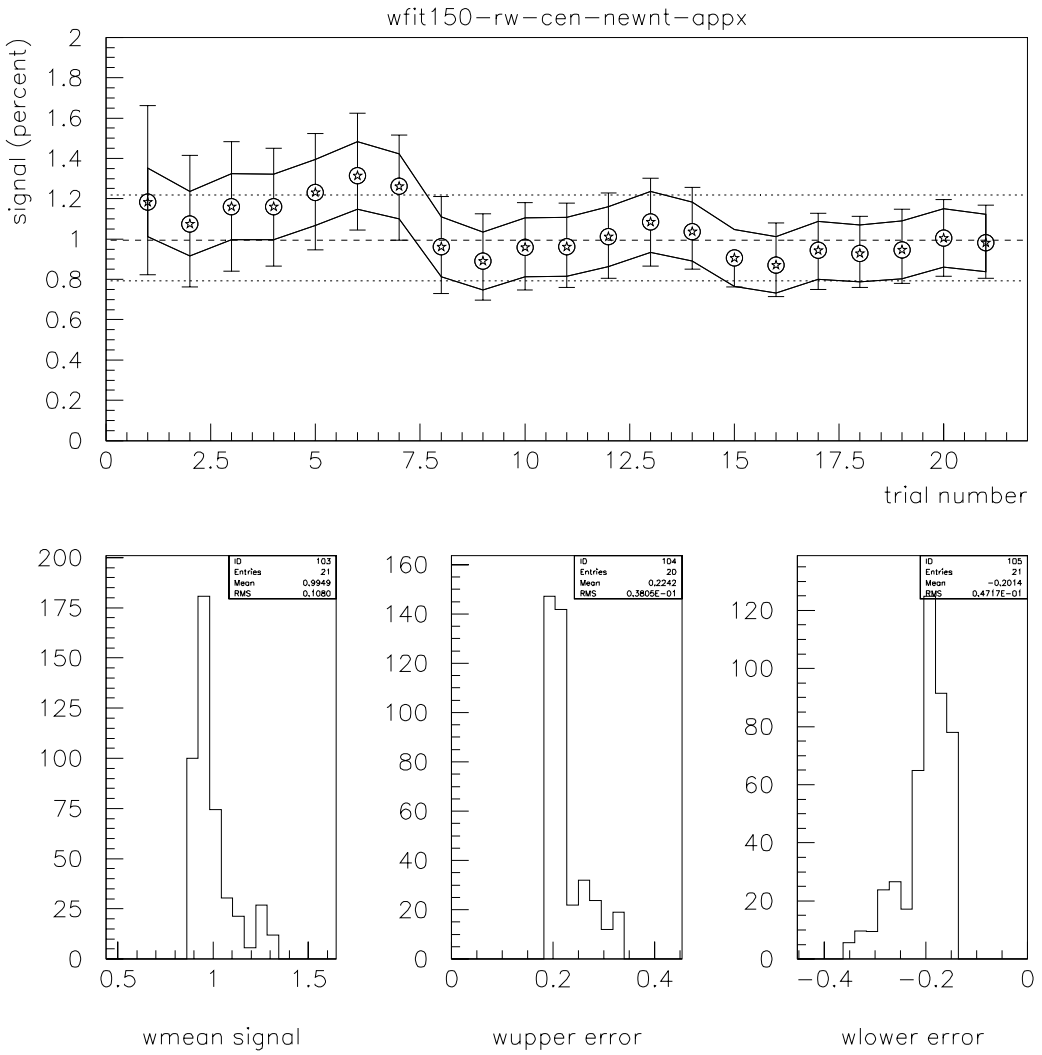

Figure A.4. Top: Variation of central electron diffractive W signal where 21 different fits have been done (x-axis) by varying the background region used in the fit. The bottom left plot shows the weighted signal distribution with one entry per fit. This is used to find the weighted mean signal fraction, and the rms error on this distribution. The bottom center and bottom left plots show the distributions of the weighted upper and lower MINOS errors, respectively, for each fit. In each case, fits with smaller MINOS errors are given higher weight in the average.

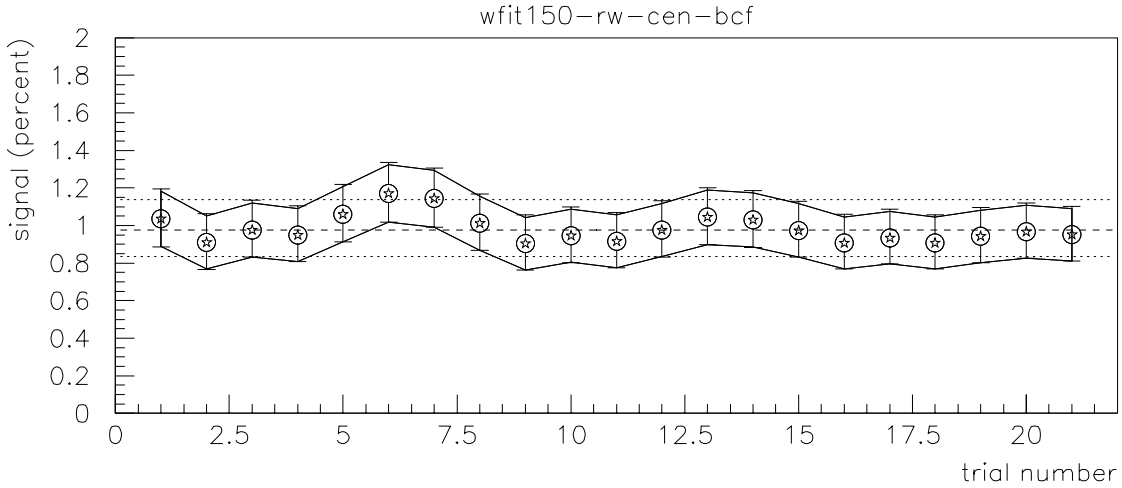

Figure A.5. The fit results for the 1800 GeV central electron W data sample are presented. Shown is the variation of the signal for fits using an upper limit range of 5-7 in LØ bins and 6-12 in n_{CAL} bins (top). The bands represent the parabolic errors from MINUIT and the error bars show the MINOS errors. The combined central and forward electron W sample was used to find the background shape for this fit.

BIBLIOGRAPHY

[1] B. Abbott et al.(DØ Collaboration), Phys. Rev. Lett. **82**, 2457 (1999).

[2] N. Hadley, "Cone Algorithm for Jet Finding", DØ Internal Note 904.

[3] S. Abachi et al.(DØ Collaboration), Phys. Rev. Lett. **74**, 2632 (1995).

[4] P.D.B. Collins, An Introduction to Regge Theory and High Energy Physics, Cambridge University Press (1977).

[5] G. Ingelman and P. Schlein, Phys. Lett. **B152**, 256 (1985).

[6] D. Griffiths, *Introduction to Elementary Particles*, John Wiley and Sons, New York (1987).

[7] V.D. Barger and R.J.N. Phillips, *Collider Physics*, Addison-Wesley (1987).

[8] G. Kane, *Modern Elementary Particle Physics: the fundamental particles and forces*, Addison-Wesley (1993).

[9] M. Shochet,"The Physics of Proton Antiproton Collisions", *Lectures from Les Houches Summer School*, Les Houches, Fr. (1991).

[10] F. Gross, *Relativistic Quantum Mechanics and Field Theory*, John Wiley and Sons, New York (1993), pp. 171,581.

[11] National Research Council, *Elementary-Particle Physics: Revealing the Secrets of Energy and Matter*, National Academy Press (1998).

[12] K. Goulianos, Phys. Rep. **101**, 169 (1983).

[13] F.E. Low, Phys. Rev. **D 12**, 163 (1975).

[14] R. Bonino et al.(UA8 Collaboration), Phys. Lett. **B211**, 239 (1988).

[15] A. Brandt et al.(UA8 Collaboration), Phys. Lett. **B297**, 417 (1992).

[16] M. Derrick et al.(ZEUS Collaboration), Phys. Lett. **B356**, 129 (1995).

[17] T. Ahmed et al.(H1 Collaboration), Nucl. Phys. **B435**, 3 (1995).

[18] T. Ahmed et al.(H1 Collaboration), Phys. Lett. **B348**, 681 (1995).

[19] P. Bruni and G. Ingelman, Phys. Lett. **B311**, 317 (1993).

[20] DØ Collaboration, "Proposal for a Forward Proton Detector at DØ" (presented by A. Brandt), Proposal P-900 submitted to the Fermilab PAC (1997); A. Brandt *et al*, Fermilab PUB–97-377.

[21] A. Edin, G. Ingelman and J. Rathsman, "Unified description of rapidity gaps and energy flows in DIS final states," Z. Phys. **C75**, 57 (1996).

[22] A. Edin, G. Ingelman and J. Rathsman, "Soft color interactions and the diffractive structure function," J. Phys. **G22**, 943 (1996).

[23] A. Edin, G. Ingelman and J. Rathsman, "Soft color interactions as the origin of rapidity gaps in DIS," Phys. Lett. **B366**, 371 (1996).

[24] A. Edin, G. Ingelman and J. Rathsman, "Rapidity gaps in DIS through soft color interactions," hep-ph/9508224.

[25] A. Edin, "Soft Colour Interactions at the Tevatron", *Presented at 4th Workshop on Small-x and Diffractive Physics, Fermilab, 1998.*

[26] S. Abachi et al.(DØ Collaboration), Nucl. Instrum. Methods in Phys. Res. **A338**, 185 (1994).

[27] A.R.Baden and N. Hadley, "Jets and Kinematics", DØ Internal Note 957, unpublished.

[28] C.W. Fabjan,"Detectors for Elementary Particle Physics", *Presented at the 1993 European School of High-Energy Physics, Zakopane, Poland 1993.*

[29] V.L. Ginzberg and I.M. Frank, JETP **16**, 15 (1946).

[30] A.R. Clark et al., Nucl. Instr. Meth. **A261**, 420 (1987).

[31] A.R. Clark et al., Nucl. Instr. Meth. **A279**, 243 (1989).

[32] A.R. Clark et al., Nucl. Instr. Meth. **A315**, 193 (1992).

[33] D. Buchholz et al., Nucl. Instr. Meth. **A257**, 556 (1987).

[34] J.F. Detoeuf et al., Nucl. Instr. Meth. **A265**, 157 (1988).

[35] J.F. Detoeuf et al., Nucl. Instr. Meth. **A279**, 310 (1989).

[36] J. Womersley, "Everything your advisor should have told you about Calorimetry... but probably didn't know," Presented at the University of DØ DØ Internal Note 2365, unpublished.

[37] C. Brown et al., Nucl. Instr. Meth. **A279**, 121 (1989).

[38] M. Abolins et al., IEEE Trans. Nucl. Sci. **NS-36**, 384 (1989).

[39] M. Abolins et al., Nucl. Instr. Meth. **A289**, 543 (1990).

[40] J. Drinkard, "The DØ Level 1.5 Calorimeter Trigger," DØ Internal Note 2274 (1994), unpublished.

[41] D. Edmunds, S. Gross, and P. Laurens for the DØ Collaboration, "A DSP Based Calorimeter Trigger for the DØ Experiment," 1994 IEEE Nuclear Science Symposium Volume 2, pp. 819-823.

[42] B. Abbott et al.(DØ Collaboration), Phys. Rev.**D58**, 092003 (1998).

[43] The bad runs are eliminated using the RUN SELECT package within the DOUSER framework, both of which are part of the standard DØ software library. This removes bad runs listed in /d0library/physics_util/general/bad_run.rcp except for those with problems restricted only to the muon system. This RCP file is dated 13-SEP-1996.

[44] B. Abbott et al.(DØ Collaboration), Phys. Rev.**D61**, 072001 (2000).

[45] G. Gomez, Ph.D thesis, University of Maryland, 1999 (unpublished).

[46] B. Abbott et al.(DØ Collaboration), Phys. Rev.**D61**, 072001 (2000).

[47] S. Abachi et al.(DØ Collaboration), Phys. Rev.**D52**, 4877 (1995).

[48] A. Brandt, L.Coney, B. Hirosky, and K.Mauritz, Hard Single Diffraction EB Note, www-d0.fnal.gov/ brandta/d0_private/hsd_prl.html.

[49] P. Bruni, A. Edin, and G. Ingelman, "POMPYT version 26 –A Monte Carlo to Simulate Diffractive Hard Scattering Processes," ISSN 0418-9833.

[50] T. Sjostrand, Computer Physics Commun. **82**, 74 (1994).

[51] J.F. Owens and W.K. Tung, Annu. Rev. Nucl. Sci. **42**, 291 (1992).

[52] H.L. Lai et al.(CTEQ Collaboration), Phys. Rev.**D51**, 4763 (1995).

[53] H.L. Lai et al.(CTEQ Collaboration), Phys. Rev.**D55**, 1280 (1997).

[54] CTEQ Collaboration (Coordinated Theoretical/Experimental Project on QCD Phenomenology and Tests of the Standard Model) consists of the authors of [52] and [53], and S. Kuhlmann(ANL), S. Mishra(Harvard), R. Brock, J. Pumplin, C.P. Yuan (MSU), D. Soper(Oregon),J. Collins, J. Whitmore(PSU), F. Olness (SMU), and J. Smith, G. Sterman(Stony Brook).

[55] F. Abe et al.(CDF Collaboration), Phys. Rev. Lett. **74**, 850 (1995).

[56] A. Baldit et al.(NA51 Collaboration), Phys. Lett. **B332**, 159 (1992).

[57] R. Brun and F. Carminati, CERN Program Library Long Writeup W5013, 1993 (unpublished).

[58] B. Hirosky, www-d0.fnal.gov/ hirosky/ d0_private/sddp updates/ sddp updates.html

[59] K. Mauritz, Ph.D thesis, Iowa State University, 1999 (unpublished).

[60] A. Brandt, Private Communication